© Copyright 2015

Kebin Gu

Development of a 2D Mechanical Resonant Push-Pull Scanning Endoscope

Kebin Gu

A dissertation

submitted in partial fulfillment of the

requirements for the degree of

Doctor of Philosophy

University of Washington

2015

Reading Committee:

Wei-Chih Wang, Chair

Albert S. Kobayashi

Brian A. Nelson

Program Authorized to Offer Degree:

Mechanical Engineering

University of Washington

Abstract

Development of a 2D Mechanical Resonant Push-Pull Endoscope

Kebin Gu

Chair of the Supervisory Committee:
Research Associate Professor Wei-Chih Wang
Department of Mechanical Engineering

In recent years, miniature scanner technologies, including micro-electro-mechanical system (MEMS) scanners, have started to appear on the market. Most miniature scanner technologies utilize MEMS scanner mirrors. However, this approach has many limitations. In the meanwhile, a competing technology called fiber optic resonant scanner (FORS) has also been developed in order to obtain forward image. An off-the-shelf piezoelectric actuator at the base to create transverse vibrations of a resonating optical fiber has shown to be an effective method for generating 1D and 2D laser line scans. We previously developed a 2D micro image display device that utilized MEMS-based waveguide to replace the optical fiber, which can potentially overcome the size limitations of mirror-based display. In this research, an improved waveguide scanner system using a fully integrated MEMS-based push-pull actuator is presented. This

prototype features monolithic integration of the waveguide, actuator, and light source, and removes the dependence on external actuators used by the previous design. The transmission efficiency is low and cantilever is slightly under tensile stress due to inherent imperfection in the process imperfection and tooling in fabrication. Nevertheless, 2D light scanning pattern is successfully demonstrated using 1D push-pull actuation.

TABLE OF CONTENTS

List of Figures iii

List of Tables vii

Chapter 1. Introduction 1

Chapter 2. Design and Working principle 5

- 2.1 Device Design Consideration 5
- 2.2 Operating Principle 6

Chapter 3. Finite Element Model and Parametric Study 9

- 3.1 Piezoelectric Design 9
  - 3.1.1 Parametric Study 10
  - 3.1.2 Study on Line Resolution 11
  - 3.1.3 Study on Field of View 13
- 3.2 Electrostatic Design 16
  - 3.2.1 Parametric Study 16
  - 3.2.2 Optimized Design 19
  - 3.2.3 Actuator Modification 20

Chapter 4. Optical Analysis 24

Chapter 5. Device Fabrication and characterization 30

- 5.1 Device Fabrication 30
  - 5.1.1 SU-8 Introduction 30
  - 5.1.2 Fabrication Process of PZT Push-Pull Device 30
  - 5.1.3 Fabrication Process of Electrostatic Push-Pull Scanner 33
  - 5.1.4 Results and Discussion 35
- 5.2 Device Package Design 50
- 5.3 MEMS Device Testing 52

5.3.1 Piezoelectric Device Testing 52
5.3.2 Electrostatic Device Testing 55
Chapter 6. Conclusions 63
Bibliography 65
Appendix A: Piezoelectric Scanner Microfabrication Process Flow 75
Appendix B: Electrostatic Scanner Microfabrication Process Flow 91
Appendix C: Preparing for the MEMS Device Test Sample 113

LIST OF FIGURES

Figure 2.1. Schematic diagram and geometric parameters of the proposed scanner. 6
Figure 2.2. Two typical mode shapes of the waveguide. 7
Figure 2.3. Basic operating principle of the 2-D scanner using push-pull actuator (a) showing vertical scan, and (b) showing horizontal scan. 8
Figure 3.1. FRF on the angle of rotation. (a) case I, (b) case II, and (c) case III (parameters given in Table 3.2). 15
Figure 3.2. Schematic of the MEMS scanner with illustrations of the 3D physical geometry mapped to the corresponding behavior symbols. 17
Figure 3.3. Effect of waveguide length on the resonant frequency: (top trace) frequency response in the low-frequency mode direction and (bottom trace) frequency response in the high-frequency mode direction. 17
Figure 3.4. Effect of waveguide width on the resonant frequency. top: frequecy response in the low-frequency mode direction, bottom: frequency response in the high-frequency mode direction. 19
Figure 3.5. Effect of mass size on the resonant frequency: (top trace) frequency response in the low-frequency mode direction and (bottom trace) frequency response in the high-frequency mode direction. 19
Figure 3.6. The modified parallel plate actuator. The bottom electrode is expanded along Y-axis so that the fringe effect causes larger electrostatic force in Y direction than that in X direction. 21
Figure 3.7. Harmonic virtualization of the scanner in Architect3D under the electrostatic excitation: (a) low frequency motion and (b) high-frequency motion. 22
Figure 3.8. Pull-in effect study: (Top trace) rotational angle response of the low-frequency mode, (middle trace) rotational angle response of the low-frequency mode, and (bottom trace) deflection response of the electrodes. 22

Figure 3.9. Layout of the optimized scanner design with a 2-μm-thick slab and a 2-μm-thick rib (Unit: μm). The layout is generated by Architect3D. Each color indicates same mask for micro-fabrication. 23

Figure 4.1. Cross section of the waveguide structure. 25

Figure 4.2. Waveguide width as a function of waveguide height at different r values. 26

Figure 4.3. Modal profile of the waveguide scanner at λ= 800 nm. 27

Figure 4.4. Wave propagation along the waveguide using a Gaussian beam profile for the 10 μm core input fiber (a) operating at 1.3 μm, (b) operating at 0.7 μm. 29

Figure 5.1. Fabrication process of mechanical based scanning endoscope. Left: Actuators portion. Right: Waveguide portion. (a) RIE etch front side oxide/nitride open window. (b) Deposit bottom electrode/PZT layer/up electrode. (c) Use wet etching to pattern PZT actuator, deep-RIE to etch front side fiber grooves, and pattern sacrificial layer to level nitride/oxide opening. (d) Spin and develop double-layer SU-8 2 waveguide cantilever. (e) Backside etch-through to release actuators and waveguide tips. 32

Figure 5.2. Fabrication process of electrostatic scanner. (a)-(e): scanner body and bottom electrodes (f)-(g): top electrodes. (a) Double-layer photolithography process to define rib shape waveguide and scanner pads (b) Development process to create SU-8 waveguide and body (c) Au/Ti metal thin films are deposited and patterned by lift-off process (d) Front side fiber grooves are patterned and deep etched using DRIE (e) the scanner (bottom electrode and waveguide) were released by DRIE again from the backside of the wafer (e) Backside etch-through to release actuators and waveguide tips (f) top electrodes is deposited and patterned on a second silicon wafer (g) SU-8 spacers are spun and patterned. Finally, the top and bottom electrodes can be assembled by the aid of an extra holder. 34

Figure 5.3. Top view of the micro-fabricated resonant push-pull scanners. (a): PZT scanner (before DRIE etch through), and (b), electrostatic scanner (scanner and bottom electrodes only). 37

Figure 5.4. SEM pictures of (a) a curling double-layer SU-8 waveguide, and (b) a straight double-layer SU-8 waveguide after modifying SU-8 lithographic recipe. 38

Figure 5.5. Microscopic pictures show lithographic result of double-layer SU-8 layer on top of nitride/silicon wafer. (a) Lower baking temperature (65°C/95°C) (b) Higher baking temperature (70°C/105°C). 38
Figure 5.6. SEM picture shows a misaligned double-layer SU-8 waveguide. 39
Figure 5.7. (a) Sol-gel PZT thin film on a patterned bottom electrodes. (b) The same sol-gel PZT on an un-patterned bottom electrode. The film appears defect-free. 40
Figure 5.8. SEM image of the micro scanner made of a commercial available PZT solution (left) and power spectrum as a function of the frequency for the micro scanners. The numbers above the peaks denotes the frequency at the peak in Hz (right) [73]. 41
Figure 5.9. Schematic of Bosch process: (a) PR opening for DRIE; (b) SF_6 isotropic etch step; (c) C_4F_8 passivation layer deposition; (d) next etch step. Etch and passivation pulses repeated [77]. 43
Figure 5.10. SEM pictures show RIE lag during DRIE etch. Under the same etch condition and duration, (a) a smaller etch rate for a narrower line and (b), a faster etch rate for a wider line.. 44
Figure 5.11. Microscope pictures show (a) after 750 DRIE loops, only the center of the backside open window is etched through the front side due to the non-uniformity of DIRE. There are still silicon residues around the corners, and (b) adding 30 DRIE loops more to clean the silicon residue around the corner. 46
Figure 5.12. (a) The original scanner design with added thin silicon oxide layer between waveguide and silicon. (b) DRIE etch through from the back side of the silicon wafer. The DRIE etch will stop automatically at the etch stop layer (oxide). (c) Use RIE oxide etch to clean oxide from the front side of the device. Oxide will remain under the waveguide and pads area.. 48
Figure 5.13. Schematic diagram of a proposed MEMS resonant scanner [82]. 48
Figure 5.14. (a) Failed lift-off process to pattern bottom electrodes due to the UV- trasmissive effect. (b): a successful bottom electrodes patterning.. 49
Figure 5.15. Schematic of the lateral UV-transmissive effect in a substrate with transparent coating. Lateral resolution of the photoresist can be affected due to the effect [84]. 50

Figure 5.16. A diagram shows both top and bottom holders for the micro-fabricated device. 51
Figure 5.17. Schematics of assembles MEMS device including top electrode, scanner, bottom electrodes, and GRIN lens with the device holder. 51
Figure 5.18. Vertical frequency response. 52
Figure 5.19. Optical test apparatus. 52
Figure 5.20. Waveguide with coupled light source. (a) Aerial view, and (b), light coming out from the tip of cantilever waveguide, and (c) diverging beam. 54
Figure 5.21. Microscope picture of a tapered single mode fiber (cladding diameter of 125 μm) tip resulting from a chemical etching process, and the comparison of (b) Output of a single "pixel" from this tapered fiber tip and (c) original un-tapered fiber tip. 55
Figure 5.22. (a) the MEMS device test sample (b) apparatus for the electrostatic scanner with (c), a single mode fiber inserted in the fiber groove with an angle for the best coupling. (d) two cameras equipped with high power lenses (250× magnification) are set to provide aerial view and front view images. 57
Figure 5.23. Aerial view of the waveguide with light coupled into the waveguide. 58
Figure 5.24. (a) Waveguide tip displacement vs. resonant frequency under the driving voltages with 100V DC to bottom electrodes and 150V AC to top electrodes. Microscope pictures show driving frequency under (b) 0 Hz, (c) 201 Hz. 59
Figure 5.25. Statistic actuator deformation under various input DC voltage. 59
Figure 5.26. A 30× AC amplifier connected with the function generator (HP 8904A, USA) is used to generate high voltage for MEMS device testing. 60
Figure 5.27. (a) Waveguide tip displacement and (b) scanning angle versus varies applied voltage under 1 Hz driving frequency. 61
Figure 5.28. Vertical and horizontal displacement can be achieved by applying 50 V DC to the bottom electrodes and 50 V AC to the top electrodes with (a) same phase, and (b), with 180 degree phase difference to the left and right electrodes. 62
Figure 5.29. Microscopic picture shows residual silicon around corner of actuators after deep RIE released. Picture taken from the backside and focus on the surface of the actuators. 62

LIST OF TABLES

Table 3.1. Material properties of the scanner model. 10

Table 3.2. Comparison of selected cases in actuation and PZT pad sizes. 14

Table 3.3. Resonant frequencies obtained by FEM and Architect3D. (Waveguide length 2250 µm, width of the slab 55 µm, width of the ridge 5 µm, and the mass size 300 µm). 20

Table 3.4. Reaction force of the modified actuator along X, Y, and Z axis. 21

Table 4.1. Waveguide Geometry (unit: µm). 26

Table 4.2. Output power as a function of waveguide geometry (geometry unit: µm)...... 26

Table 4.3. A summarize of all the key points from each variant (unit: µm)..................... 28

Table 5.1. Parameters in the cyclic Bosch process in DRIE. 43

Table 5.2. Light coupling measurement. 54

Chapter 1. INTRODUCTION

Micro-electromechanical systems (MEMS) is a technology of very small devices which utilizes processes developed by the semiconductor industry. The versatility of MEMS technology integrates mechanical and electrical components and has feature sizes ranging from microns to millimeters. The use of MEMS has yielded many commercial products such as accelerometers, gyroscopes, pressure sensors, microphones, etc. Due to the increased demand for minimally invasive medical procedures (MIMPs), technological advancements in endoscopy design are currently developing. One such advancement is reducing the overall size of the endoscope system while maintaining the resolution and field-of-view (FOV), as well as adding the capability of cross-sectional imaging of biological tissues at micrometer-scale resolution. Reduction of size results in less tissue damage and trauma during operation as well as faster recovery times for patients. Additionally, areas that are inaccessible by today's endoscope designs will be possible to examine.

In recent years, miniature scanner technologies, including micro-electro-mechanical system (MEMS) scanners, have started to appear on the market. Miniature scanner technologies have been employed in scanning confocal microscopy, a powerful optical imaging method that can achieve sub-cellular resolution in real time [1-4]. Beam scanning can be accomplished with electrostatic (comb drive) or electromagnetic MEMS bi-axial scan mirror to achieve both high frame rate and high optical resolution imaging. Miniature scanner technologies can also be used in portable, lightweight, low-power, inexpensive projection video displays with high information content [5-9]. Again the electrostatic attraction [5, 6] or an external piezoelectric ceramic bimorph vibrating element [9] is used. Another application of miniature scanner technologies is near-eye virtual displays like head-mounted displays (HMD) [10-14]. Miniature displays based on scanning a low power beam directly onto the viewer's retina can offer high spatial and color resolution and very high luminance.

As mentioned above, most miniature scanner technologies utilize MEMS scanner mirrors. However, this approach has many limitations. For instance, mirror-based scanners are impractical for large angle beam deflection because mirror scanners and grating deflectors must be significantly larger than the source light beam diameter to avoid beam clipping or adding

diffraction. Reducing the diameter of a conventional display device reduces the possible number of pixels, and thus reduces the resolution and/or FOV of the device.

In the meantime, non-MEMS imaging acquisition technologies such as the scanning fiber endoscope (SFE) have also been introduced for image acquisition applications. One example is the single-mode fiber optic catheter-endoscope for optical coherence tomography (OCT) [15, 16], a rotating device composed of a single mode fiber, a miniature beam focusing element (a gradient-index lens), and a micro prism is mounted for beam directing. Compared with this transverse-imaging OCT endoscope, another technology called fiber optic resonant scanner (FORS) has also been developed in order to obtain forward image. The concept is to move an optical fiber (or a fiber bundle) at its resonant frequencies to either detect or produce 2D images. An off-the-shelf piezoelectric actuator at the base to create transverse vibrations of a resonating optical fiber has shown to be an effective method for generating 1D and 2D laser line scans [17-21].

The research team of the Micro Technology Lab at University of Washington has previously developed a MEMS-based 2D micro image display device that can potentially overcome the size limitations of mirror-based display systems while maintaining high image resolution and FOV. The optical scanner consists of a micro-fabricated waveguide that is electromechanically deflected by a 2D piezoelectric actuator [22, 23]. While functional, the original scanner design has a relatively large footprint (each individual driving actuator is $20\times4.8\times0.6$ mm^3) and is difficult to replicate accurately. Although off-the-shelf PZT bimorph actuators provide ample display actuation, the original scanner is too large to be effective, and the assembly of the device is difficult, time intensive, and unlikely to provide identical systems. The scanner also produces inconsistent results after each reset due to the way the system is assembled.

In this research, an improved waveguide scanner system is presented, using a fully integrated MEMS-based push-pull actuator. The new design has several advantages over the previous generation: 1) the shorter rigid device length makes the potential endoscope more flexible, able to access channels with sharp bends without the risk of penetration into the surrounding tissue; 2) incorporation of the light source and scanning waveguide probe into an integrated system, further reduces the system size; 3) MEMs-based batch processing. MEMS devices provide good signal to noise ratios and smaller power consumption; batch processing lowers fabrication costs while providing scalable production with consistent device quality and behavior.

The push-pull actuation design in this research is generic and can be piezoelectric, electrostatic, electromagnetic, or magnetostrictive. The piezoelectric uses the displacement due to strain induced by an electric filed, the electrostatic is the attraction between oppositely charged conductors, and the magnetic is the displacement due to interaction among various magnetic elements, including permanent magnets, external magnetic fields, and magnetizable material, etc. All approaches are with different advantages and limitations.

In the first couple years of this research, we have tried developing and fabricating several techniques including sol-gel PZT (lead-zirconate-titanate) piezoelectric actuator, e-gun evaporated permalloy film, the electromagnetic actuation with micro-coils, and parallel-plate electrostatic actuators. However, due to the fact that it is difficult to fabricate defect-free piezoelectric thin films of patterned electrodes (PZT), the structure is not easy to be integrated with MEMS process and the fabrication complexity (micro-coils), and hard to control the actuation with small displacement (permalloy), currently the working actuation mechanism is the electrostatic design which uses two parallel plate as the actuators. In this dissertation, both PZT-based (lead-zirconate-titanate) piezoelectric MEMS actuator and electrostatic parallel plate actuator are presented. PZT technique is covered since it shows large potentials as this actuation method for the next generation prototype. The details of the micro-coils and permalloy designs and fabrication processes are included in the appendices.

In Chapter 2, we will first discuss the design and operational principles of this novel scanner. Then we will examine through finite element analysis (FEA) in Chapter 3. We will begin our discussion with considering the PZT thin film actuator in our FEM model, then talk about design and optimization process of the electrostatic design performed by Architect3D in CoventorWare, a system-level model method that can significantly shorten the simulation time with relatively high accuracy, as well as the actuators modification by using fringe effect to increase the in-plane electrostatic force. In Chapter 4, optical modal analysis is performed, and the coupling efficiency of the input is examined through Rsoft (RSoft Design Group, Inc., U.S.A.) modeling, followed by a description of the fabrication process of the scanning devices in Chapter 5. First the piezoelectric actuator design is covered and the PZT sol-gel process is discussed. Then the similar fabrication process of the electrostatic device will be explained. Several fabrication challenges and complexity in micro-fabricating these MEMS devices will be investigated. Additionally, the scanning

characteristics of fabricated devices are also presented and discussed. Chapter 6 will conclude this research and explore potential future work.

Chapter 2. DESIGN AND WORKING PRINCIPLE

2.1 DEVICE DESIGN CONSIDERATION

The design of the proposed micro scanner uses a pair of "push-pull" actuators to drive a cantilever waveguide (Fig. 2.1). The backscattered light is captured by the same optical scanner and channeled to an output detector. The focusing optics for the output light beam is a conventional GRIN lens (not shown). The waveguide is made of a long, slender SU-8 structure that runs through the middle of the scanner. At the input end of the waveguide, a coupler couples the light from an optical fiber via a U-shape fiber groove to the cantilever waveguide. At the distal (output) end, a proof mass is attached to the waveguide to purposely reduce the tip displacement while maintaining the same angular deflection. A rotating arm connects the waveguide to the actuators. All actuating pads are rectangular in shape and suspended, with the distal ends anchoring to the substrate. And the middle of the pads is connected to the rotating arm. As we mentioned in the previous chapter, the push-pull actuation design is generic and can be piezoelectric, electrostatic, electromagnetic, or magnetostrictive. In this research, both PZT-based (lead-zirconate-titanate) piezoelectric and electrostatic parallel-plate MEMS actuator are presented.

For the purpose of minimization, the proof mass is attached near the waveguide tip to decrease the tip displacement by weighing it down to create a "pin-like" joint at the tip. In this way, the tip can still rotate but the displacement is minimized, so it can create the largest field of view without incurring a large tip displacement. The field of view in this research is defined as twice the maximum angular direction turned from the extension of the static waveguide tip. Fig. 2.2 (b) shows a typical mode shape of the waveguide exhibiting this "pin-like" motion.

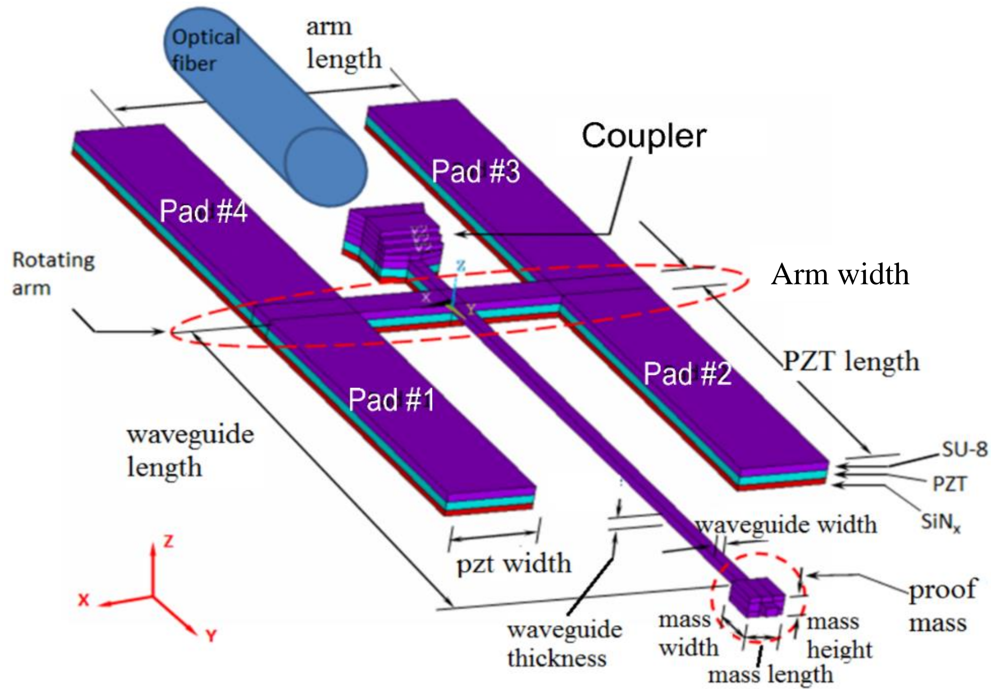

Figure 2.1. Schematic diagram and geometric parameters of the proposed scanner.

It is worthy to note that a 2D raster or Lissajous rather than spiral motion is employed for the scanner. It is very difficult to create spiral motion with a nonsymmetrical mechanical beam profile (in this case a beam width that is ~12 times its overall thickness). It is also very difficult to fabricate a circular cladded waveguide using conventional microfabrication that utilizes a planar manufacturing process. Furthermore, a uniformly cladded waveguide will require a much larger cladding (> 50 μm) to confine the wave and maintains a single mode operation at the require geometry (~ few μm for the core). Therefore, a rib waveguide design is chosen to allow a relatively small core (same size as the conventional optical fiber core) with no cladding for the scanner.

2.2 Operating Principle

The basic operating principle of this 2-D scanner is shown in Fig. 2.3. The bending of the four actuating pads in or out of plane creates the necessary push or pull actuation. The resultant forces exerted by the four corners of the rotating arm can either move the arm along the waveguide direction or rotate the arm on the XY plane, which in turn move the waveguide in or out of the plane. To generate oscillation in the YZ plane, for example, pads 1 and 2 (or pads 3 and 4) must

be moving in the same direction (in YZ plane) and phase (Fig. 2.3a). This will cause the waveguide to move up or down in the Z direction because of the hinge effect at the bottom layer of the coupler. Besides, in order to generate the bending in the XY plane, pads 1 and 3 (or 2 and 4) must be moving in the same direction (in YZ plane) with same magnitude and phase (Fig. 2.3b). The force couple formed by pad 1 and 3 will rotate the arm about x axis and move the waveguide in the X direction. This actuation is accompanied by an out-of-plane movement of the waveguide due to the hinge effect at the bottom layer of the coupler. By exciting motion in the XY and YZ planes simultaneously, the tip of the waveguide will move in a raster scanning fashion. In addition, for the purpose of achieving the raster scanning, the actuators must be driven by a signal formed by superimposing two carefully chosen resonant frequencies for the scanner system. This method of actuation is verified by finite element analysis (FEA).

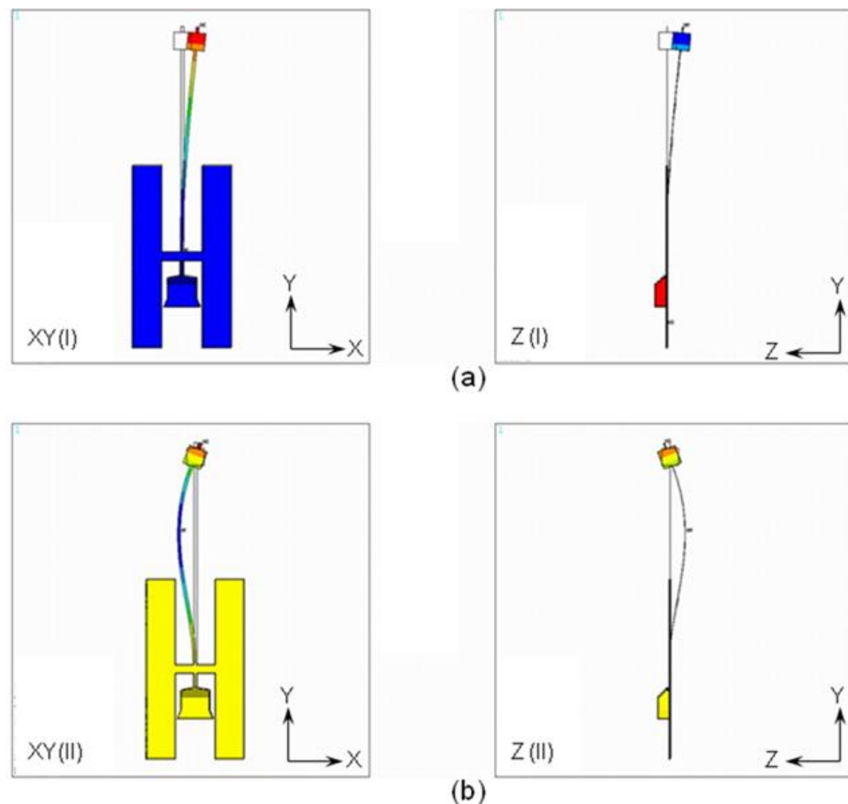

Figure 2.2. Two typical mode shapes of the waveguide.

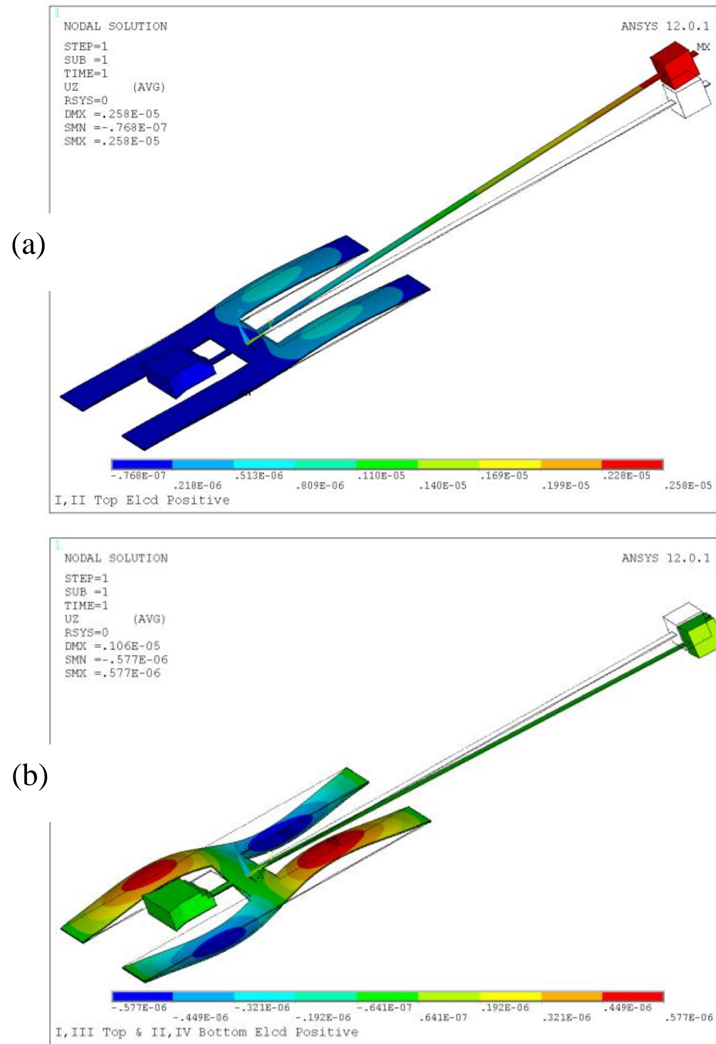

Figure 2.3. Basic operating principle of the 2-D scanner using push-pull actuator (a) showing vertical scan, and (b) showing horizontal scan.

Chapter 3. FINITE ELEMENT MODEL AND PARAMETRIC STUDY

3.1 PIEZOELECTRIC DESIGN

We will begin our discussion with considering the PZT thin film actuator in our FEM model. In general, an actuator consists of a substrate layer, a bottom electrode, a PZT film, and a top electrode. To simplify the finite element model, the relatively thin electrode layers are not included, and the applied voltage potential is modeled with boundary conditions. The final model consists of a substrate layer of silicon nitride (0.2 µm), a PZT layer (1 µm), and a SU-8 layer (2 µm). The model is constrained in all directions on the ends of the four actuating pads and at the bottom surface of the coupler in the substrate layer. ANSYS 3D elements Solid5 with piezoelectric option (for PZT film) and Solid45 (for SiNx and SU-8) are used in the model. The material properties of PZT thin film are adapted from Guo's recipe [24]. All material properties used in this part of research are shown in Table 3.1. The analysis is based on a linear elastic model that assumes no residual thermal stresses from fabrication.

To better understand the device's scanning motion, a slab waveguide with a 20 µm width, 2 µm height, and 1000 µm length is used. Frequencies and mode shapes are obtained using modal analyses. Based on the simulation results, the two lowest resonant frequencies are 131.55 Hz (in the YZ plane) and 1313 Hz (in the XY plane). The lower resonant frequencies are dominated by the waveguide modes because the waveguide is relatively soft compared to other parts of the scanner.

Table 3.1. Material properties of the scanner model.

- *Elastic compliance* $(10^{-12} N/m^2)$

$$\begin{bmatrix} 16.4 & -5.74 & -7.22 & 0 & 0 & 0 \\ -5.74 & 16.4 & -7.22 & 0 & 0 & 0 \\ -7,22 & -7.22 & 18.8 & 0 & 0 & 0 \\ 0 & 0 & 0 & 47.5 & 0 & 0 \\ 0 & 0 & 0 & 0 & 47.5 & 0 \\ 0 & 0 & 0 & 0 & 0 & 44.3 \end{bmatrix}$$

- *Piezoelectric strain* $(10^{-10} C/N)$

$$\begin{bmatrix} 0 & 0 & -171 \\ 0 & 0 & -171 \\ 0 & 0 & 374 \\ 0 & 584 & 0 \\ 584 & 0 & 0 \\ 0 & 0 & 0 \end{bmatrix}$$

- *Dielectric permitivity at constant stress*

$$\begin{bmatrix} 1730 & 0 & 0 \\ 0 & 1730 & 0 \\ 0 & 0 & 1700 \end{bmatrix}$$

$Density = 7550 (kg/m^3)$

Material	SiN_x	SU-8
Young's modulus (GPa)	265	4.5
Poisson' ratio	0.23	0.22
Density (kg/m^3)	3200	1190

3.1.1 *Parametric Study*

To optimize the performance of the scanner, two parameters, the scanning field of view (FOV) and the line resolution must be carefully examined. To obtain a large FOV, the MEMS scanner is designed to operate at its resonant frequencies, where it achieves its maximum displacement and angle of rotation. The line resolution of the scanner depends on the ratio of the two operating frequencies in X and Z directions. Higher resolutions can be obtained by increasing the ratio of the two operating resonant frequencies. To identify important factors of the design, this research utilized ANSYS (ANSYS, Inc., Pennsylvania, USA) to create a second FEA model of the scanner. In the following sections, we will discuss the important design considerations and parameters.

In the model, the system is dissected and analyzed component by component, and the dimensions are optimized to obtain the best line resolution and FOV. The components of primary importance are the proof mass (length, width, and height of the mass), the waveguide (width, thickness, and length), and the actuator (length and width of both the PZT pads and the rotating arm).

3.1.2 *Study on Line Resolution*

Line resolution is linked to the ratio of the resonant frequencies in the vertical and horizontal directions. To find these frequencies, this research first conducted modal analyses and confined the scope of this research to the resonances only occurring in the XY and YZ planes.

Typical mode shape of the waveguide is shown in Fig. 2.2. The first bending mode in the XY plane and Z direction are shown in Fig. 2.2 (a), and the corresponding frequencies are XY (I) and Z(I). The other higher order modes in the study are XY (II), Z (II), and the corresponding mode shapes are shown in Fig. 2.2 (b). To obtain the largest line resolution possible, the ratios between XY (II)/Z I), XY (II)/Z (II), XY (I)/Z (II), and XY (I)/Z (I) are investigated. For practical considerations, the resonant frequencies investigated are less than 50 kHz, because past experience has shown the displacement is relatively small for frequencies greater than 40 kHz, and modes higher than the second order are too difficult to obtain.

The summarized results of the parametric study are:

- Proof mass (overall size)

This parametric study varies the length and the width of the proof mass from 20 to 180 μm and the height from 20 to 60 μm. As the length, width or height of the proof mass increases, the resonant frequencies of the scanner decrease, and the resolutions increase (particularly for XY (II)/Z (I), from 43 to 91). This is a non-trivial improvement; therefore, the dimensions of the proof mass are one of the dominant design factors.

- Waveguide cross-section and PZT thickness

This parametric study varies the waveguide width from 10 to 20 μm, the PZT thickness from 1 to 3 μm, and the SU-8 thickness from 1 to 5 μm. As the width of the waveguide increases, the resonant frequency in the XY plane increases, and the resolution increases as well (particularly for XY (II)/Z (I), from 316 to 531). As the thickness of the waveguide increases, the resonant frequency in the YZ plane increases, and the resolution decreases (particularly for XY (II)/Z (I), from 531 to 60). The PZT thickness does not appear to significantly influence the resolution. A vertically thin or horizontally wide (utilizing the orientation in Figure 2.1) cross-section of the waveguide appears to achieve a larger resolution, and is considered as a dominant design factor.

- Waveguide and actuator dimensions

This parametric study first varies the waveguide length from 400 to 1500 µm, the arm length from 240 to 280 µm, and the arm width from 30 to 70 µm. For the study about the waveguide length, as the length increases, the resonant frequencies of the waveguide in both the XY and the YZ planes decrease significantly. The corresponding line resolution (the ratio of horizontal over vertical resonant frequencies) seems to peak at a waveguide length of 1000 µm (from 100 to 133, then to 118). Regarding the arm layout, as the arm length and width increases, the resonant frequency of the waveguide may increase or decrease, without a definite pattern. The changes of frequency, however, are insignificant. The corresponding change in line resolution is also trivial (from 133.0 to 133.4). Based on this finding, the waveguide length is considered a dominant factor for the scanner resolution, but the length and width of the rotating arm are not.

For the layout of the PZT actuating pads, this study varies the length of the pad from 100 to 500 µm, and the width from 50 to 150 µm. As the size of the pad changes, neither the resonant frequencies of the waveguide nor the resolution (from 130.7 to 130.7) change significantly. The size of the PZT pad is therefore not a factor in the scanner resolution.

Until this point, the results show the geometry of the waveguide (cross section and length) dominates the resolution of the scanner. A flat cross-section, however, does not guarantee a better light transmission. This issue has been analyzed and confirmed separately in optical analysis using waveguide equation and Rsoft BeamPROP^{tm}. To allow practical optical transmission, a ridge structure is added on the original slab waveguide to form a rib waveguide structure. Also, its dimensions are optimized to ensure a single mode operation and optimal light transmission and coupling. The optical analyses have been conducted assuming an equal thickness of the SU-8 layer and the ridge structure. These results will be further discussed in the optical simulation section.

- Rib Waveguide design Consideration

For the purpose of seeing how an additional layer of SU-8 added to the waveguide structure affects the mechanical design, the rib waveguide dimension is examined. Here the slab width is varied from 10 to 20 µm, and the ridge thickness is varied from 1.45 to 4.3 µm, with the slab and ridge assumed to have equal thickness. As the height of the ridge increases, the resonant frequency of the slab in the YZ plane increases, and the scanner resolution decreases (from 182 to 28). As the width of the slab part of the waveguide increases, the resonant frequency in the XY plane increases,

and the scanner resolution increases (from 94 to 182). Therefore, a "flat" cross-section of the waveguide, more rigid in the XY plane and more flexible in the X axis, still tends to contribute to a higher overall scanning resolution. Additionally, when the width of the ridge structure is smaller than the width of the slab, the mechanical resonant frequency is dominated by the slab part of the waveguide.

3.1.3 *Study on Field of View*

The rotation of the distal end of the waveguide serves as an indicator for the device's FOV. Obtaining the waveguide movement at a particular operating frequency requires harmonic or transient analyses. These analyses are usually computationally intensive. As it is estimated that a large static actuation will imply a larger dynamic actuation, a static parametric study of the actuator portion is first conducted to narrow down suitable design dimensions, followed by a harmonic analysis of some selected dimensions as verification. Because the flat geometry of the waveguide is much more difficult to oscillate in the XY plane, the effectiveness of the actuator design will be judged by the tip displacement in XY, with larger displacements translates larger angular rotations of the waveguide are possible. Because the tip displacement is influenced by the geometry of the rotating arm and the forces acting on it, the width and length of the rotating arm and the PZT pad are under investigation. The waveguide displacement is measured with pads 1 and 3 actuated in phase by an applied voltage of 20 V. All other dimensions were based on the previously simulated optimized waveguide.

The damping value is extracted from the previous experiment with a slightly larger cross section cantilever waveguide design [25]. The overall damping can only be found experimentally since it is difficult to separate the air damping from the waveguide’s structural and material damping. For our PZT actuator, the maximum driving voltage is around 20 V. This is based on the poling voltage of 100 V which is sufficient to pole the sample and produce the best electromechanical coupling coefficient out of all our samples.

In this study, the arm width varied from 70 to 130 µm, the arm length from 300 to 2000 µm, the PZT width from 50 to 750 µm, and the PZT length from 300 to 1000 µm. This study discovered that as the length and width of the PZT pad increase, the displacement of the tip increases as well (UXY from 0.078 to 0.221). This can be attributed to the larger forces exerted on the rotating arm

by the larger PZT pads. As the width or length of the rotating arm increases, the displacement of the tip decreases (UXY from 0.361 to 0.104). This can be attributed to a softer arm, which is less efficient in transferring forces from the PZT pads.

The relationship between the tip displacement (UXY) and the angle of rotation is verified with three harmonic analyses of selected geometries (Table 3.2). The plots of the angle of rotation against the frequency response function (FRF) of the three cases are shown in Fig. 3.1. This comparison confirms the original estimate that a larger static tip displacement UXY contributes to a larger dynamic displacement and rotation angle of the waveguide tip in this design.

In the parametric study, the geometry of the waveguide (the cross section and the length) dominates the resolution of the scanner; the resolution increases with a flatter and shorter waveguide (from 60 to 531). The rib waveguide has a very similar resonant frequency response as long as the dimensions of the width of the ridge section are kept relatively small compared to the width of the slab section (<4 x). All other geometric parameters do not appear to affect the resolution significantly. In the analyses for PZT actuator and arm geometries, larger PZT pads allow larger actuation; however, the sizes of the pads are limited by the designed footprint (3×3 mm^2) defined for the endoscopic application. The largest angle of rotation achieved by the investigated push-pull designs is ~4° (Table 3.2, harmonic rotation at XY(I), 2× 2.03°). A shorter rotating arm appears to provide a larger angle of rotation. These findings suggest that the waveguide and the actuator layout can be considered separately to optimize the line resolution and scanning magnitude.

Table 3.2. Comparison of selected cases in actuation and PZT pad sizes.

	Case I	Case II	Case III
Arm Width (µm)	70	100	70
Arm Length (µm)	300	300	1000
PZT Width (µm)	150	150	750
PZT Length (µm)	600	600	1000
Static UXY (µm)	0.221	0.187	0.361
Harmonic UXY at XY(I) (µm)	15.5	12.5	25.7
Harmonic UXY at XY(II) (µm)	0.963	0.811	1.77
Harmonic Rotation at XY(I) (degree)	1.23	0.99	2.03
Harmonic Rotation at XY(II) (degree)	0.93	0.78	1.71

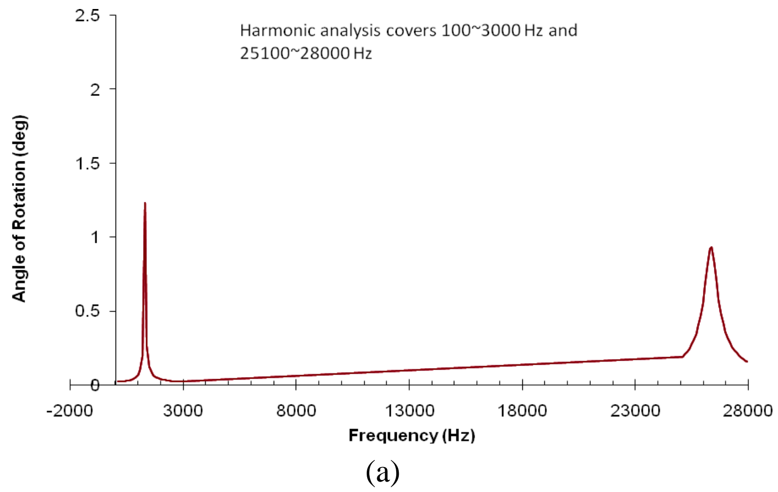

(a)

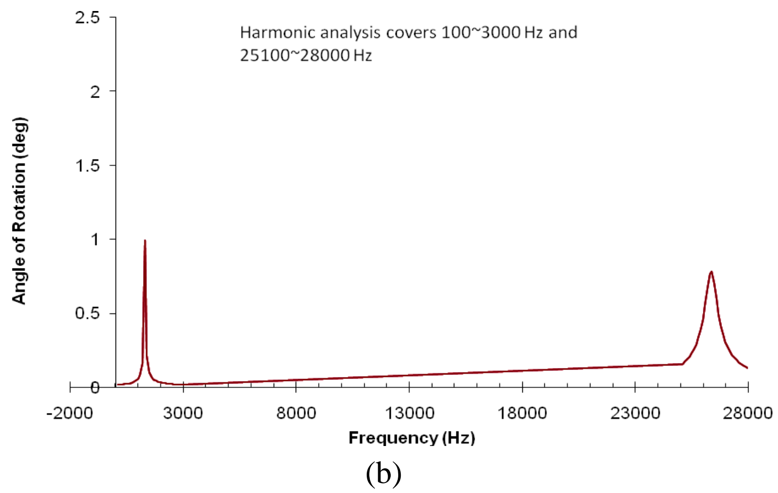

(b)

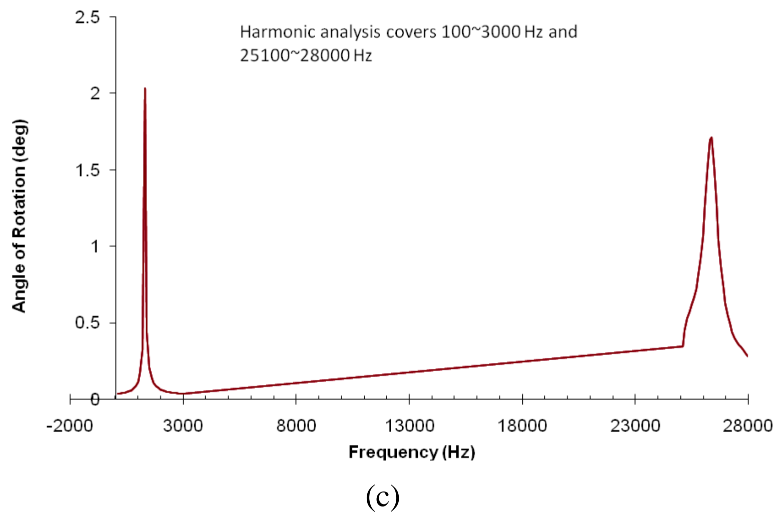

(c)

Figure 3.1. FRF on the angle of rotation. (a) case I, (b) case II, and (c) case III (parameters given in Table 3.2).

3.2 ELECTROSTATIC DESIGN

The design and optimization process of the electrostatic scanner design is performed by Architect3D in CoventorWare. Compared to traditional finite element method (FEM), the system-level model method can significantly shorten the simulation time with relatively high accuracy. Fig. 3.2 shows the schematic layout created in Architect3D and the corresponding 3D model. The schematic layout is composed of various components which are used to model the mechanical and electrical behaviors of the scanner. The components include beams, beams with electrodes, rigid plate, anchors, bus connectors, reference frames and signal sources.

As mentioned in the previous section, to optimize the performance of the scanner, two parameters, the scanning field of view (FOV) and the line resolution must be carefully examined. The high line resolution of the device is obtained through the large difference of the two operation frequencies. The resonant frequency of the high-frequency mode is designed to be 200 times larger than the resonant frequency of the low-frequency mode. Therefore, highest scanning line resolution can be obtained. Since it is difficult to excite a device above 20 kHz in current experiment condition, the resonant frequency of the low-frequency mode must be smaller than 100 Hz. As for the field of view, when the device is operating at its lower order mode resonant frequency, it results in larger FOV compared to higher order modes.

3.2.1 *Parametric Study*

- Effect of Waveguide Length

First, the waveguide length is adjusted from 500 to 2500 μm with an increment of 200 μm. Figure 3.3 shows the waveguide length has a large effect on the resonant frequency. The top trace is the frequency response along the low-frequency mode (vertical) direction. The bottom trace is the frequency response along the high-frequency mode (horizontal) direction. When the length is 2500 μm, the resulting resonant frequency of the low-frequency mode is approximately 150 Hz, which is relatively close to the desired 100 Hz. Therefore, a waveguide length of 2500 μm is chosen as the preliminary optimum size.

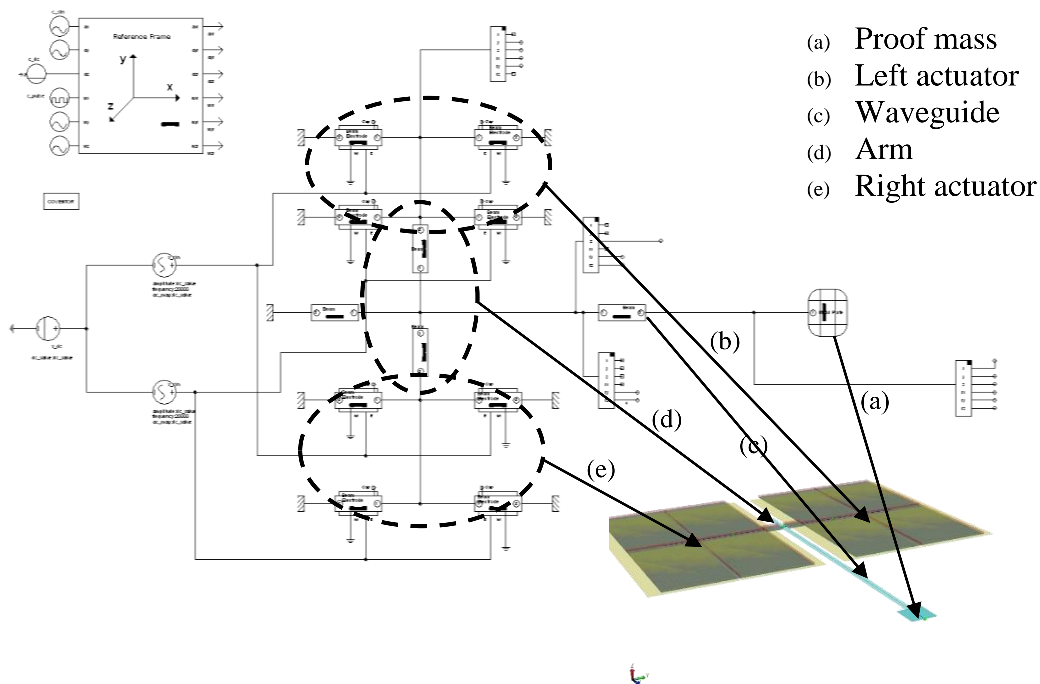

Figure 3.2. Schematic of the MEMS scanner with illustrations of the 3D physical geometry mapped to the corresponding behavior symbols.

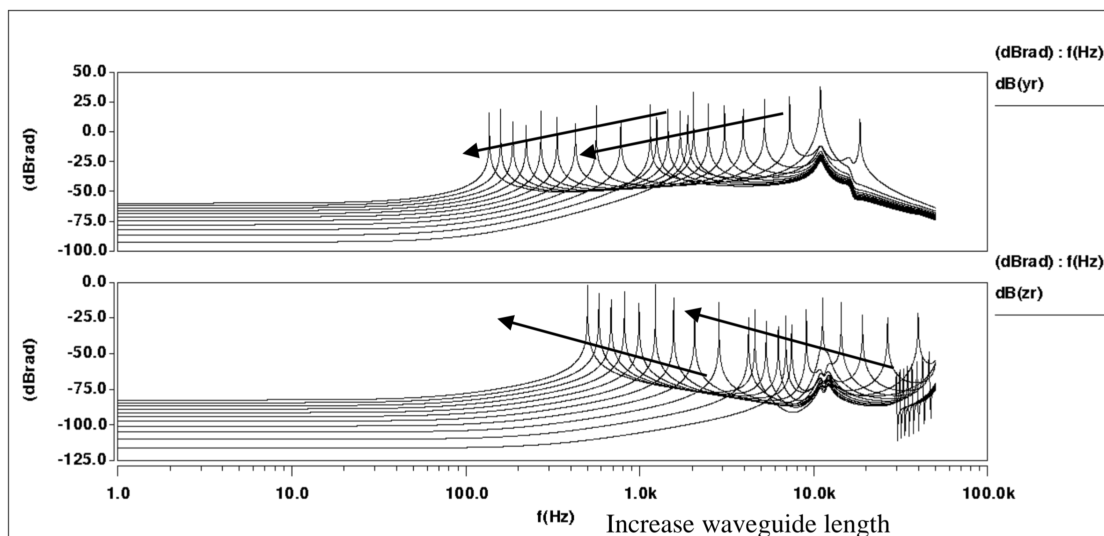

Figure 3.3. Effect of waveguide length on the resonant frequency: (top trace) frequency response in the low-frequency mode direction and (bottom trace) frequency response in the high-frequency mode direction.

- Effect of slab width

Based on the optical simulation which will be discussed in chapter four, the thicknesses of the slab and the ridge are 2 μm respectively and the optimum width of the ridge is 5 μm. The width of the slab is changed from 15 to 115 μm with an increment of 10 μm. Figure 3.4 shows an effect of the width on the resonant frequency in both low-frequency mode direction (top trace) and high-frequency mode direction (bottom). But in the high-frequency mode, there is a much larger effect. Therefore, the width of the slab could be used to increase the ratio between the two resonant frequencies. In other words, the line resolution of the device increases. As shown in Figure 3.4, when the width of the slab is 55 μm, the resonant frequency of the high-frequency mode is approximately 20 kHz. Accordingly, a slab width of 55 μm is chosen and the rest of the parameters will be optimized next.

- Effect of Proof Mass

This study varies the size of the mass from 50 to 550 μm with an increment of 50 μm. Figure 3.5 shows the effect the mass size on the resonant frequency in both low-frequency mode direction (top trace) and high-frequency mode direction (bottom trace). When the mass size is 300 μm, the resonant frequencies of the low-frequency mode and the high-frequency mode are 55 Hz and 10 kHz respectively. As a result, the line resolution is approximately 200.

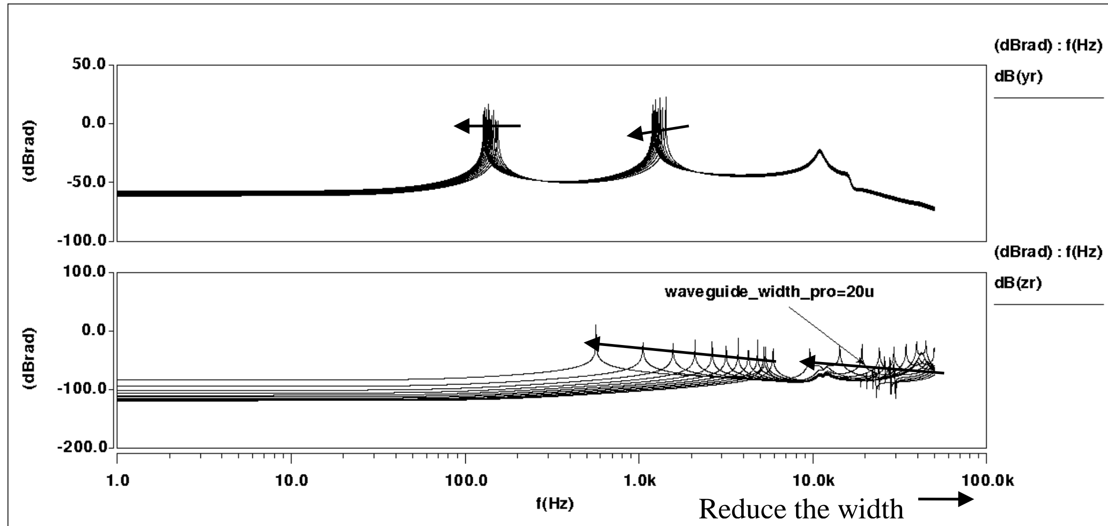

Figure 3.4. Effect of waveguide width on the resonant frequency. top: frequecy response in the low-frequency mode direction, bottom: frequency response in the high-frequency mode direction.

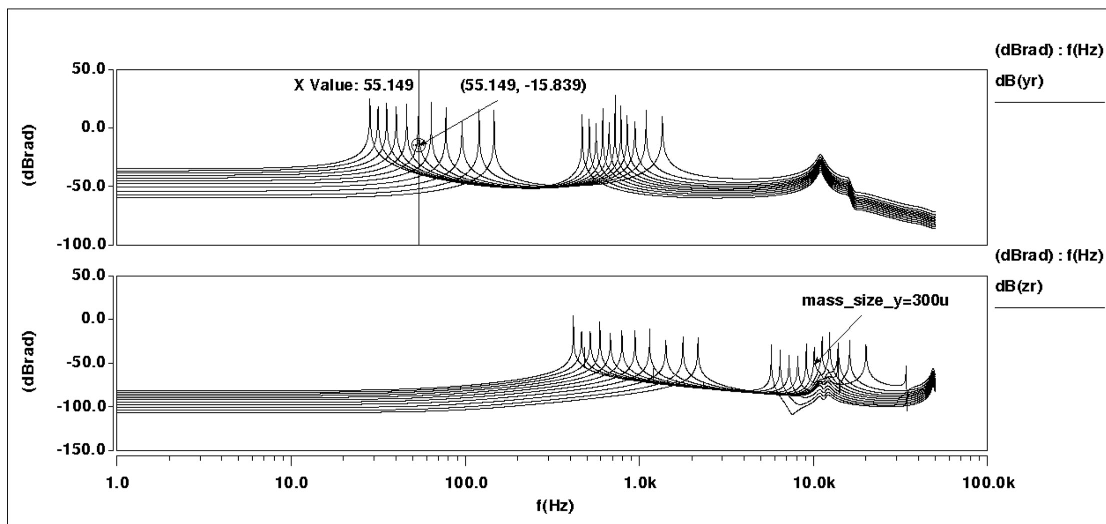

Figure 3.5. Effect of mass size on the resonant frequency: (top trace) frequency response in the low-frequency mode direction and (bottom trace) frequency response in the high-frequency mode direction.

3.2.2 *Optimized Design*

Through the system-level simulation, the trend of the resonant frequency shift under the three parameter variations can be found out swiftly. We can conclude that the width of the slab is

approximately 55 μm. The resulting line resolution is approximately 200. Due to the current experimental setup constraints, the resonant frequency of the high-frequency mode must be lower than 20 kHz; the resulting resonant frequency of the low-frequency mode must be lower than 100 Hz. Because the frequency is a function of the mass and the spring constant, the low frequency (100 Hz) can be achieved through a long waveguide or a large proof mass. Nevertheless, a long waveguide undermines the device compactness. To solve this problem, we design the length of the waveguide and the size of proof mass as 2250 μm and 300 μm respectively. The modal analysis results obtained from Architect are verified by FEM results (Table 3.3). With the knowledge of these preliminary results obtained from modal analysis, the optimization of the rotational angle of each mode is investigated next. The other parameters are kept same as PZT design.

Table 3.3. Resonant frequencies obtained by FEM and Architect3D. (Waveguide length 2250 μm, width of the slab 55 μm, width of the ridge 5 μm, and the mass size 300 μm).

		FEM	**Architect3D**
X-axis	1st	58.3	55.9
	2nd	630	707
Y-axis	1st	1103	1062

3.2.3 *Actuator Modification*

The conventional capacitive actuator is either a set of parallel plate or a set of comb drives [26]. However, the driving force is dominant in one direction (usually out-of-plane direction) and negligible in the other two directions. Fig. 3.6 is the modified actuator design with the extended bottom electrode. The non-equivalent electrodes increase the utilization of electrostatic fringe effect. Therefore, a larger in-plane electrostatic force is generated in Y direction. Table 3.4 shows that the FEM results of the reaction forces of the modified actuator as the applying voltage is 20 V. In the out-of-plane direction, F_z is 27.66 μN. In the two in-plane directions, F_y is 8.64×10-2 μN, which is over two orders of magnitude larger than F_x of 1.92×10-4 μN.

Table 3.4. Reaction force of the modified actuator along X, Y, and Z axis.

F_x (μN)	F_y (μN)	F_z (μN)
1.92×10^{-4}	8.64×10^{-2}	27.66

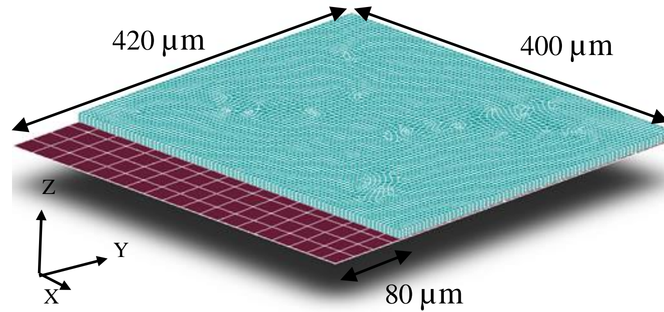

Figure 3.6. The modified parallel plate actuator. The bottom electrode is expanded along Y-axis so that the fringe effect causes larger electrostatic force in Y direction than that in X direction.

The modified actuator is employed to increase the in-plane electrostatic force, leading to large FOV. When the device is in operation, Electrode 1 and 3 are applied the same voltage waveform $V_o \sin\omega t$ and Electrode 2 and 4 are applied $V_o \cos\omega t$, where ω is the resonant frequency of the both low and high-frequency mode and V_o is the amplitude of the voltage waveform. Suppose the waveguide is simultaneously driven at the above two resonant frequencies, a raster scanning pattern will appear.

The excitation of vertical (low frequency) and horizontal motion (high frequency) using harmonic virtualization of the scanner in Architect3D under the electrostatic excitation is shown in Figure 3.7. Figure 3.8 shows the rotational angle response along the low-frequency mode direction. In this direction, there are two resonance peaks. The designed low-frequency mode is chosen as 55.9 Hz. The rotational angle is 0.44 rad. The middle trace is the rotational angle response along the high-frequency mode direction. The 12775 Hz peak is the high-frequency mode. The rotational angle is 0.089 rad. The bottom trace is the deflection response of the electrodes. At the high-frequency mode, the deflection of the electrodes is 4.27 μm which is well below the designed gap space of 20 μm.

Figure 3.9 shows the layout of the optimized resonant scanner with a 2-μm-thick slab and a 2-μm-thick rib. The layout is generated from Architect3D. Each color indicates one mask required in Architect3D. The size of the scanner is approximately 3.5×3 mm^2.

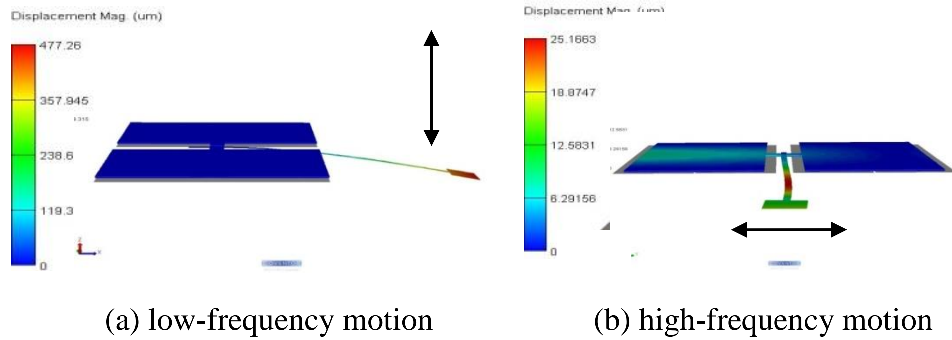

(a) low-frequency motion (b) high-frequency motion

Figure 3.7. Harmonic virtualization of the scanner in Architect3D under the electrostatic excitation: (a) low frequency motion and (b) high-frequency motion.

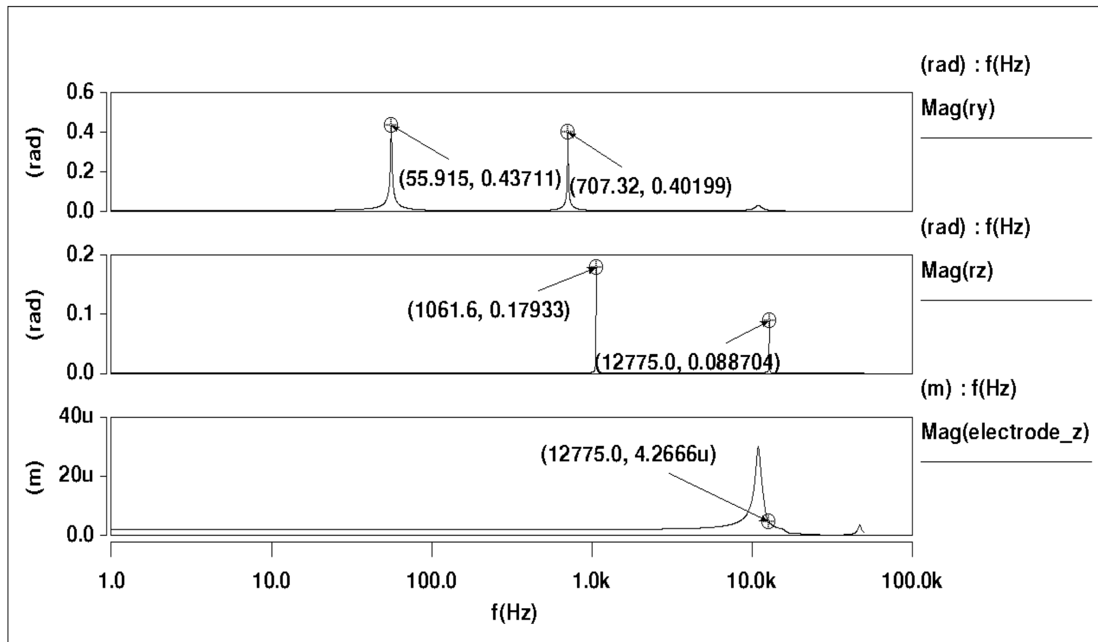

Figure 3.8. Pull-in effect study: (Top trace) rotational angle response of the low-frequency mode, (middle trace) rotational angle response of the low-frequency mode, and (bottom trace) deflection response of the electrodes.

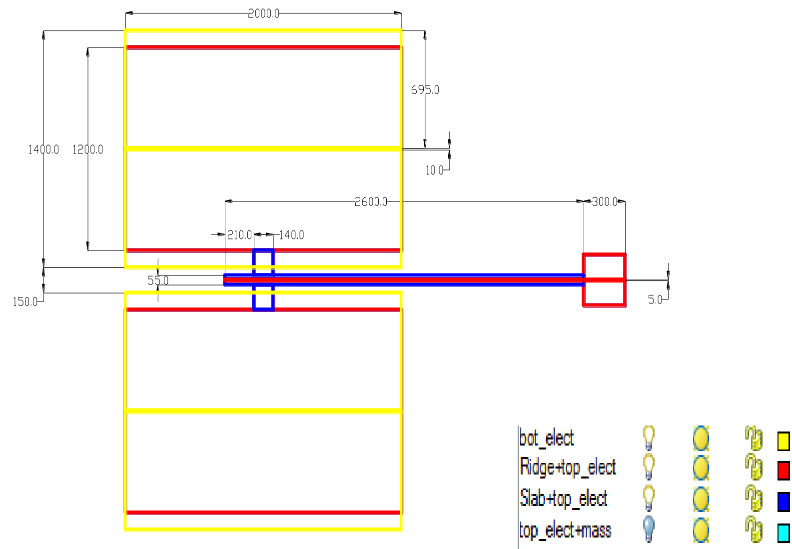

Figure 3.9. Layout of the optimized scanner design with a 2-µm-thick slab and a 2-µm-thick rib (Unit: µm). The layout is generated by Architect3D. Each color indicates same mask for micro-fabrication.

Chapter 4. OPTICAL ANALYSIS

Optimizing the light transmission and coupling between the tip of the input fiber and the cantilever beam requires using modal analysis and investigating the system's coupling efficiency. The waveguide for the scanner has a rib waveguide feature (Fig. 4.1), and it is made of an epoxy based SU-8 negative-tone photoresist. The wavelength range required for the proposed endoscopic application is 750 to 1300 nm. One way to predict the dimensions of the rib waveguide structure is to use the single mode conditions proposed by Soref [27]:

$$\frac{H}{\lambda}\sqrt{n_f^2 - n_s^2} \geq 1 \tag{4.1}$$

$$0.5 \leq r \equiv \frac{h}{H} < 1 \tag{4.2}$$

$$\frac{a}{b} = \frac{W}{H} \leq \left(\frac{q+4\pi b}{4\pi b}\right)\frac{1+0.3\sqrt{\left(\frac{q+4\pi b}{q+4\pi rb}\right)^2 - 1}}{\sqrt{\left(\frac{q+4\pi b}{q+4\pi rb}\right)^2 - 1}} \tag{4.3}$$

Where q is defined as:

$$q = \frac{\gamma_c}{\sqrt{n_f^2 - n_c^2}} + \frac{\gamma_s}{\sqrt{n_f^2 - n_s^2}} \tag{4.4}$$

Where $\gamma_c = \gamma_s = 1$ for TE modes and $\gamma_c = \frac{n_c^2}{n_f^2}$ and $\gamma_s = \frac{n_s^2}{n_f^2}$ for TM modes.

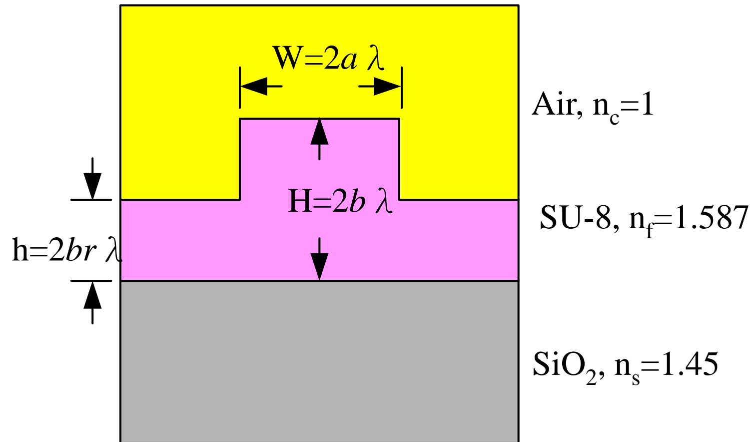

Figure 4.1. Cross section of the waveguide structure.

To have a single mode based on the above condition in TE polarization for any given H, the width W has to be less than or equal to the value on the curve (Fig. 4.2). By fixing the ratio r to 0.5, we generate a list of waveguide dimensions that we can use for the scanner design (Table 4.1). In case 1, the cross section of the rib waveguide has dimensions relative to the core diameter of a single mode fiber (SMF), which is an ideal geometry for the proposed end-butted coupling design. Table 4.2 summarizes the output power for different waveguide geometries, assuming that the same input is applied at the center of the rib waveguide.

Using modal analysis, based on a SU-8 (n = 1.57) rib waveguide structure with a width : ridge height : waveguide height ratio as shown in Table 4.1 and 4.2, the results confirm single mode operation for transverse mode input with wavelengths between 750 to 1300 nm. Figure 4.3 shows the modal profile of all three cases observed at 1 mm from the coupling end at λ= 800 nm. The profile is similar at 1300 nm.

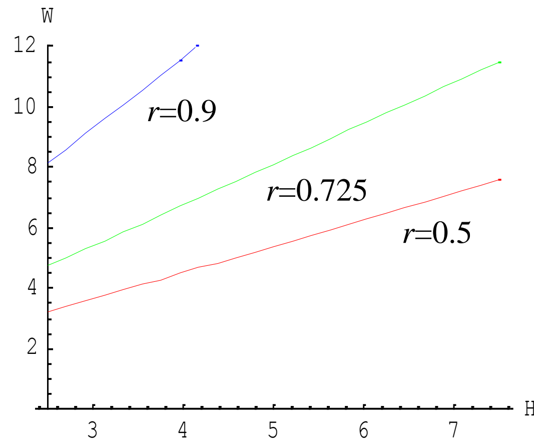

Figure 4.2. Waveguide width as a function of waveguide height at different r values.

Table 4.1. Waveguide Geometry (unit: μm).

	r	W	H	h
Case 1	0.5	8.	8.6	4.3
Case 2	0.5	5	5.2	2.6
Case 3	0.5	3	2.9	1.45

Table 4.2. Output power as a function of waveguide geometry (geometry unit: μm).

	r	W	H	h	Center of input	Output power
Case 1	0.5	8.	8.6	4.3	4.3	>90%
Case 2	0.5	5	5.2	2.6	2.6	~87%
Case 3	0.5	3	2.9	1.45	1.45	~61%

Case 1:

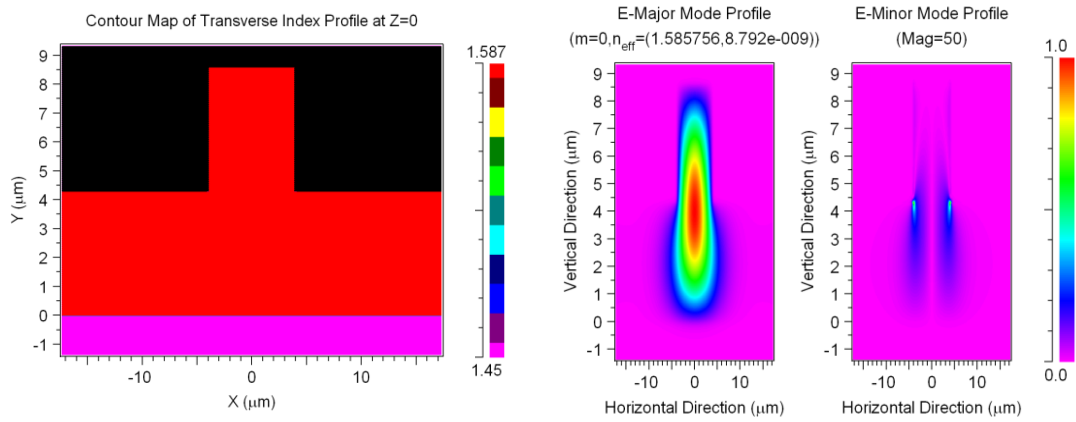

Case 2:

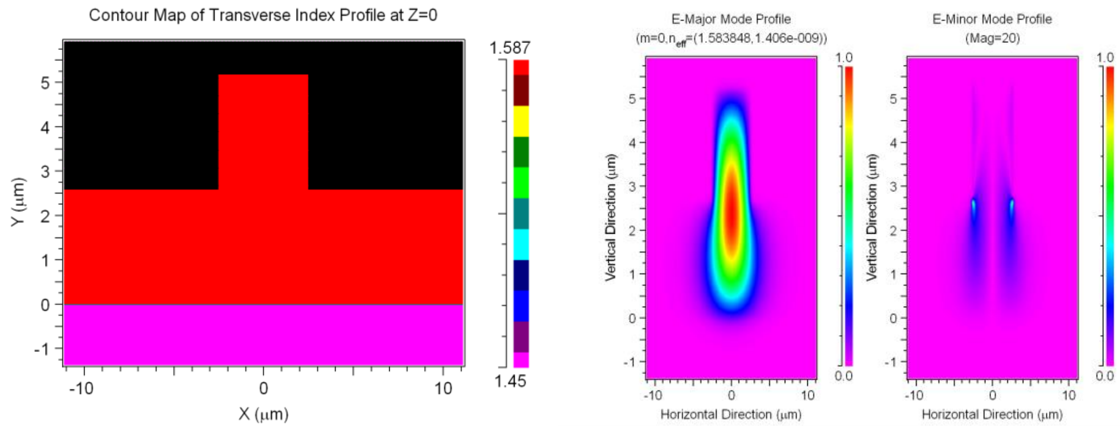

Case 3:

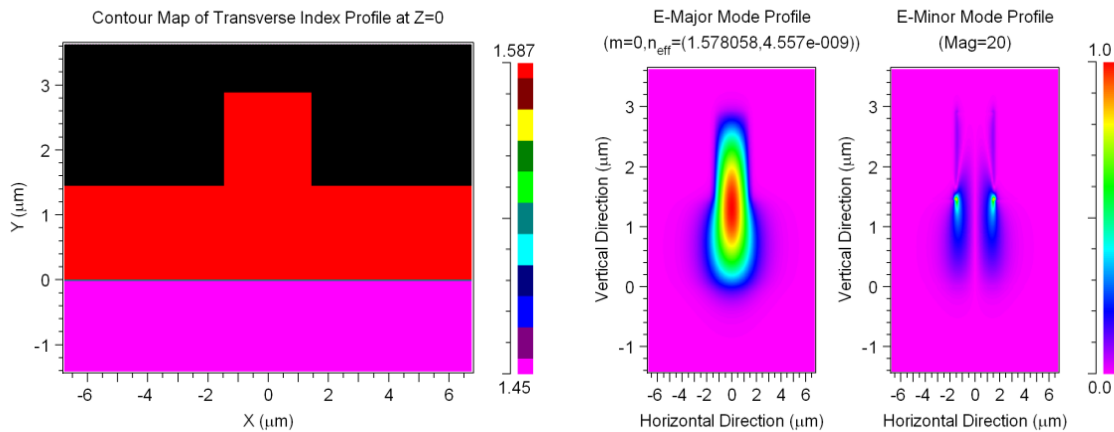

Figure 4.3. Modal profile of the waveguide scanner at λ= 800 nm.

Soref's equations are an approximation method to allow one to quickly check some of the critical design geometry in rib waveguide design to see if certain wavelengths are operating in a single-mode region. However, the method cannot analyze the wave coupling, produce the actual beam profile and the exact range of single mode operation and overall wave transmission in the waveguide. Therefore, the beam propagation method (BPM) in Rsoft software is used. An optical simulation using Rsoft beam propagation program software is performed to analyze the coupling efficiency. In order to simplify the analysis, it is assumed that the input to the waveguide is a single mode Gaussian beam and that scattering and absorption are negligible. In the previous multimode 100 µm × 85 µm × 2100 µm SU-8 rectangular waveguide, the combined loss from mode coupling, scattering and absorption is around 28.6% [28]. The simulation is based on a SU-8 (n = 1.57) rib waveguide structure with a width: waveguide height: ridge height ratio of 8: 4: 2. The results confirm single mode operation for transverse mode input with wavelengths between 750 and 1300 nm. As shown in Figure 4.4, a very low light loss for wavelengths operates between 0.7 and 1.3 µm. For an input with a Gaussian profile, the coupling efficiency for both wavelengths is around 95% for λ= 700 nm and λ= 1.3 µm. Minimum light attenuation is observed along the coupler and cantilever waveguide sections. The light throughput is roughly the same as the initial coupling efficiency (85% and 87% respectively). The same coupling efficiency and throughput is also observed if the input is a 0 order mode. The simulation also shows that the shape of the proof mass does not matter in the optical simulation, because single mode propagation is maintained as long as the input beam is confined mostly inside the ridge area of the waveguide. Table 4.3 summarizes all the key points of design dimensions this study got from both mechanical analysis (including FOV and line resolution) and optical analysis.

Table 4.3. A summarize of all the key points from each variant (unit: µm)

Pad		Arm		Waveguide			Proof mass		
Width	Length	Width	Length	Rib Width	Total Height	Rib Height	Width	Length	Height
750	1000	70	1000	5	5.2	2.6	60	60	4

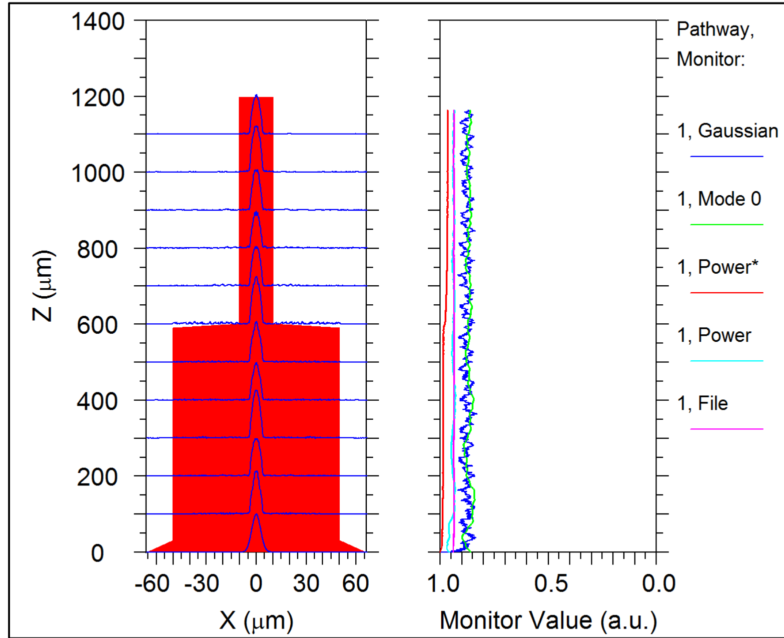

(a)

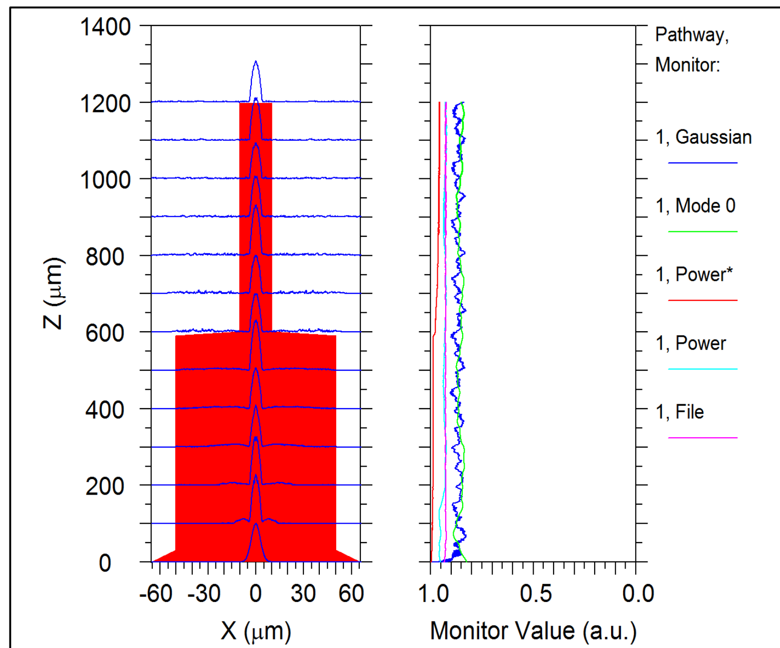

(b)

Figure 4.4. Wave propagation along the waveguide using a Gaussian beam profile for the 10 μm core input fiber (a) operating at 1.3 μm, (b) operating at 0.7 μm.

Chapter 5. DEVICE FABRICATION AND CHARACTERIZATION

In this chapter, fabrication processes of both PZT and electrostatic push-pull devices are explained, as well as fabrication difficulties. Additionally, the packaging design and scanning characteristics of fabricated devices are presented and discussed.

5.1 DEVICE FABRICATION

5.1.1 *SU-8 Introduction*

SU-8, first developed by IBM, is an epoxy-based negative resist. It consists of three components: resin SU-8, solvent, and photoacid generator (PAG). The resin is an epoxy made up of a bisphenol A novolac glycidyl ether. There are, in general, 8 epoxy groups in this molecule. That is where the name "8" in SU-8 comes from [29, 30]. In this study, all the SU-8s' used were purchased from MicroChem Corp. Based on the thickness (less than 5 µm) required in making the proposed scanner, SU-8 2 and SU-8 5 are selected for spin-coating various thin (1.5µm -5µm) SU-8 films. This SU-8 layer will be used as the main scanner material, including a cantilever waveguide with ridge and slab parts, and the SU-8 pads under metal electrodes.

5.1.2 *Fabrication Process of PZT Push-Pull Device*

The fabrication process is accomplished by both surface and bulk micromachining. The devices to be produced are fabricated from a single side polished 4 inch silicon wafer with a standard thickness of 525±25 µm with 1 µm wet thermal oxide and 200 nm LPCVD nitride deposited on both surfaces. The schematic diagram shown in Fig. 5.1 depicts the scanner fabrication process flow. For the fabrication of the actuator, the procedure is shown in the left column and waveguide portion is shown in the right column. The processing begins with a reactive ion etching (RIE) through the front side silicon oxide/nitride layer to open a window for the waveguide as illustrated in Fig. 5.1(a). Bottom electrodes made of 100 nm Pt and 20 nm Ti are done by an E-beam metal evaporation and a lift-off process (Fig. 5.1(b)).

The piezoelectric actuators used in this study are formed by sol-gel PZT process [31]. PZT (Lead Zirconate Titanate or $PbZr_{1-x}Ti_xO_3$) is a piezoelectric material often used in sensor and

actuator applications, such as nonvolatile memories [32-34], micro-cantilever actuator [35], piezoelectric diaphragms [36], ultrasonic microsensors [37], micromotors [38-40], micro-pumps [41], accelerometers [42-49], active slider in hard disk drivers [50-52] and chemical sensors [53]. Metal organic chemical vapor deposition (MOCVD) and sol-gel processing are the most promising techniques for the fabricating of PZT thin films among currently developed PZT films processes. Despite several advantages provided by MOCVD, sol-gel processing offers direct patterning of microstructures without using conventional etching, which is more beneficial to integrate with MEMS fabrication [54].

The top electrodes are patterned using the same method as described in the bottom electrodes. In Fig. 5.1(c), a ~10 μm thick positive photoresist (AZ P4620, AZ Electrode Materials) and PZT etching solution (BOE: HCl: NH_4OH: H_2O= 1:2:4:4) are used to pattern the PZT. After wet-etching, subsequent photolithography (again the same AZ P4620 is used) and deep RIE, fiber groove are formed. A 1 μm thick photoresist (AZ 1512, AZ Electronic Materials) layer is spin-coated on as a sacrificial layer to level the front side notch (Figure 5.1(c)). Then photolithography with a two-mask process is employed to define double-layer waveguide slabs and ridges using SU-8 2 (Fig. 5.1(d)). The critical alignment between the ridge and the flat rectangular waveguide section required a double side aligner system (EVG 620, EV Group). Finally, the device is released via bulk silicon etching using deep RIE from the backside (Fig. 5.1(e)).

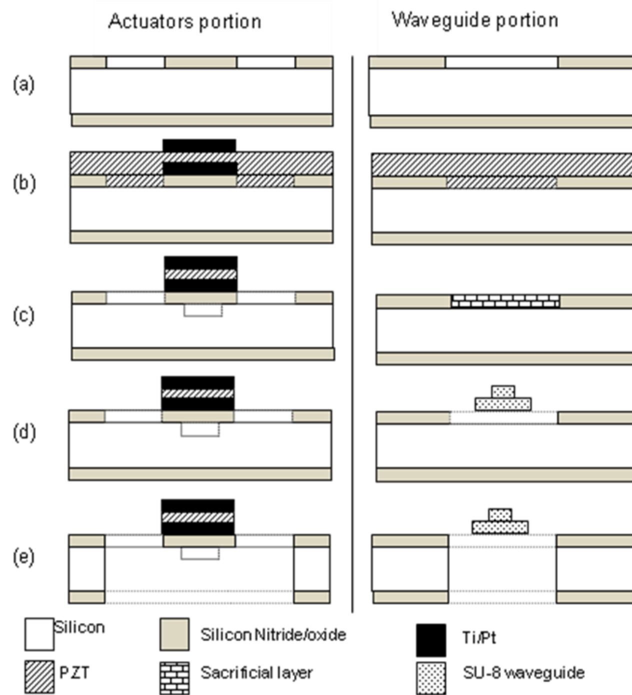

Figure 5.1. Fabrication process of mechanical based scanning endoscope. Left: Actuators portion. Right: Waveguide portion. (a) RIE etch front side oxide/nitride open window. (b) Deposit bottom electrode/PZT layer/up electrode. (c) Use wet etching to pattern PZT actuator, deep-RIE to etch front side fiber grooves, and pattern sacrificial layer to level nitride/oxide opening. (d) Spin and develop double-layer SU-8 2 waveguide cantilever. (e) Backside etch-through to release actuators and waveguide tips.

The two parallel PZT actuators composed of $PbZr_{0.52}Ti_{0.48}O_3$ thin films are prepared by a sol-gel method on a $Pt/Ti/Si_3N_4/SiO_2/Si$ substrate. The precursor solutions of PZT in appropriate chemical formulas are prepared using lead acetate trihydrate, tetraisopropyl orthotitanate, and zirconium propoxide (70% in n-propanol) in 2-methoxyethanol and acetic acid as the solvent. Before PZT sol is implemented, the bottom electrodes are annealed at 800 °C for 45 minutes at a heating rate of 10 °C per min and natural cooling to room temperature inside the furnace. PZT thin films are deposited onto $Pt/Ti/Si_3N_4/SiO_2/Si$ substrates by spin coating at 4500 rpm for 20s. After PZT deposition, solvent removal is accomplished by heat treatment at 650 °C for 10 min in a preheated furnace. A multilayer approach is used to prepare thicker PZT films, where each layer is ~350 nm.

The PZT etch solution consists of 10 ml BOE + 20 ml HCl + 40 ml NH_4OH in 40 ml H_2O (1:2:4:4). A dip in high-concentration HNO_3 solution and then cleaned by DI water are employed to remove two intermediate products PbClF and $PbCl_2$. The roles of individual component have already been reported [55]. The PZT etch rate using this recipe is ~50 nm/min.

5.1.3 *Fabrication Process of Electrostatic Push-Pull Scanner*

SU-8 waveguide layer and bottom electrode

The electrostatic scanner follows a similar process to the piezoelectric scanner to keep the fabrication procedure consistent (Figure 5.2). The devices to be produced are fabricated from a p-type single side polished 4 inch silicon wafer with a standard thickness of 525±25 µm. The substrate is cleaned by immersing a Piranha solution (H_2SO_4: H_2O_2= 4:1) to clean organic residues off the substrate. The wafer is then rinsed thoroughly in deionized (DI) water, dried using a spin rinse dryer (SRD), and then dehydrated on a hotplate at 200℃ for 10 minutes. The processing begins with a two-layer SU-8 structures lithographic process. The first layer (2 µm) of SU-8 2 (MicroChem, MA) is spun coated onto the silicon substrate to fabricate the scanner body and waveguide slab part, following instructions provided by the MicroChem Corp. To fabricate the waveguide rib part, another 2 µm-thickness SU-8 2 resist is spun and exposed on top of the first layer after post-exposure bake (PEB) process of the first SU-8 layer. In order to reduce the extrinsic stress that occurs during prebaking, the temperature is first held at 70 ℃ for one minute before continuing ramping from 70 ℃ to 105℃ at a rate of 3℃/min. We then hold the sample at that temperature for 15 minutes before gradually ramping down to room temperature at a rate of 2 ℃/min.

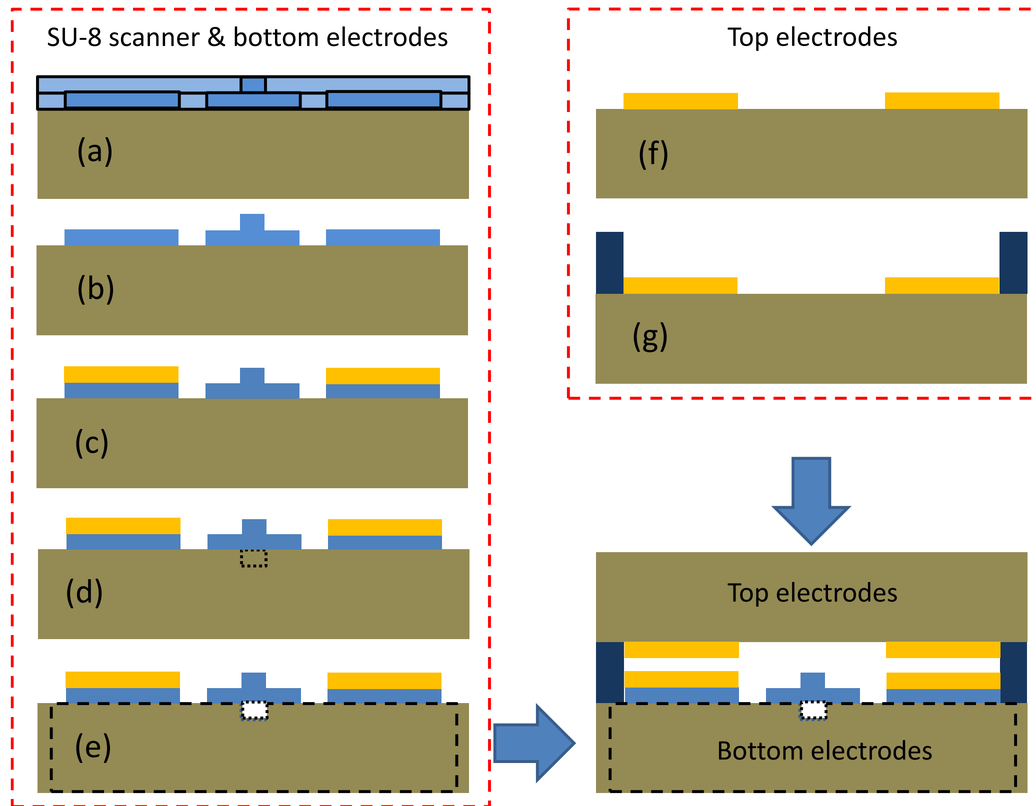

Figure 5.2. Fabrication process of electrostatic scanner. (a)-(e): scanner body and bottom electrodes (f)-(g): top electrodes. (a) Double-layer photolithography process to define rib shape waveguide and scanner pads (b) Development process to create SU-8 waveguide and body (c) Au/Ti metal thin films are deposited and patterned by lift-off process (d) Front side fiber grooves are patterned and deep etched using DRIE (e) the scanner (bottom electrode and waveguide) were released by DRIE again from the backside of the wafer (e) Backside etch-through to release actuators and waveguide tips (f) top electrodes is deposited and patterned on a second silicon wafer (g) SU-8 spacers are spun and patterned. Finally, the top and bottom electrodes can be assembled by the aid of an extra holder.

Both waveguide slab and ridge are transferred from a soda lime with chromium (Cr) coating mask to the double-layer SU-8 2 film by exposing the film on a contact aligner with a mercury broadband light source. Based on repeated trials, it is found that the film reproduces best features when exposed at 130 mJ/cm^2. For the PEB, the wafer is again placed on a hotplate for 1 minute at 70 °C, holding for 1 minute, then ramping from 70 °C to 105°C at a rate of 3°C/min. We hold the sample

at that temperature for another 1 minute, gradually ramping down to room temperature for 30 minutes. This cooling (relaxation) period is much longer than the post bake time recommended by the manufacturer. This greatly reduces the internal stress, which will be discussed in more detail in the results later.

After cooling the film to room temperature, the double-layer SU-8 film is then developed in SU-8 developer (PGMEA, an ethyl lactate and diacetone alcohol, MicoChem Corp., MA) for about 1 minute with mild agitation. The wafer is then rinsed thoroughly in isopropyl alcohol (IPA) for another 1 minute, and dried using SRD.

Metal electrodes made with 20 nm titanium and 200 nm gold are done by an E-beam evaporation deposition and a lift-off process. Prior to metal deposition, a layer of negative photoresist NR9-3000PY (Futurrex Inc) is spun onto the SU-8 layer. The pattern is transferred from a soda lime mask to the resist to define electrodes area. After metal deposition, the wafer is immersed in an acetone solution. Similar to previous process, subsequent photolithography (again the same AZ P4620 is used) and deep RIE, fiber groove are formed. Finally the device (scanner and bottom electrodes) is released via bulk silicon etching using deep-RIE from the backside.

Top Electrode

The fabrication process of the top electrode of the device is a relatively easy two-step micro-fabrication process. In a second 4 inch silicon wafer, first the substrate is again followed the similar clean and dry procedure as mentioned above. A photolithography process is followed to define the top electrodes area, an e-beam evaporator system is used again to deposit the titanium adhesion layer and the Au electrode. The metal thin films are then patterned by lift-off process. Secondly a SU-8 spacer is spun and patterned to form a SU-8 spacer. By the aid of an extra packaging design, which will be introduced in the next section, the top electrodes are able to be aligned with the scanner and the bottom electrodes are constructed with the parallel-plates electrostatic actuation.

5.1.4 *Results and Discussion*

Double-layer SU-8 Patterning Problems

Both PZT and capacitor devices are successfully fabricated (Figure 5.3). However, due to their large aspect ratio and residual stress, the fabricated waveguides appear bent (Figure 5.4(a)). The reason is that due to the mismatch of the coefficient of thermal expansion (CTE) between SU-8

and the commonly used substrate (Si), a great amount of thermal stress will be induced during the baking process [56-58]. This problem has been resolved by carefully controlling the baking process of the SU-8 waveguide layers. Using more gradual heating and cooling results in a straighter beam (Figure 5.4(b)). The new baking recipe also helps resolve the adhesion problem between the SU8 waveguide and the silicon nitride substrate. In the earlier baking recipe, the SU-8 tended to peel off the nitride surface (Figure 5.5(a)) because the thermal conductivity of nitride is lower than silicon. After a higher bake temperature is employed (originally 65℃ for soft bake and 95℃ for post-exposure bake, here we change to 70℃ and 105℃ respectively), the delaminating problem is solved (Fig. 5.5(b)).

Overall the fabrication procedure is robust, despite requiring 9 masks for PZT device and 7 masks for electrostatic device (including top electrode) respectively. The average deviation in the alignment is ~5% for the actuator and ~20% for the rib waveguide structure in a single batch. Figure 5.6 shows an example of the ridge misaligned with the bottom slab.

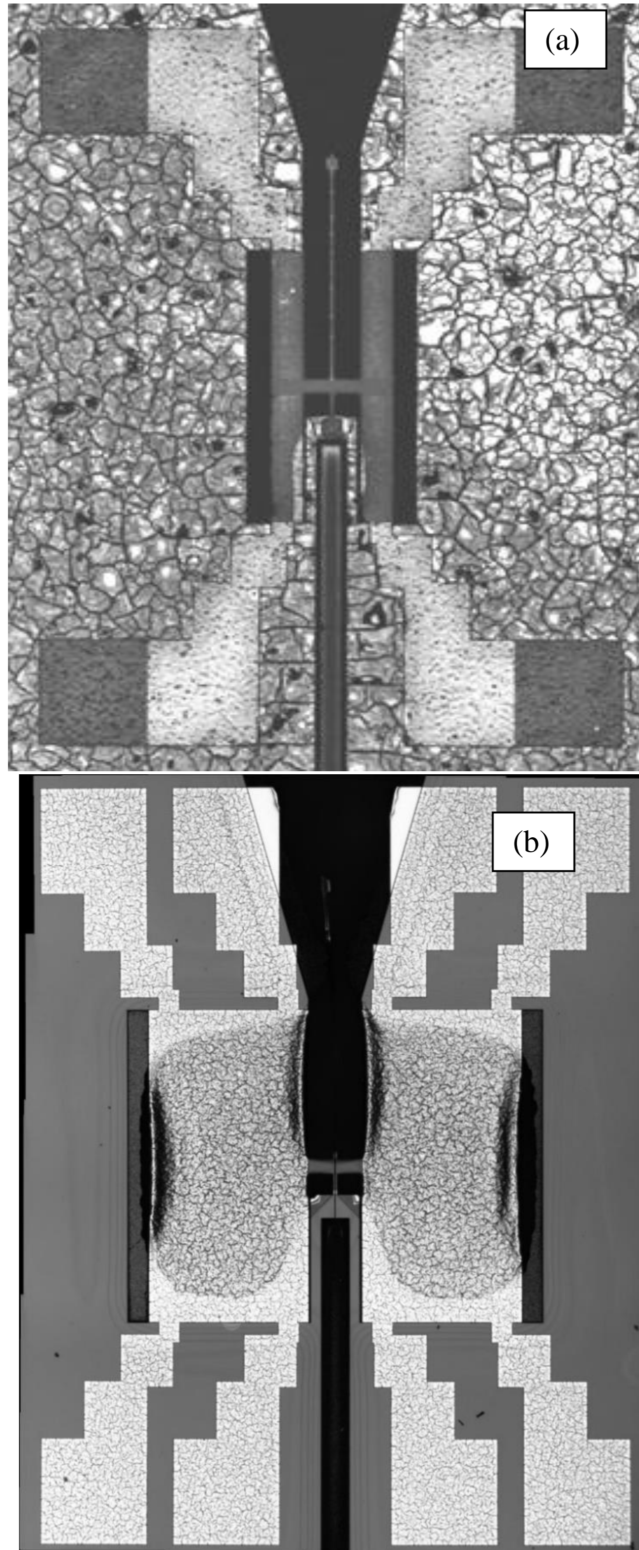

Figure 5.3. Top view of the micro-fabricated resonant push-pull scanners. (a): PZT scanner (before DRIE etch through), and (b), electrostatic scanner (scanner and bottom electrodes only).

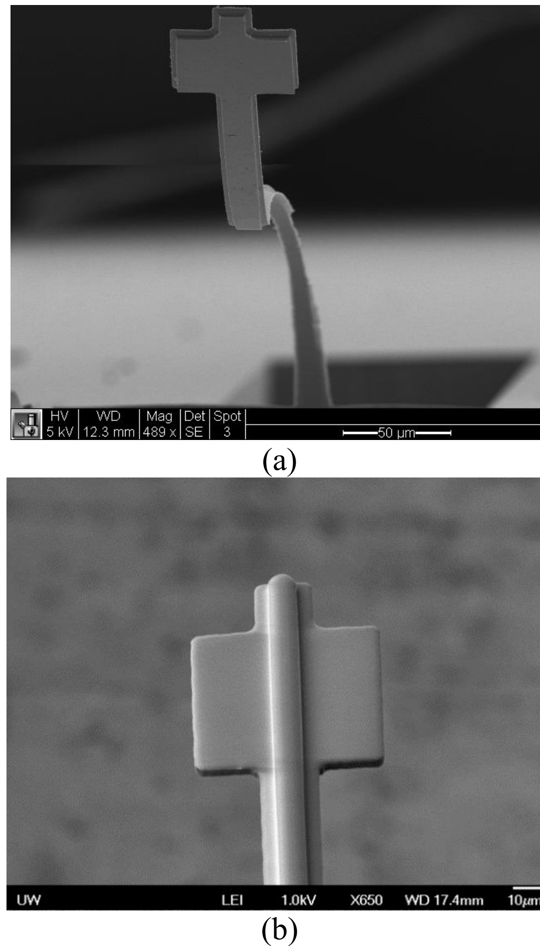

Figure 5.4. SEM pictures of (a) a curling double-layer SU-8 waveguide, and (b) a straight double-layer SU-8 waveguide after modifying SU-8 lithographic recipe.

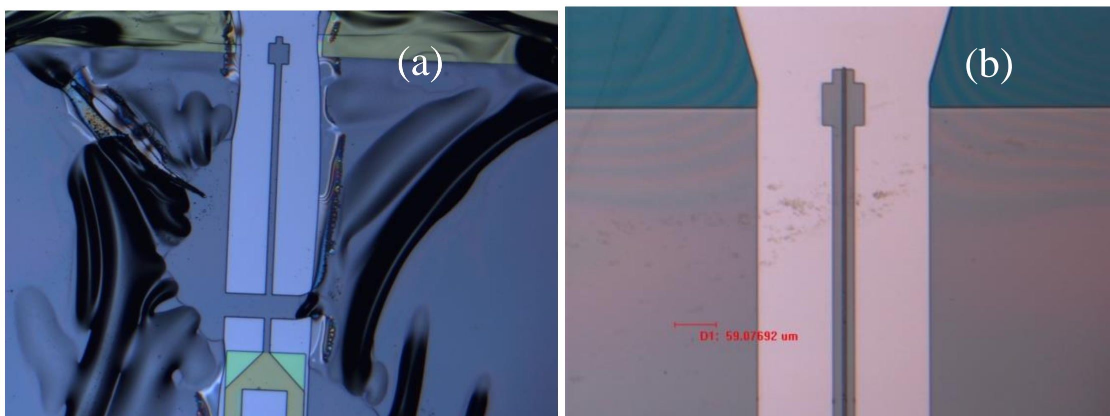

Figure 5.5. Microscopic pictures show lithographic result of double-layer SU-8 layer on top of nitride/silicon wafer. (a) Lower baking temperature (65°C/95°C) (b) Higher baking temperature (70°C/105°C).

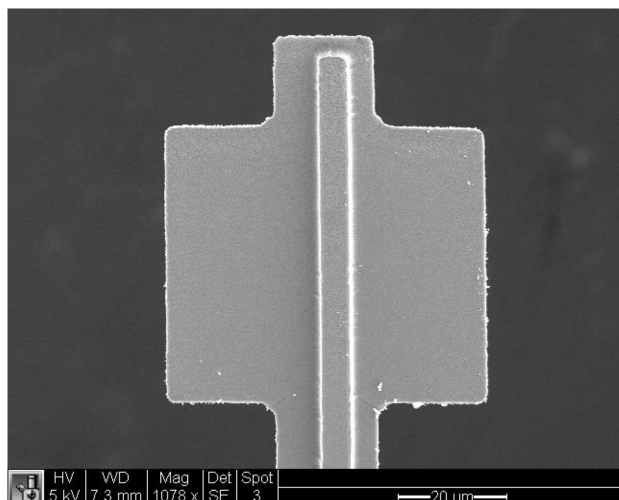

Figure 5.6. SEM picture shows a misaligned double-layer SU-8 waveguide.

Sol-Gel PZT Defect Problem

Cracks and pin holes are found in the current PZT film with a patterned bottom electrode (Fig. 5.7(a)). Cracks are formed from stress gradients developed during the sol-gel drying stage. As the solvent evaporates, the concentration increases and condenses to form a 3-dimensional gel network [54]. The large stress gradient occurs as the solvent removes from the film surface in the beginning, and cracks are much more likely to develop as the film thickness increases. In our PZT sol-gel process, the main difference between fig. 5.7 (a) and (b) is that in fig. 5.7(a), PZT thin film is spun on a patterned bottom electrode; however, this is not the case when the bottom electrode is not patterned (Fig. 5.7(b)). After the lift-off process, it is possible that the metal surface is not properly cleaned and metal particles are stuck on the surface, which subsequently causes the defects to form. Another probable cause might be the aggregation of certain components. It is found that chemical reaction limited aggregation is responsible for most of the sol aging, followed by diffusion limited aggregation [59]. At the beginning, particles grow by reaction between initial polymers and particles. As the particle number-density increases, a particle-particle aggregation characterized by an exponential growth law becomes the predominant mechanism [60]. In the sol-gel solution or certain hydrophilic components, due to their limited shelf life, start to colligate or change their properties, thus causing these unwanted particles to form over the film over time. However, so far the film has only been inspected using a microscope. The sol-gel PZT quality needs to be examined more carefully by XRD (X-ray diffraction) in the near future.

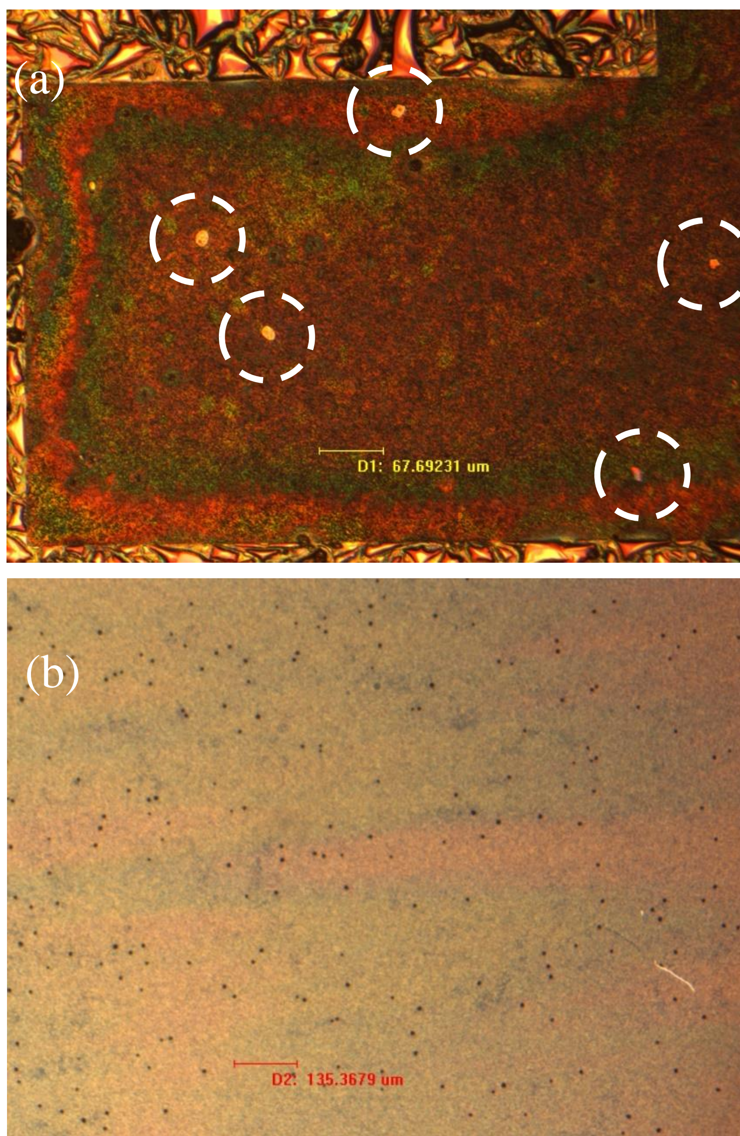

Figure 5.7. (a) Sol-gel PZT thin film on a patterned bottom electrodes. (b) The same sol-gel PZT on an un-patterned bottom electrode. The film appears defect-free.

Refinement of Piezoelectric actuator

The most difficult technical challenge in developing our proposed piezoelectric push-pull actuator is its defects (cracks). Currently, successful processes of PZT films include sputtering [61-64], direct bonding [65, 66], screen printing [67], metal organic chemical vapor deposition (MOCVD) [68], and sol-gel processing [69-72]. As we discussed previously, sol-gel processing offers unique advantages such as inexpensive, suitable for mass production, compatible with MEMS fabrication process, and it is easy to control the stoichiometric chemical composition of PZT films. This is extremely important for complex oxides such as PZT, because their physical properties strongly depend on the precise control of the chemical composition. Since it is more beneficial to fabricate PZT films using sol-gel processing, currently there are commercially available PZT solutions (PZT-20, Kojundo Chemical Co., Japan) with Pb/Zr/Ti ratio of 120/52/48 which can be used as a precursor solution (Fig. 5.8) [73]. It is worth giving it a try due to lots of advantages. There are many other reasons for developing a piezoelectric actuator: 1) to save the work of preparing PZT sol-gel precursors, which was previously unstable and unreliable process in this study; 2) to eliminate the need of parallel electrodes which cause a robustness issue for electrostatic design; 3) to dramatically reduce the device footprint due to the requirement of adding extra holders; and 4) to avoid problems based on current electrostatic design imperfection, such as alignment issue for both top and bottom electrodes, imprecision of the top/bottom electrodes gap space, etc.

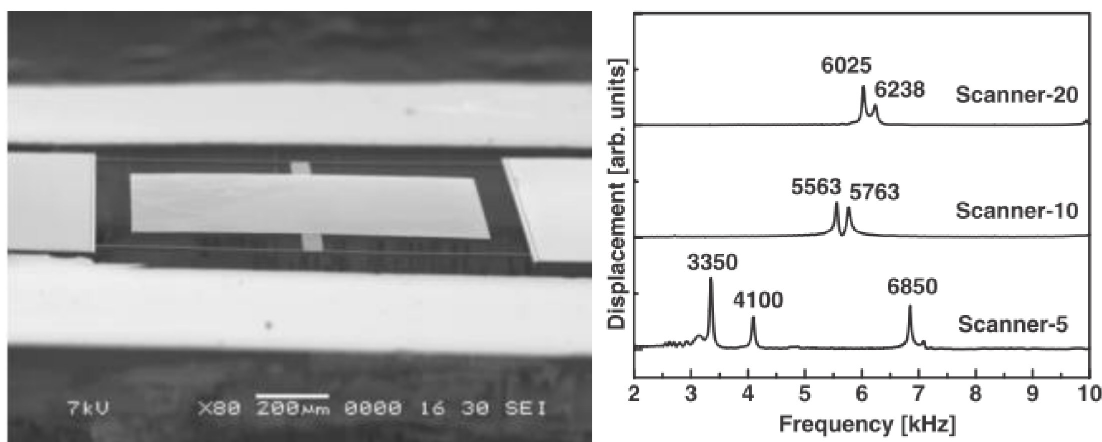

Figure 5.8. SEM image of the micro scanner made of a commercial available PZT solution (left) and power spectrum as a function of the frequency for the micro scanners. The numbers above the peaks denotes the frequency at the peak in Hz (right) [73].

The Challenges of Plasma Etching

Reactive Ion Etching (RIE) is widely used in the semiconductor industry and in MEMS due to the fact that the dry process is relatively robust, near vertical etch profile, and highly accurate reproduction of photoresist dimensions to closely spaced structures (compared to wet etch), which are great for pattern transfer requirements in the IC manufacturing industry. The RIE etching is done in a vacuum chamber by reactive gases excited by RF fields. There are basically two kinds of species generated by this plasma environment: ionic species and very reactive excited molecules. So the RIE etch process is basically a combination of both physical etching of ion bombardment (which is also isotropic since the ions are accelerated by the RF field) and chemical etching by the excited reactants [74].

Deep reactive-ion etching (DRIE) is an extension of reactive ion etching (RIE) with highly anisotropic etch process used to create high aspect ratio structures (holes/trenches) in wafers [75]. The technology used in this experiment to create deep penetration in silicon wafers called Bosch process [76]. The Bosch process, named after the German company Robert Bosch GmbH which developed the process, SF_6 and C_4F_8 gases are pulsed (Figure 5.9) [77]. In the first couple seconds, an SF_6 pulse starts to etch the silicon surface with the same mechanism as RIE etch. The etching profile is not completely anisotropic. Then a C_4F_8 pulse is applied, and a fluoropolymer protective film is deposited all over the wafer. The next SF_6 etching pulse removes the polymer film from the hole/trench bottom by ion-assisted etching, but the sidewalls remain protected due to the fact that the ion bombardment is more directional. After removing the protective film from the trench bottom, both SF_6 etching and ion bombardment etching of silicon can continue. By repeating this etch/passivation steps, the etch front can go deeper and deeper with minimum isotropic sidewalls and create high aspect ratio structures.

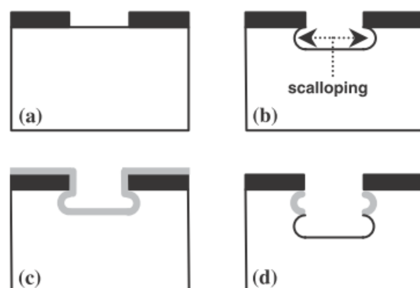

Figure 5.9. Schematic of Bosch process: (a) PR opening for DRIE; (b) SF_6 isotropic etch step; (c) C_4F_8 passivation layer deposition; (d) next etch step. Etch and passivation pulses repeated [77].

Once the chrome masks are made, all features are fixed and can't be revised. When fabricating the current prototypes, a number of flaws were found in the original design. In order to understand how the DRIE limitations affect to our MEMS device, a DRIE etch experiment is conducted to see how the current etch recipe relates to the fabrication imperfection. A single experiment with a test structure that contains two kinds of different linewidth (30 µm and 280 µm respectively) trenches are etched simultaneously on the same wafer using the inductively coupled plasma (ICP) RIE (Oxford Instruments, UK). The etch recipe is shown in Table 5.1. Figure 5.10 shows two scanning electron microscope pictures of the cross-section view of the etch results. In this cross-section view of the etching profile, couple parameters are carefully examined including the aspect ratio dependent etch (ARDE), sidewall angle (SWA) and the bottom curvature.

Table 5.1. Parameters in the cyclic Bosch process in DRIE.

Cyclic step	Time (s)	C_4F_8 (sccm)	SF_6 (sccm)	ICP Power (W)	DC Bias (V)
Etch	7	100	1	1650	130 - 150
Passivation	5	1	100	1500	60- 90

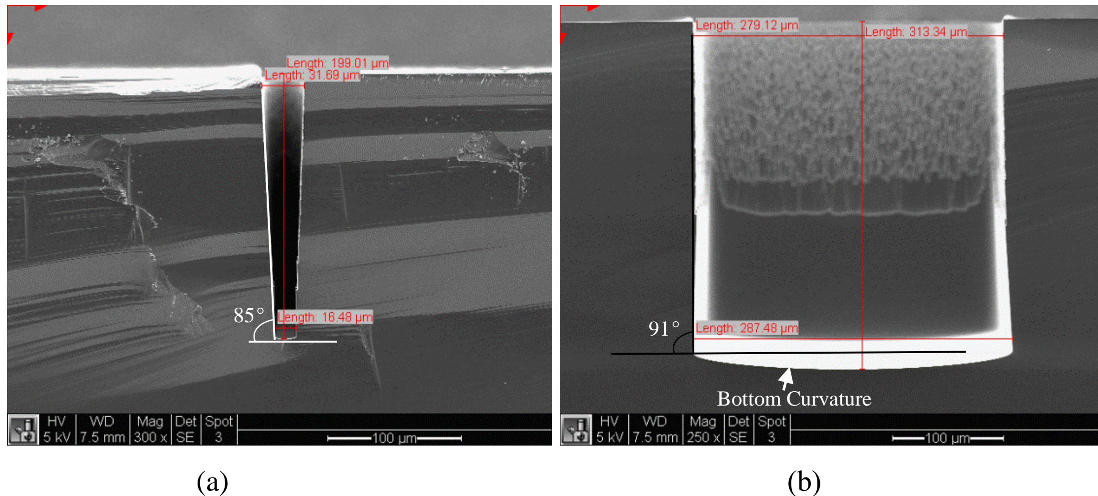

(a) (b)

Figure 5.10. SEM pictures show RIE lag during DRIE etch. Under the same etch condition and duration, (a) a smaller etch rate for a narrower line and (b), a faster etch rate for a wider line.

RIE Leg

During the DRIE process, a well-understood phenomenon called "RIE lag" manifests itself: under the same etch condition and etch duration, smaller features etch slower than larger features [78, 79]. In Figure 5.10, the etch depth of 30 µm and 280 µm width trenches are about 200 µm and 313 µm respectively. This is because gas conductance in deep narrow trenches is low and the reactants generated by DRIE ICP plasma simply cannot reach the bottom effectively. This phenomenon is also called "Aspect ratio dependent etch, ARDE". This is a problem because masks layout often make use of different density and linewidth within a single MEMS device. Fortunately in this step for making the MEMS backside etch through mask design, all the linewidths used to release the MEMS device are pretty even, so the RIE lag can be ignored.

Sidewall Angle

In order to release the MEMS device with suspended actuators and waveguides, the last step of the fabrication process is photolithography patterning on the backside of the wafer using a double-side aligner, then deep-RIE etch through the wafer from the backside. In this step, pattern transform accuracy plays a very important role. Even the photolithography misalignment can be eliminated when operating the double side aligner, the etch profile still needs to be carefully controlled to achieve the accurate pattern transform from the backside of the wafer to the devices. In other

words, a vertical etch profile (90 degree) is desired. Figure 5.10 (a) shows a tapered profile of the etched trench which is about 85 degree and Figure 5. 10 (b) shows a vertical (nearly 90 degree) sidewall angle which meets our requirements in this experiment. A tapered profile often results from deposition on the sidewall during etching, effectively increasing the mask width as etching progress. It is more obvious especially in the high aspect ratio structures. To avoid this tapered profile, the DRIE etch recipe needs to be modified to reduce passivation on the sidewall. However, since the tapered profile only appears when the line width is smaller than 100 μm, and all the linewidths of the backside patterns are greater than 250 μm in our design, this issue can be ignored.

Bottom curvature

During plasma etching, the exposure of the surface to plasma can be a harsh environment that damages the surface of the device which is being formed. The bottom curvature of the etch front after DRIE (Fig. 5.10) is one of the challenges because an uneven etch front means that "over etch" step is needed to fully clear residue at the bottom of the feature. Fig. 5.11 (a) shows silicon residue around the etched features and Fig. 5.11 (b) shows the over-etch result. When the over etch step is applied, the plasma etch-induced damage would happen to the exposed area. However, if it's under-etched, beam will not be released. The bottom curvature can be seen as an isotropic etch front only happening in the bottom because the sidewalls are protected by the polymers during the etch process, and it usually results in the isotropic chemical etch during the Bosch Process. In Bosch process, every single etch step is slightly isotropic. After thousands of repeating etch and passivation steps, the isotropic etch profile becomes significant.

Due to the limitations of resources and equipment, this issue cannot be solved completely. Currently the bottom curvature can be slightly improved by increasing the ion bombardment and reducing the chemical etch during the Bosch process to increase directional etch and minimize isotropic etch. However, a modified recipe will need to consider the trade-off between all parameter-related issues such as etch rate, etch profile which we discussed in the previous section. To solve this problem, the next prototype will use a revised mask design to protect the waveguide, or a slightly thicker SU-8 waveguide will be fabricated to compensate for over-etching. In the future, an etch stop layer is suggested to protect the MEMS scanner in the front side during the DRIE etch and over-etch steps.

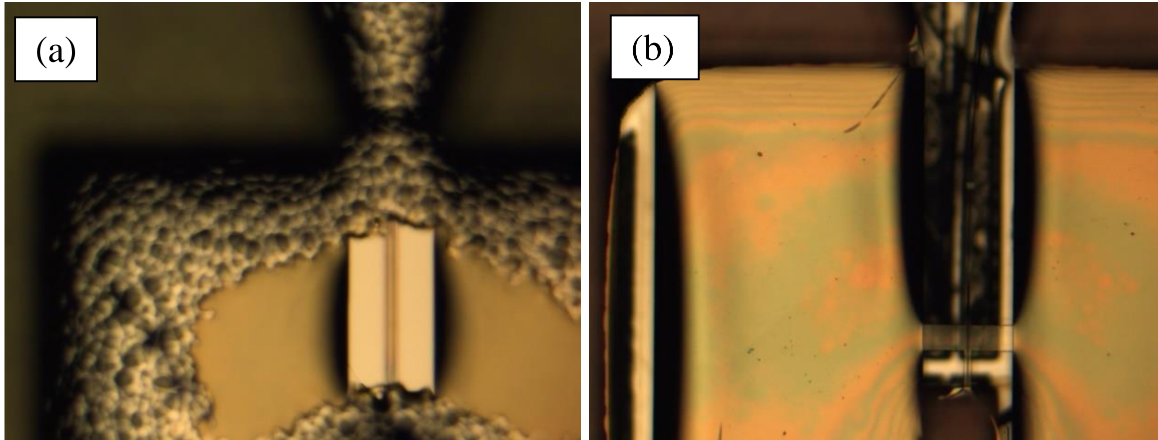

Figure 5.11. Microscope pictures show (a) after 750 DRIE loops, only the center of the backside open window is etched through the front side due to the non-uniformity of DIRE. There are still silicon residues around the corners, and (b) adding 30 DRIE loops more to clean the silicon residue around the corner.

SU-8 Waveguides Dry Etching Yield

The final deep RIE process from the backside of the silicon wafer to release the device as well as SU-8 waveguide is currently the most difficult process in the whole fabrication flow. Due to the fact that the etch products during the etch process heavily attack the epoxy-based waveguide as well after the silicon substrate is etched through and the waveguide is exposed, it is very difficult to stop the etch process perfectly at the right timing that the waveguides are just released. Even running the process very slowly and carefully before the wafer is etched through, the deep RIE still causes non-uniformity issue across the wafer. In other words, during the DRIE etch process, the etch rate in some areas is etched faster than other areas, causing obvious under-etch or/and over-etch appearing on the same wafer. In this study, the yield of the current waveguide process is only about 10% (10 devices out of 100 in a single 4 inch wafer).

Since the epoxy based SU-8 waveguide in this study is a long, slender and relatively soft structure compared to the traditional silicon/ silicon oxide/ silicon nitride/ carbon/ metal cantilevers, one of the major technology issues in surface micromachining is how to release this structure without a stiction problem in order to make it free standing. All the current wet etching techniques are not practical due to the fragileness of the structure. One possible solution to improve this process technology and increase the yield of SU-8 waveguide is to add a thin silicon oxide

layer below SU-8 waveguide layer (Fig 5.12). In MEMS applications, silicon dioxide is widely used as “etch stop layer” due to its high selectivity to silicon (>100:1) under a plasma etch process [80]. When deep RIE etches from the backside, it can uniformly stop at the etch stop layer. Then the thin silicon oxide layer can be removed by a dry isotropic etch process called HF vapor-phase etching to remove the underneath silicon oxide from the front side of a silicon wafer [81].

Fig. 5.13 is a schematic drawing of a pre-objective MEMS resonant scanner [82]. This device features monolithic integration of the MEMS waveguide, actuator, light source and detector. The cantilever beam is free to resonate in 1D or 2D and a single mode fiber which couples the light from a laser diode is mounted on top of the silicon cantilever. The waveguide, however, is proposed to be fabricated using the traditional silicon cantilever beams [83], which has been developed for decades and provides an alternative to micro-fabricate a more robust and reliable MEMS cantilever for vibration.

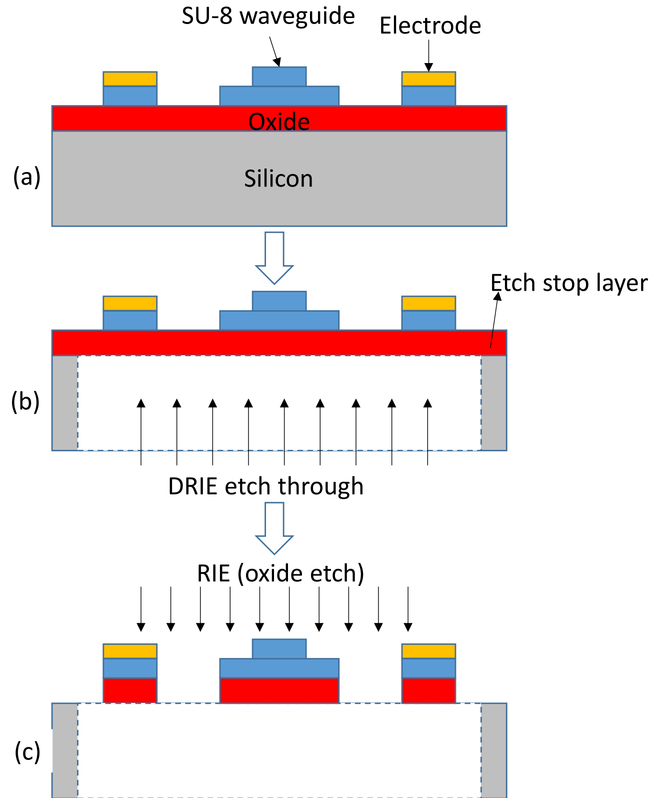

Figure 5.12. (a) The original scanner design with added thin silicon oxide layer between waveguide and silicon. (b) DRIE etch through from the back side of the silicon wafer. The DRIE etch will stop automatically at the etch stop layer (oxide). (c) Use RIE oxide etch to clean oxide from the front side of the device. Oxide will remain under the waveguide and pads area.

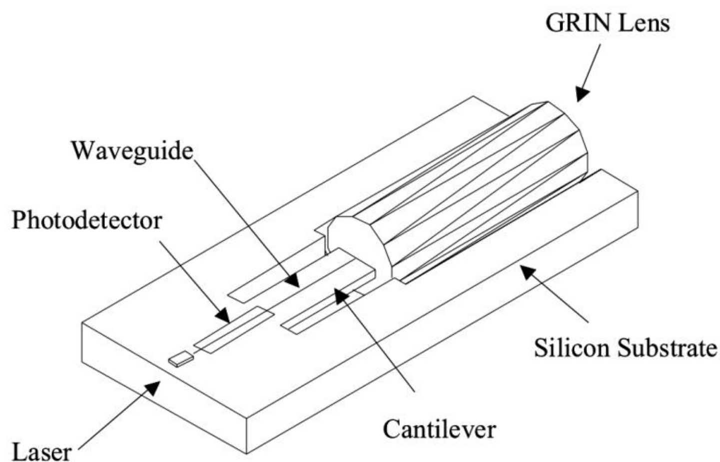

Figure 5.13. Schematic diagram of a proposed MEMS resonant scanner [82].

Over-exposure Issue Due to the Lateral UV-Transmissive

In the fabrication process of making electrostatic scanner, the bottom electrode is patterned using a lift-off process, which requires a photolithography step using negative-tone photoresist NR9-3000PY to spin and exposure on top of the SU-8 pads layer. However, the lift-off results of the metal electrodes are failed during the first couple runs under the default lithography recipe recommended by the official datasheets (Fig. 5.14(a)). The reason is because the SU-8 layer, here in this fabrication step, plays a role of UV-transmissive substrates, which is usually a transparent polymers under the photolithography layer, laterally guide light along the substrate (Fig. 5.15), cause reflections from the bottom substrate (silicon, in this case) and reduce the lateral resolution. To solve this problem, putting extra UV-absorbing (or anti-reflection coating, ARC) films between Silicon/SU-8 and SU-8/NR9-3000PY interfaces will dramatically reduce the UV transmissive effect. In our modified recipe, a reduced exposure dose for NR9-3000PY to effectively minimize the exceeding UV light helps, as well as increasing development duration in the NR9-3000PY developer (RD6 Developer, Futurrex INC., NJ, USA) for better un-cross-linked resist removal (Fig. 5.14(b)).

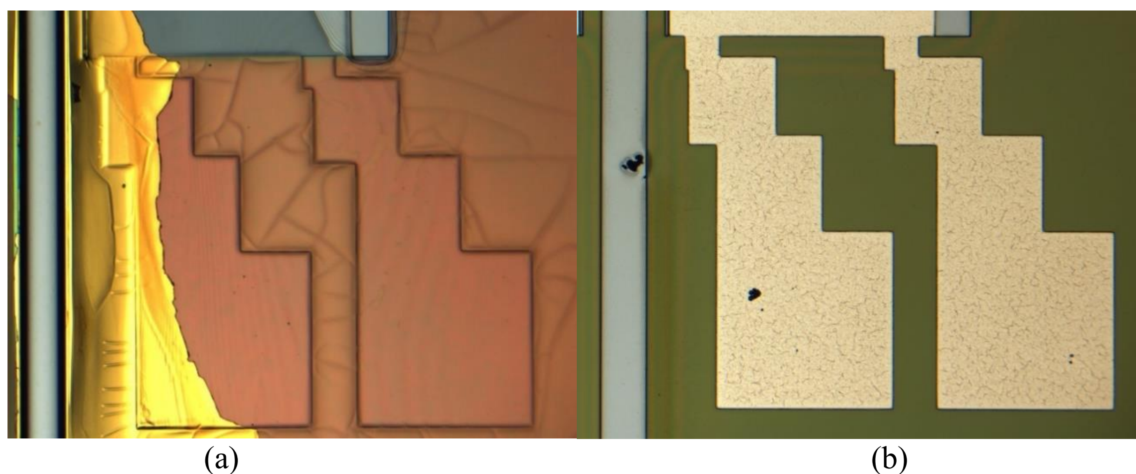

(a) (b)

Figure 5.14. (a) Failed lift-off process to pattern bottom electrodes due to the UV-trasmissive effect. (b): a successful bottom electrodes patterning.

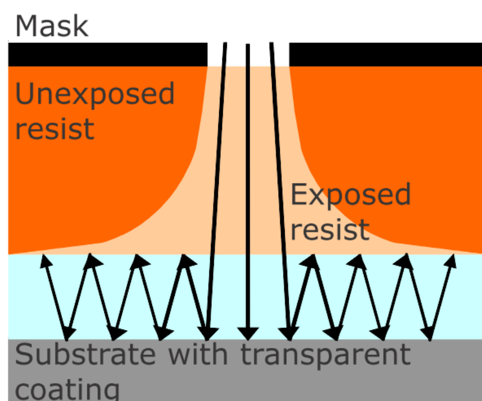

Figure 5.15. Schematic of the lateral UV-transmissive effect in a substrate with transparent coating. Lateral resolution of the photoresist can be affected due to the effect [84].

5.2 DEVICE PACKAGE DESIGN

The packaging design is required in this study due to the fact that 1) the scanner needs to be durable enough to withstand situations similar to what the device will experience from contacting with tissue under normal use, and 2) to secure the MEMS waveguide with an optical component, a focusing gradient index (GRIN) lens. For the future endoscopic application, the performance will be tested under a range of temperatures and humidity using a controlled environmental chamber. We also need to test the ability of the packaging to withstand an environment similar to clinical use. This includes the ability for the packaging to seal properly and to be durable enough to withstand situations similar to what the device will experience from contact with tissue under normal use. Here an 8.0 mm × 8.0 mm × 1.0 mm holder made of acrylic-based photopolymer materials is designed and fabricated using a multi-material 3-dimensional printing system (Connex 350, Objet Geometries Ltd) with 16-micrometer accuracy (Fig. 5.16). The holder is made of 2 parts, and they are combined to form a ferrule to hold the GRIN lens at a predetermined distance from the tip of the cantilever waveguide as shown in Fig. 5.17. Our proposed GRIN lens is fixed and disposed beyond the end of the cantilever inside a proposed holder, relaying the image of the waveguide to an eventual object plane. Based on calculation, the angular deflection of the proposed scanning system is only 5 degrees total (2.5 degrees each side). The aberrations and vignetting are minimal in such a small deflection. The 4.85 mm length × 2 mm diameter GRIN lens rod

(GRINTECH GmbH, Jena, Germany) with working distance = 20 mm, beam width = 20 µm, view angle = ±30°, and NA=0.5 is used to help steer and focus the diverging beam radiating out from the scanner. The estimated beam width at focus based on the given focal length of the GRIN lens and our operating wavelength is around 20 microns based on the 0.4 mm the gap space between the waveguide and grin lens design. The actual beam profile measurement is around 20 microns. The deviation is likely due to the larger gap space between grin lens and waveguide created by the inherent limitation on resolution of the 3D printer.

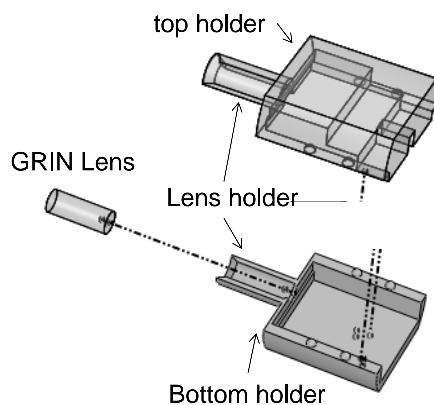

Figure 5.16. A diagram shows both top and bottom holders for the micro-fabricated device.

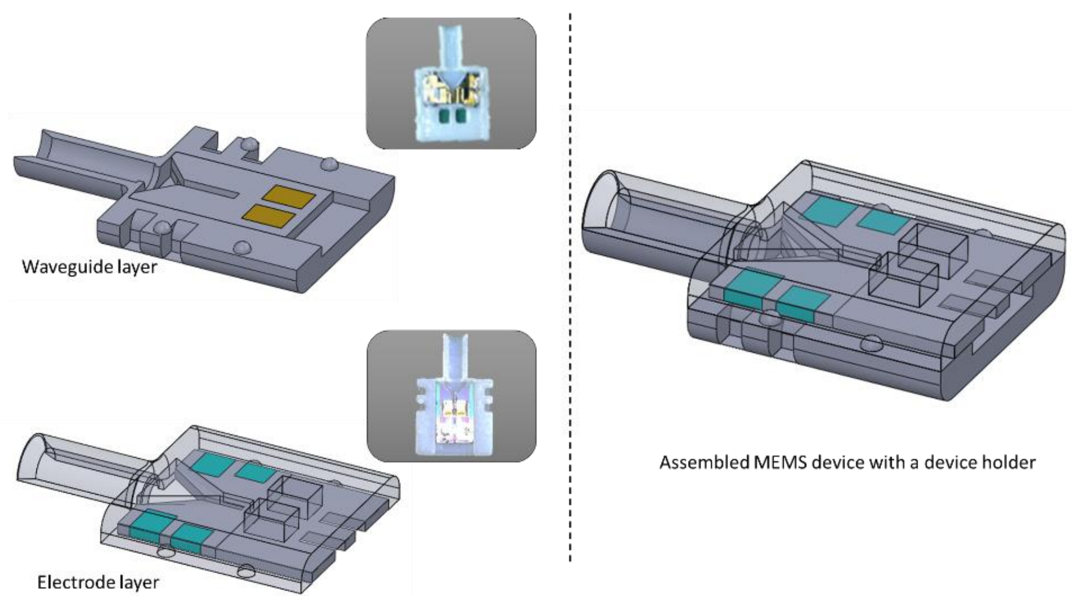

Figure 5.17. Schematics of assembles MEMS device including top electrode, scanner, bottom electrodes, and GRIN lens with the device holder.

5.3 MEMS Device Testing

5.3.1 *Piezoelectric Device Testing*

The mechanical resonance test is performed using a laser vibrometer (Polytec QFC-2600, Germany). Based on the measurement results, we found that the most significant resonances occur at 350 and 1700 Hz in the Z direction (Fig. 5.18). The peak occurring at 1700 Hz is found to be one of the resonant frequencies from the supporting structure. However, the peak at 350 Hz appears to be one of the scanner's resonant frequencies in the Z direction. The deviations are most likely due to fabrication errors. With 10% deviation in the width and/or thickness, resonant frequency can vary up to greater than 10%. This shows the result matches within the predicted 393 Hz Z(I) mode frequency range in the mechanical FEA simulation.

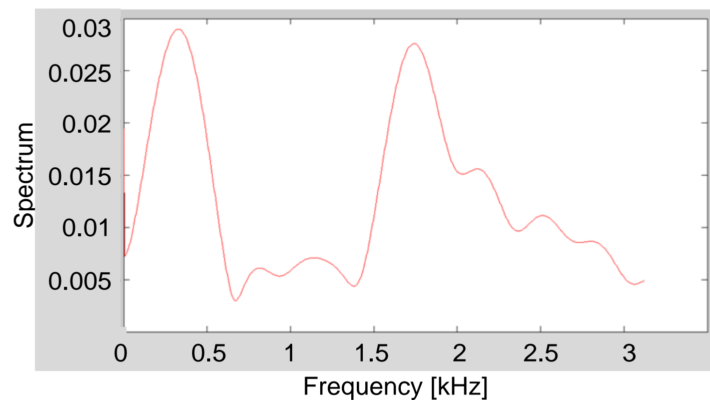

Figure 5.18. Vertical frequency response.

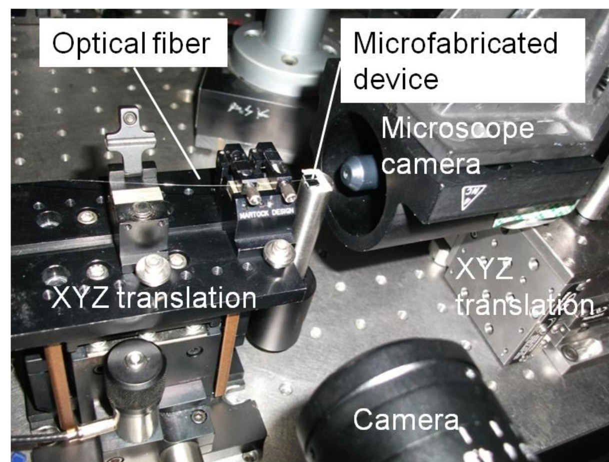

Figure 5.19. Optical test apparatus.

To couple light into the fabricated SU-8 waveguide, an apparatus is constructed as shown in Fig. 5.19. The system uses an XYZ positioning stage for the light-carrying fiber to accurately couple to the SU-8 waveguide. Two cameras equipped with high power lenses (250× magnification) are used to aid the alignment of the optical fiber in both vertical and horizontal directions. A third camera, a microscope, is placed near the tip of the waveguide to observe the light emitted from the waveguide. A 10 mW He-Ne laser (λ=632.8 nm) provides the necessary light to the single mode optical fiber (diameter = 4.3 μm).

After using the microscope and the cameras to align the fiber to the scanner, light is observed at the tip of the waveguide. Fig. 5.20(a) shows the aerial view of the waveguide with light coupled into the waveguide. Visible light can be seen coming out of the tip of the waveguide, some light is also observed near where the light is coupled into the coupler of the waveguide (Fig. 5.20(b)). Light scattering is also observed near the tip of the waveguide due to the curling of the waveguide. Fig. 5.20 (c) shows the diverging beam as it leaves the waveguide without a GRIN lens. The intensity of the light at the output of the waveguide and the light from the input fiber are measured. The average coupling (or transmission) efficiency is calculated to be around 10% (Table 5.2). The low coupling efficiency is mainly due to inherent process imperfections in making the fiber groove using Deep RIE. Although the dimension of our waveguide reaches the limit of our fabrication facility capability, a chemically etched optical fiber is used to reduce the cladding mode and create a smaller tip (5 to 10 μm) to match the rib cross section (Fig. 5.21(a)) [85]. The effect of the tapering process is also evident in Fig. 5.21(b), where it shows that a tapered fiber does produce a finer pixel (4.3 μm after tapering process) than a regular fiber (Fig. 5.21(c)). In the future, a laser with larger input power (>10 mW) and a larger fiber core (10 um for wavelength ~ 1.3 um) will be used. The light with addition of focusing lens and better light coupling at the fiber-waveguide interface. The output is expecting to improve by at least 2 to 3 orders in magnitude.

Table 5.2. Light coupling measurement.

	Intensity measured at fiber end (Volt)	Intensity measured at waveguide output (Volt)
Mean 1	0.077	0.014
Mean 2	0.079	0.004
Mean 3	0.075	0.006
Mean	0.077±0.001	0.008 ±0.001
Coupling efficiency (%)		10.390

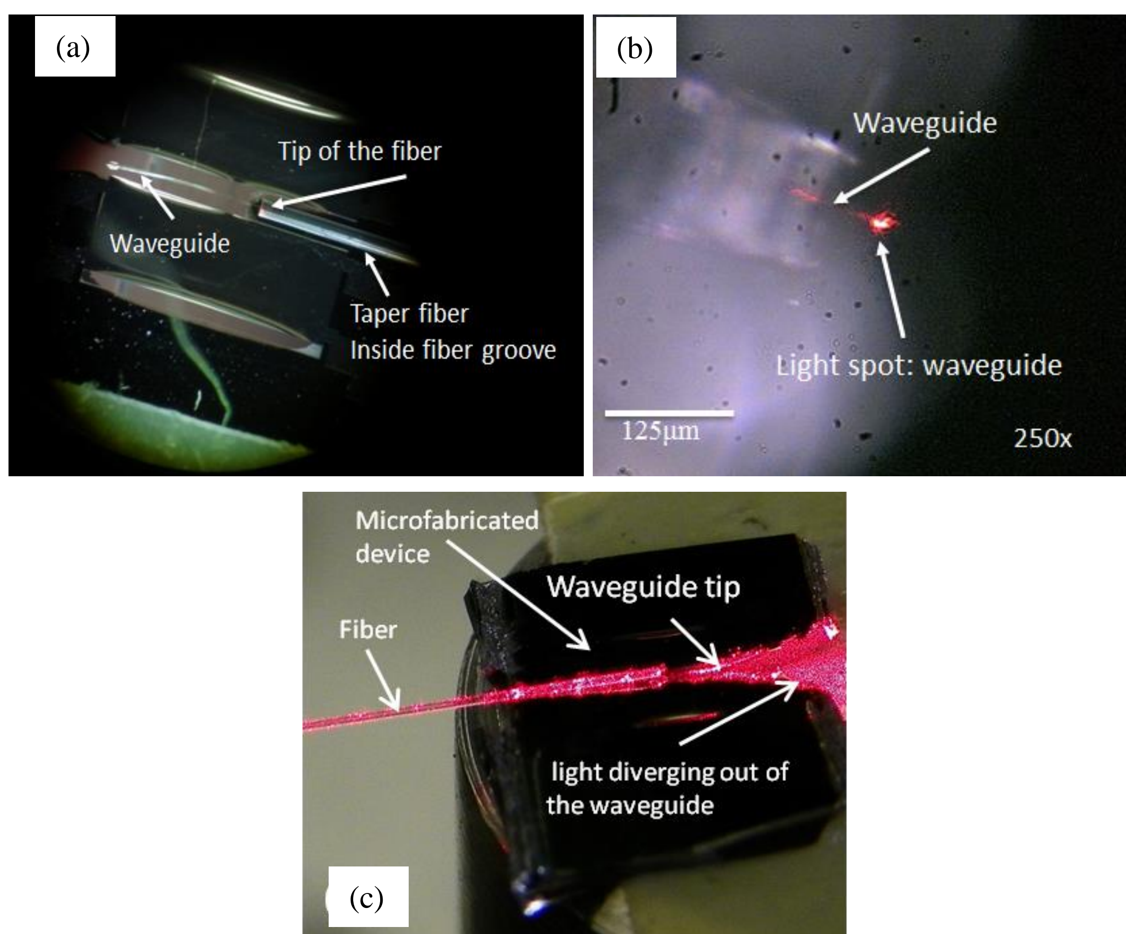

Figure 5.20. Waveguide with coupled light source. (a) Aerial view, and (b), light coming out from the tip of cantilever waveguide, and (c) diverging beam.

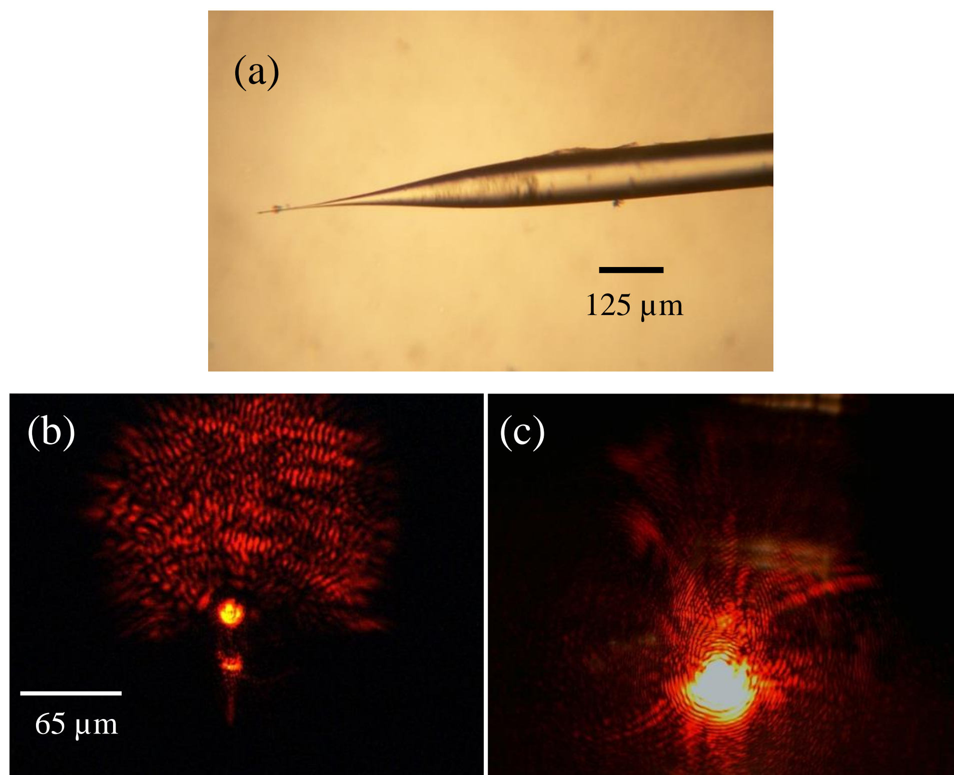

Figure 5.21. Microscope picture of a tapered single mode fiber (cladding diameter of 125 μm) tip resulting from a chemical etching process, and the comparison of (b) Output of a single "pixel" from this tapered fiber tip and (c) original un-tapered fiber tip.

5.3.2 *Electrostatic Device Testing*

Experiments Setup

The electrostatic scanner test sample is prepared as shown in Fig. 5.22. Fig. 5.22 (a) shows the MEMS device test sample including both top and bottom electrodes and the holder with expended pads made of copper tapes sitting on a glass slide. The extended copper electrodes and the MEMS device are connected by soldering with Litz wires (for the details of preparing the test sample, please see Appendix C). An apparatus for the electrostatic device on the glass slide is constructed as shown in Fig. 5.22 (b) to couple light into the fabricated SU-8 waveguide. The system uses an XYZ positioning stage for the light-carrying fiber to accurately couple to the SU-8 waveguide. The scanner is placed into the waveguide layer holder as the bottom layer, an optical fiber is

inserted into the glove of the waveguide layer as a light source. Instead of inserting the fiber horizontally, an angle about 30 degree making the light can be better coupled into the waveguide. The tilting degree of the fiber holder can be adjusted by turning the side knobs to approach the best coupling between the optical fiber and the waveguide (Fig. 5.22 (c)). In order to observe the scanning motion of the waveguide tip, two cameras equipped with high power lenses (250× magnification) are set to provide aerial view and front view images of the SU-8 waveguide tip (Fig. 5.19 (d)). Again a 10 mW He-Ne laser (λ=632.8 nm) provides the necessary light to the single mode optical fiber (diameter = 4.3 μm). Fig. 5.23 shows the aerial view of the waveguide with light coupled into the waveguide.

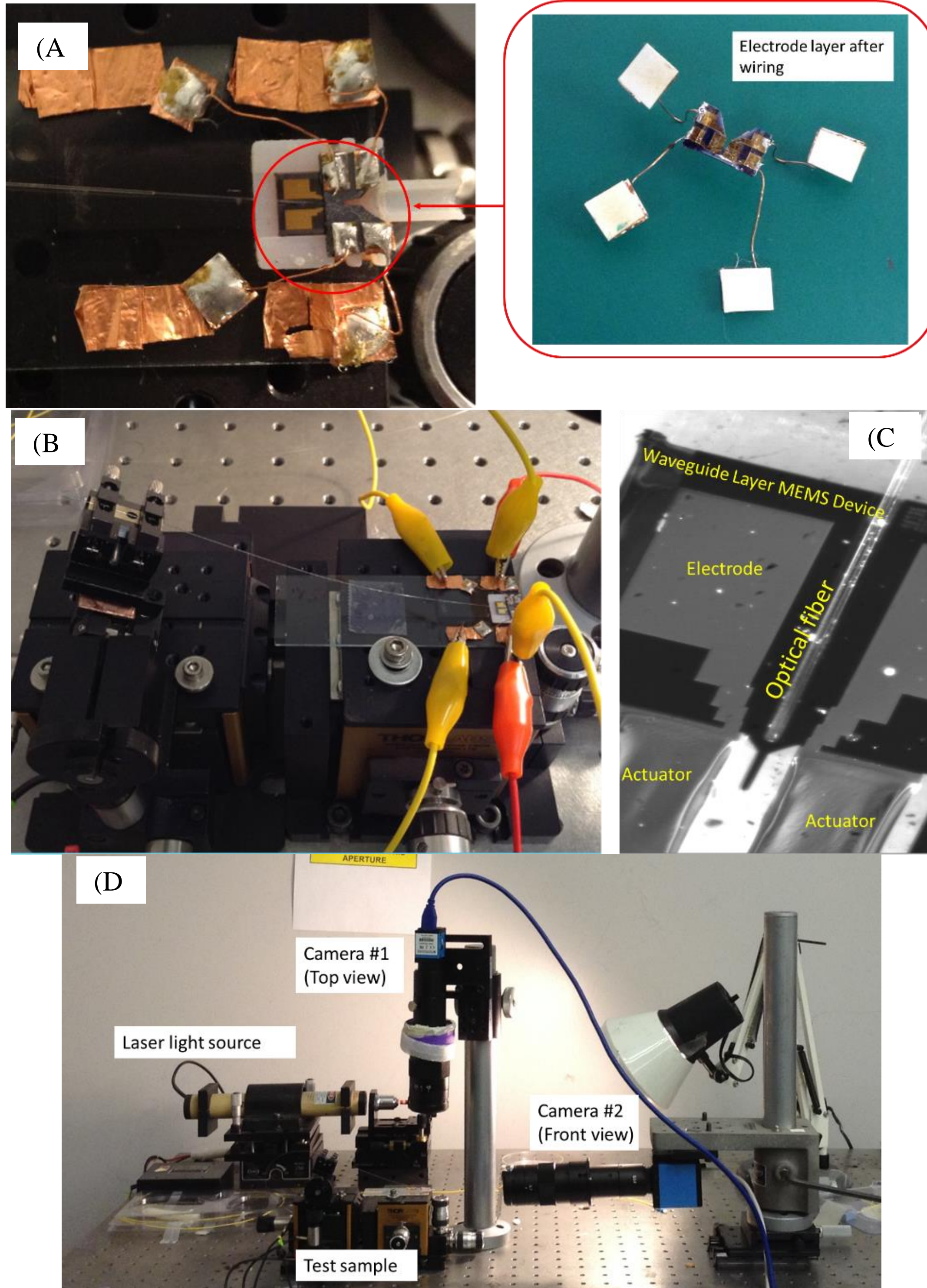

Figure 5.22. (a) the MEMS device test sample (b) apparatus for the electrostatic scanner with (c), a single mode fiber inserted in the fiber groove with an angle for the best coupling. (d) two cameras equipped with high power lenses (250× magnification) are set to provide aerial view and front view images.

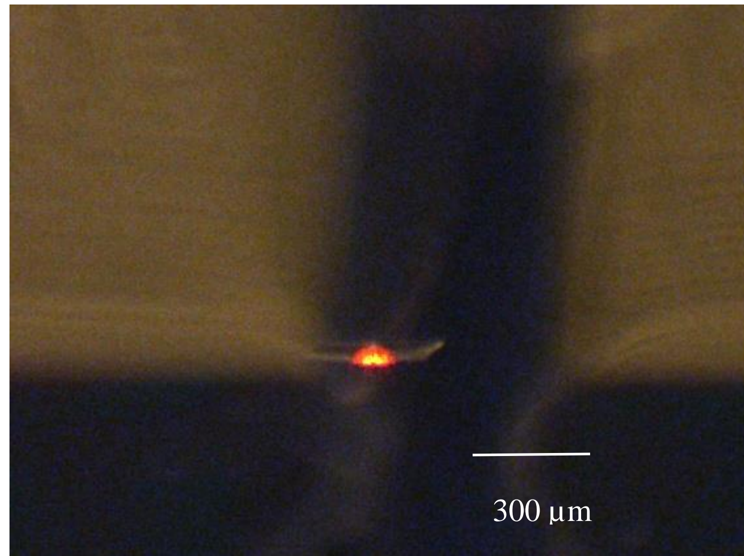

Figure 5.23. Aerial view of the waveguide with light coupled into the waveguide.

Several aspects of the performance of the device are tested. The vertical scan is achieved by applying 100 V DC voltage to the bottom electrodes and ±150 V AC voltage to both of the top electrodes (left and right) with the same phase. The horizontal scan can also be observed by driving actuators with the same voltage as vertical scan but with 180 degree phase delay to top electrodes. The applied driving voltages are much larger than expected due to the fact that the gap space between top and bottom electrodes is larger than original designed value (20 µm). The resonant frequencies for both directions are found by sweeping the frequency from 10 Hz to 600 Hz (Fig. 5.24). The resonant frequencies are found to be ~201 Hz in the vertical direction, which is three times higher than the simulation result (56 Hz), and ~535 Hz in the horizontal scan, about half of the simulation result (1062 Hz). As expected, the waveguide tip displacement in the horizontal direction is relatively small compared to the vertical direction (19 µm and 130 µm respectively, which is about 0.009 and 0.062 rad as the field of view). Again the variations are most likely due to the fabrication imperfection, including the thickness variation of the SU-8 waveguides, and the plasma damage during the backside etch step. Fig. 5.25 presents the images of the characterization of the actuator membrane performance with static actuation versus applied DC voltages. The actuator membrane deflection is achieved by grounding bottom electrodes and applying voltage to the top electrodes. Visible deformation of the actuator membrane starts from the voltage 200V.

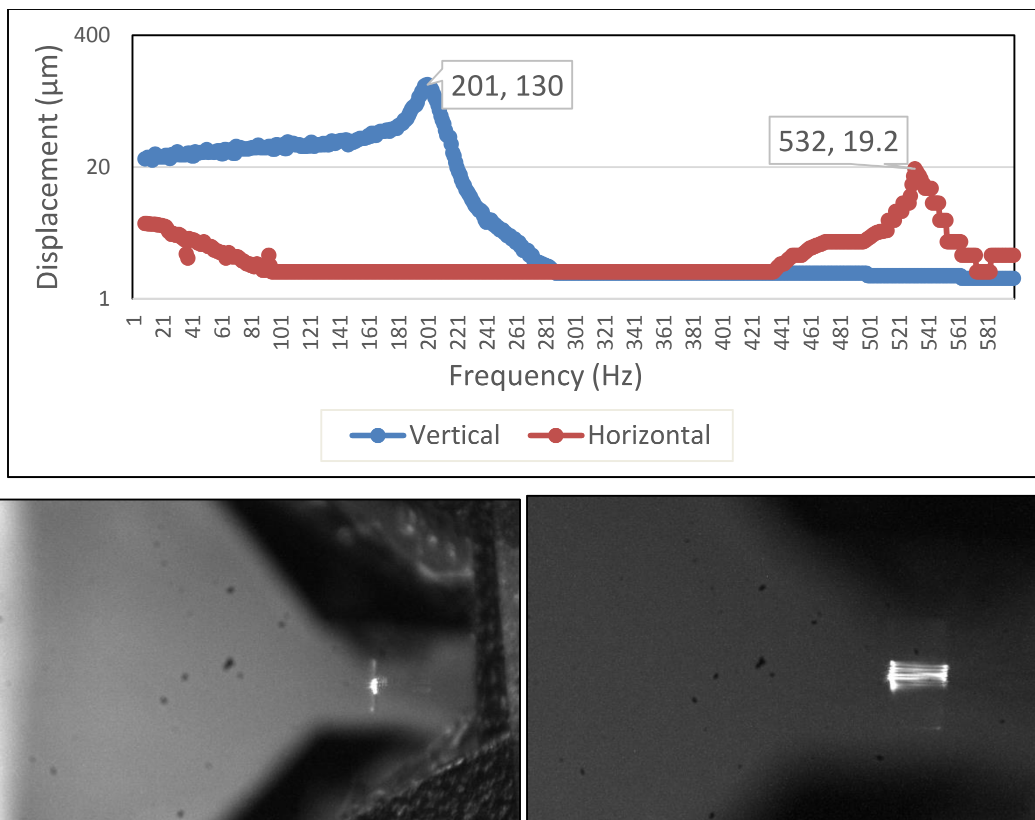

Figure 5.24. (a) Waveguide tip displacement vs. resonant frequency under the driving voltages with 100V DC to bottom electrodes and 150V AC to top electrodes. Microscope pictures show driving frequency under (b) 0 Hz, (c) 201 Hz.

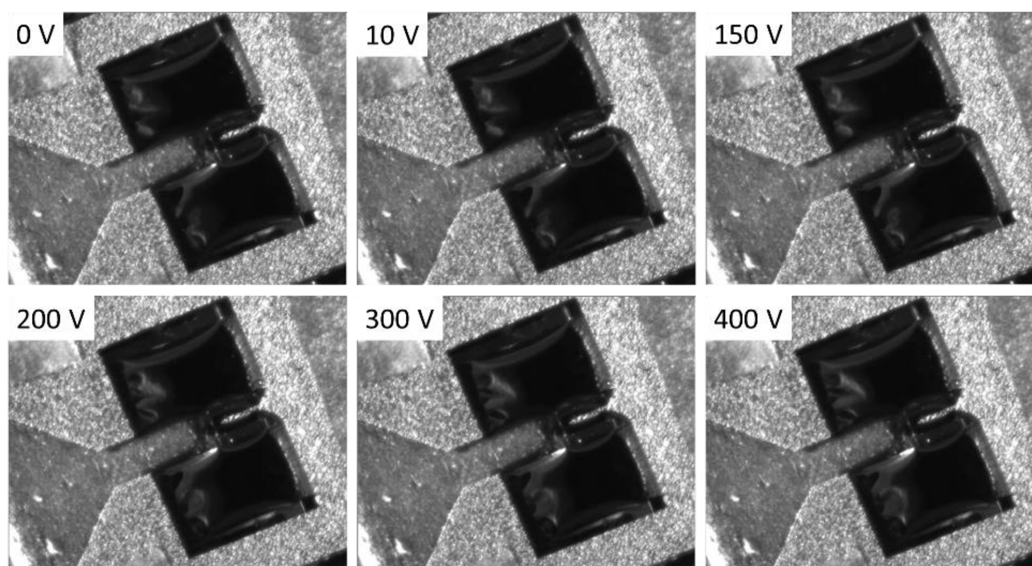

Figure 5.25. Statistic actuator deformation under various input DC voltage.

Characterization of the scanning performance of the waveguide is performed by measuring the waveguide tip displacement and scanning angle versus input actuation voltages. The scanning angle is calculated as the inverse of the sine function of the half of the tip displacement over the waveguide length, in this case, 2100 μm. Due to the large electric field necessary to actuate the actuators, an amplifier (30×) that is capable of generating high voltages must be used (Fig. 5.26). As expected, the AC voltage needed to actuate the waveguide is much greater than the simulation results due to the fact that the displacement between fabricated top and bottom electrodes can't be precisely controlled and is expected to be much larger than the original design. Fig. 5.27 shows the measurement results in vertical direction. Both tip displacement and scanning angle versus actuation voltages are highly linear. The largest test voltage is 150 V, with a tip displacement of 111.8 μm and a corresponding 3.21 degree of the field of view under 1 Hz driving frequency.

Measurement of displacement of the waveguide tip in vertical direction under various driving frequencies is shown in Fig. 5.27. The driving frequency is adjusted from 1 Hz to 15 Hz, with 120 AC voltage. As can be seen in Fig. 5.27, the tip deflection shows no significant trends during the first 15 Hz, which basically meets our expectations since the first resonant frequency of the micro-fabricated waveguide in vertical direction is measured to be around 202 Hz and there is no trend of the displacement change before the first resonant frequency.

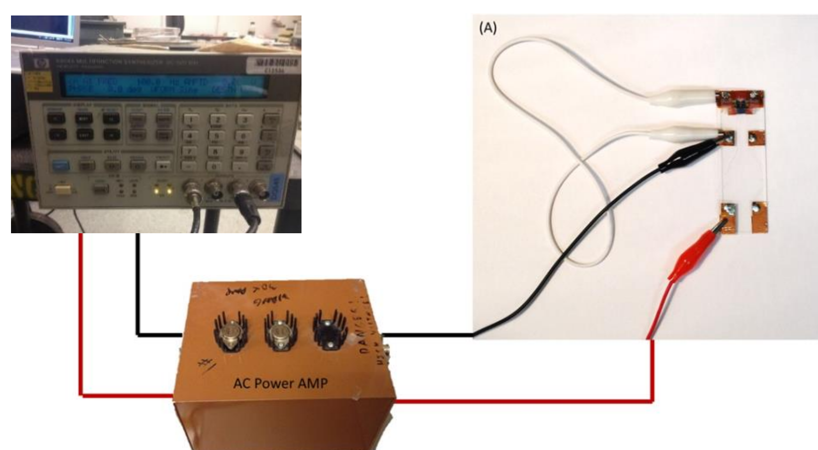

Figure 5.26. A 30× AC amplifier connected with the function generator (HP 8904A, USA) is used to generate high voltage for MEMS device testing.

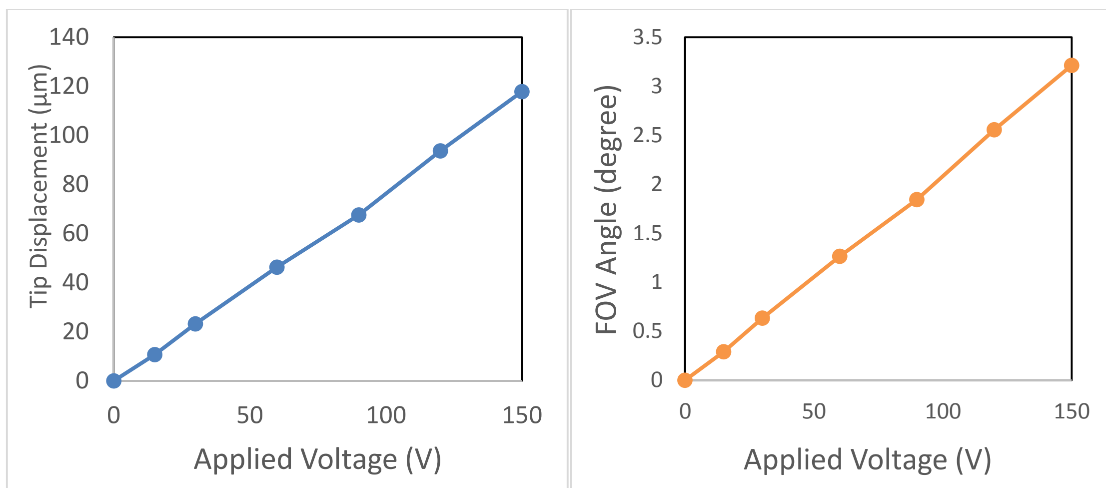

Figure 5.27. (a) Waveguide tip displacement and (b) scanning angle versus varies applied voltage under 1 Hz driving frequency.

A horizontal displacement can also be observed by driving left and right actuators with 180 degree phase delay. Fig. 5.28 shows both vertical and horizontal movement achieved by applying 50 V DC voltage to the bottom electrodes and ±50 V AC voltage to the top electrodes with the same phase (Fig. 5.28 (a)) and with 180 degree phase difference between both left and right pads (Fig. 5.28 (b)) when 2 Hz driving frequency. As expected, the displacement in the horizontal direction is relatively small compared to the vertical direction (13 µm and 33 µm respectively, which is about 0.35 degree as the field of view in horizontal direction), and can only be observed when the driving frequency is very small (under 5 Hz). This low frequency is far below the known resonant frequency (535 Hz) so that the desired resonant vibration cannot be achieved.

The initial displacement measurement of the scanner is much smaller than expected due to smaller than expected actuation from the actuator. The probable cause of the smaller than expected actuation is likely due to the residual silicon thickness that is not completely removed during the release of the actuators (Fig. 5.29). This additional silicon layer most likely increases the stiffness and thus reduces the actuation.

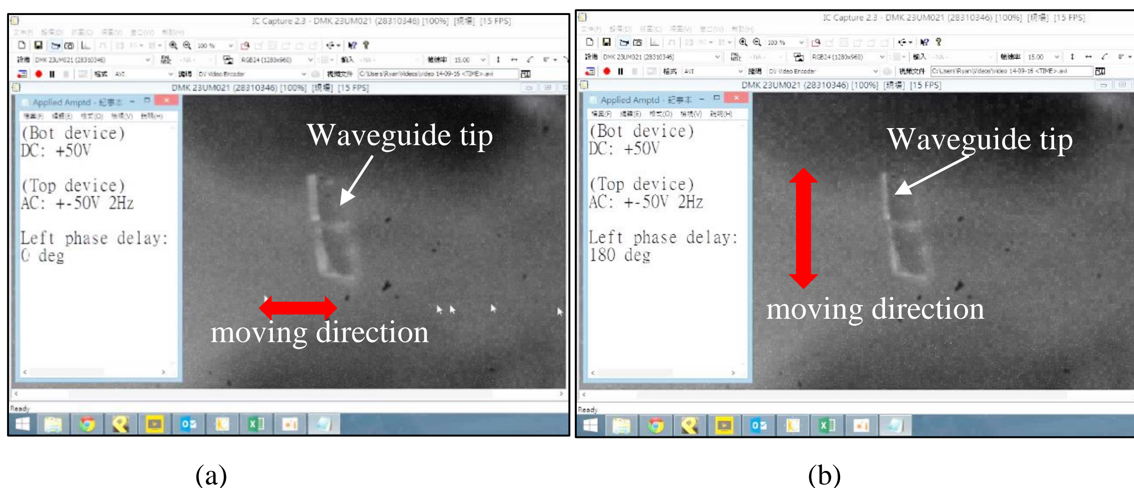

(a) (b)

Figure 5.28. Vertical and horizontal displacement can be achieved by applying 50 V DC to the bottom electrodes and 50 V AC to the top electrodes with (a) same phase, and (b), with 180 degree phase difference to the left and right electrodes.

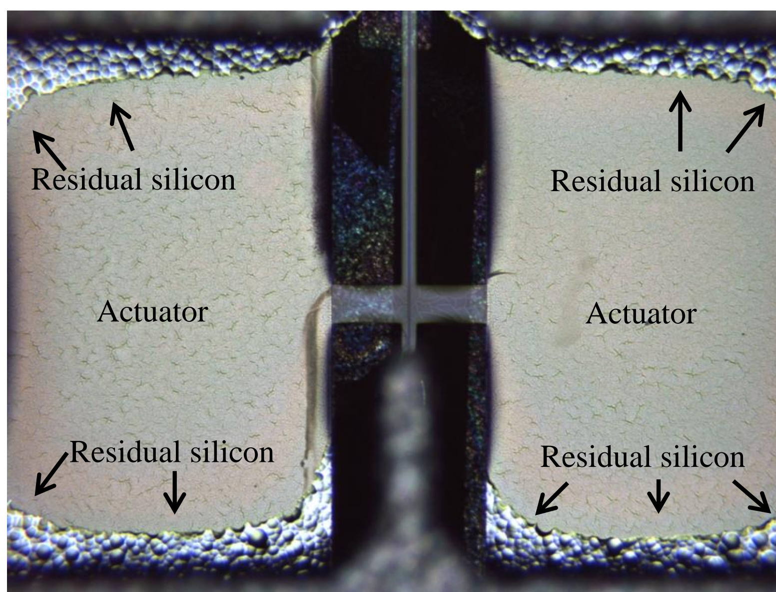

Figure 5.29. Microscopic picture shows residual silicon around corner of actuators after deep RIE released. Picture taken from the backside and focus on the surface of the actuators.

Chapter 6. CONCLUSIONS

New push-pull devices based on micro-fabrication technique to further reduce the size of a resonance-based optical scanner have been designed, fabricated and tested. This new scanning probe is constructed with a SU-8 epoxy-based waveguide actuated by a push-pull actuator, and is the first proposed MEMS scanner which integrates sol-gel thin PZT and electrostatic actuators into a resonance-based waveguide scanner. The scanner's geometric parameters were analyzed to optimize the system's line resolution and FOV. Based on the simulation, the cross-section and length of the waveguide are found to be the dominant factors affecting scanner resolution. Also, higher resolutions can be achieved with a vertically thin or horizontally wide inverted T cross section and a longer waveguide.

From the mechanical resonance test, this research has discovered the vertical resonant of 536 Hz and horizontal resonant of 201 Hz. Deviations to the simulation results are most likely contributed to fabrication errors. With 10% deviation in the width and/or thickness, resonant frequency can vary up to greater than 10%. The initial coupling tests show a relatively low coupling efficiency of 10%. Based on optical simulation, this double-layer SU-8 rib waveguide design has a relatively large cross section (4 μm in height and 60 μm in width) which should provide very good coupling efficiency (~95% with a Gaussian beam profile input) and a broad band single mode operation (λ= 0.7 to 1.3μm) with a minimal transmission loss (85% output transmission efficiency). The discrepancy is likely due to the inherent process imperfection and tooling in creating the device and compounded by the micron range precision alignment needed to couple light from the fiber into the waveguide. For the FOV and line resolution test, the largest FOV is found to be 0.009 rad in horizontal and 0.062 rad in vertical directions and the largest line resolution is calculated to be about 90 dots per line.

The performance of the fabricated device will be tested under a range of temperatures and humidity using a controlled environmental chamber. We will also test the ability of the packaging to withstand an environment similar to clinical use. For the integration with an endoscope and optical system testing using OCT, confocal reflectance, and confocal fluorescence imaging of tissue microanatomy in real time will need to be performed to validate the performance of the waveguide cantilever scanner. Imaging resolution, scanning pattern stability and signal collection efficiency will be characterized using standard resolution chart and tissue phantoms (fluorescent

or non-fluorescent). The current OCT system is based on a Michelson-type interferometer. A superluminescent laser diode with a 1.29-μm center wavelength is employed. In time-domain OCT, a fiber coupler splits the input light between two output optical fibers. The fabricated MEMS device in this study will be used at the distal end of the sample arm focuses the laser beam onto the sample and scans the beam over the desired image to acquire transverse images. The interference signal is generated when the lengths of both reference and signal arms are matched. This allows the imaging depth into the sample to be controlled by dynamically controlling the path length in the reference arm.

Overall, the scanner has integrated electrostatic actuators into a resonance-based waveguide scanner. However, there are some sub-optimal features of the fabricated MEMS devices which need to be addressed in future work. Most of them were discussed in Chapter 5. More revisions in the actuator and coupling system are needed to achieve a better FOV and line resolution.

BIBLIOGRAPHY

1. Miyajima, H., et al., *A MEMS electromagnetic optical scanner for a commercial confocal laser scanning microscope.* Microelectromechanical Systems, Journal of, 2003. **12**(3): p. 243-251.

2. Murakami, K., et al. *A miniature confocal optical microscope with MEMS gimbal scanner*. in *TRANSDUCERS, Solid-State Sensors, Actuators and Microsystems, 12th International Conference on, 2003*. 2003. IEEE.

3. Ra, H., et al., *Two-dimensional MEMS scanner for dual-axes confocal microscopy.* Microelectromechanical Systems, Journal of, 2007. **16**(4): p. 969-976.

4. Shin, H.-J., et al., *Fiber-optic confocal microscope using a MEMS scanner and miniature objective lens.* Optics express, 2007. **15**(15): p. 9113-9122.

5. Amm, D. and R. Corrigan. *5.2: Grating light valve™ technology: update and novel applications*. in *SID Symposium Digest of Technical Papers*. 1998. Wiley Online Library.

6. Francis, D., et al., *Compact 2D laser beam scanner with fan laser array and Si micromachined microscanner.* Electronics Letters, 1997. **33**(13): p. 1143-1145.

7. Hwang, Y., et al. *Large-scale full color laser projection display*. in *Proceedings of the 18th International Display Research Conference ASIA Display*. 1998.

8. Solgaard, O., F. Sandejas, and D. Bloom, *Deformable grating optical modulator.* Optics letters, 1992. **17**(9): p. 688-690.

9. Yamada, K. and T. Kuriyama. *A novel asymmetric silicon micro-mirror for optical beam scanning display*. in *Micro Electro Mechanical Systems, 1998. MEMS 98. Proceedings., The Eleventh Annual International Workshop on*. 1998. IEEE.

10. Davis, W.O., R. Sprague, and J. Miller. *MEMS-based pico projector display*. in *Optical MEMs and Nanophotonics, 2008 IEEE/LEOS Internationall Conference on*. 2008. IEEE.

11. Helmchen, F., et al., *A miniature head-mounted two-photon microscope: high-resolution brain imaging in freely moving animals.* Neuron, 2001. **31**(6): p. 903-912.

12. Muller, R.S. and K.Y. Lau, *Surface-micromachined microoptical elements and systems.* Proceedings of the IEEE, 1998. **86**(8): p. 1705-1720.

13. Urey, H., D.W. Wine, and T.D. Osborn. *Optical performance requirements for MEMS-scanner-based microdisplays*. in *Micromachining and Microfabrication*. 2000. International Society for Optics and Photonics.

14. Wine, D.W., et al. *Performance of a biaxial MEMS-based scanner for microdisplay applications*. in *Micromachining and Microfabrication*. 2000. International Society for Optics and Photonics.

15. Bouma, B. and G. Tearney, *Power-efficient nonreciprocal interferometer and linear-scanning fiber-optic catheter for optical coherence tomography.* Optics Letters, 1999. **24**(8): p. 531-533.

16. Tearney, G., et al., *Scanning single-mode fiber optic catheter-endoscope for optical coherence tomography: erratum.* Optics Letters, 1996. **21**(12): p. 912.

17. Lee, C.M., et al., *Scanning fiber endoscopy with highly flexible, 1 mm catheterscopes for wide-field, full-color imaging.* Journal of biophotonics, 2010. **3**(5-6): p. 385-407.

18. Seibel, E.J., et al., *Scanning single fiber endoscopy: a new platform technology for integrated laser imaging, diagnosis, and future therapies.* Gastrointestinal endoscopy clinics of North America, 2008. **18**(3): p. 467-478.

19. Seibel, E.J., R.S. Johnston, and C.D. Melville. *A full-color scanning fiber endoscope*. in *Biomedical Optics 2006*. 2006. International Society for Optics and Photonics.

20. Seibel, E.J. and Q.Y. Smithwick, *Unique features of optical scanning, single fiber endoscopy***.* Lasers in surgery and medicine, 2002. **30**(3): p. 177-183.

21. Seibel, E.J., et al. *Single-fiber flexible endoscope: general design for small size, high resolution, and wide field of view*. in *EOS/SPIE European Biomedical Optics Week*. 2001. International Society for Optics and Photonics.

22. Takahashi, C., et al. *Polymeric waveguide design of a 2D display system*. in *Nondestructive Evaulation for Health Monitoring and Diagnostics*. 2006. International Society for Optics and Photonics.

23. Wang, W.-C., et al., *Micromachined optical waveguide cantilever as a resonant optical scanner.* Sensors and Actuators A: Physical, 2002. **102**(1): p. 165-175.

24. Guo, Q., G. Cao, and I. Shen. *Measurements of Piezoelectric Constant D33 of Lead Zirconate Titanate (PZT) Through Use of a Mini Impact Hammer*. in *ASME 2009 International Design Engineering Technical Conferences and Computers and Information in Engineering Conference*. 2009. American Society of Mechanical Engineers.

25. Wei-Chih, W. and P.G. Reinhall, *Scanning polymeric waveguide design of a 2-D display system.* Display Technology, Journal of, 2008. **4**(1): p. 28-38.

26. Shkel, A.M., C. Acar, and C. Painter. *Two types of micromachined vibratory gyroscopes*. in *Sensors, 2005 IEEE*. 2005. IEEE.

27. Soref, R.A., J. Schmidtchen, and K. Petermann, *Large single-mode rib waveguides in GeSi-Si and Si-on-SiO 2.* Quantum Electronics, IEEE Journal of, 1991. **27**(8): p. 1971-1974.

28. Panergo, R., et al., *Resonant polymeric waveguide cantilever integrated for optical scanning.* Journal of Lightwave technology, 2007. **25**(3): p. 850-860.

29. Lorenz, H., et al., *SU-8: a low-cost negative resist for MEMS.* Journal of Micromechanics and Microengineering, 1997. **7**(3): p. 121.

30. Becnel, C., *Ultra Deep SU-8 Manufacturing and Characterization for MEMS Applications*. 2004, Faculty of the Louisiana State University and Agricultural and Mechanical College In partial fulfillment of the Requirements for the degree of Master of Science in Mechanical Engineering in The Department of Mechanical Engineering by Charles Becnel BS, Louisiana State University.

31. Lee, C.-C., et al., *Effect of electrode size and silicon residue on piezoelectric thin-film membrane actuators.* Sensors and Actuators A: Physical, 2008. **147**(1): p. 279-285.

32. Mikolajick, T., et al., *FeRAM technology for high density applications.* Microelectronics Reliability, 2001. **41**(7): p. 947-950.

33. Ramesh, R., S. Aggarwal, and O. Auciello, *Science and technology of ferroelectric films and heterostructures for non-volatile ferroelectric memories.* Materials Science and Engineering: R: Reports, 2001. **32**(6): p. 191-236.

34. Summerfelt, S., et al., *Demonstration of scaled (≥ 0.12 µm 2) Pb (Zr, Ti) O 3 capacitors on W plugs with Al interconnect.* Applied physics letters, 2001. **79**(24): p. 4004-4006.

35. Kueppers, H., et al., *PZT thin films for piezoelectric microactuator applications.* Sensors and Actuators A: Physical, 2002. **97**: p. 680-684.

36. Muralt, P., et al., *Piezoelectric actuation of PZT thin-film diaphragms at static and resonant conditions.* Sensors and Actuators A: Physical, 1996. **53**(1): p. 398-404.

37. Yamashita, K., et al., *Arrayed ultrasonic microsensors with high directivity for in-air use using PZT thin film on silicon diaphragms.* Sensors and Actuators A: Physical, 2002. **97**: p. 302-307.

38. Dubois, M. and P. Muralt, *PZT thin film actuated elastic fin micromotor.* Ultrasonics, Ferroelectrics, and Frequency Control, IEEE Transactions on, 1998. **45**(5): p. 1169-1177.

39. Flynn, A.M., et al., *Piezoelectric micromotors for microrobots.* Microelectromechanical Systems, Journal of, 1992. **1**(1): p. 44-51.

40. Muralt, P., et al., *Fabrication and characterization of PZT thin-film vibrators for micromotors.* Sensors and Actuators A: Physical, 1995. **48**(2): p. 157-165.

41. Luginbuhl, P., et al., *Ultrasonic flexural Lamb-wave actuators based on PZT thin film.* Sensors and Actuators A: Physical, 1998. **64**(1): p. 41-49.

42. Baborowski, J., et al., *Fabrication and characterization of micromachined accelerometers based on PZT thin films.* Ferroelectrics, 1999. **224**(1): p. 283-290.

43. Beeby, S., N. Grabham, and N. White, *Micromachined accelerometer with microprocessor controlled self-test procedure.* Sensor review, 2001. **21**(1): p. 33-38.

44. Beeby, S., N. Grabham, and N. White, *Microprocessor implemented self-validation of thick-film PZT/silicon accelerometer.* Sensors and Actuators A: Physical, 2001. **92**(1): p. 168-174.

45. Beeby, S., J. Ross, and N. White, *Design and fabrication of a micromachined silicon accelerometer with thick-film printed PZT sensors.* Journal of Micromechanics and Microengineering, 2000. **10**(3): p. 322.

46. Crescini, D., et al., *Large bandwidth and thermal compensated piezoelectric thick-film acceleration transducer.* Sensors and Actuators A: Physical, 2001. **87**(3): p. 131-138.

47. Kunz, K., P. Enoksson, and G. Stemme, *Highly sensitive triaxial silicon accelerometer with integrated PZT thin film detectors.* Sensors and Actuators A: Physical, 2001. **92**(1): p. 156-160.

48. Nemirovsky, Y., et al., *Design of novel thin-film piezoelectric accelerometer.* Sensors and Actuators A: Physical, 1996. **56**(3): p. 239-249.

49. Wang, L.-P., *Microelectromechanical systems (MEMS) sensors based on lead zirconate titanate (PZT) films*. 2001.

50. Kuwajima, H. and K. Matsuoka, *Thin-film piezoelectric DSA for HDD.* Magnetics, IEEE Transactions on, 2002. **38**(5): p. 2186-2188.

51. Tagawa, N., K.-I. Kitamura, and A. Mori, *Design and fabrication of MEMS-based active slider using double-layered composite PZT thin film in hard disk drives.* Magnetics, IEEE Transactions on, 2003. **39**(2): p. 926-931.

52. Tagawa, N., et al., *Development of novel PZT thin films for active sliders based on head load/unload on demand systems.* Microsystem technologies, 2002. **8**(2-3): p. 133-138.

53. Xia, J., et al. *A micromachined sensor array using thin film resonators*. in *Frequency Control Symposium, 1995. 49th., Proceedings of the 1995 IEEE International*. 1995. IEEE.

54. Shen, I., et al., *PZT thin-film meso-and micro devices.* Ferroelectrics, 2006. **342**(1): p. 15-34.

55. ZHENG, K.-l., et al., *Study on wet-etching of PZT thin films.* Piezoelectr. Acoust, 2005. **27**: p. 209.

56. Carlier, J., et al., *Integrated microfluidics based on multi-layered SU-8 for mass spectrometry analysis.* Journal of micromechanics and Microengineering, 2004. **14**(4): p. 619.

57. Despont, M., et al. *High-aspect-ratio, ultrathick, negative-tone near-UV photoresist for MEMS applications*. in *Micro Electro Mechanical Systems, 1997. MEMS'97, Proceedings, IEEE., Tenth Annual International Workshop on*. 1997. IEEE.

58. Li, B., M. Liu, and Q. Chen, *Low-stress ultra-thick SU-8 UV photolithography process for MEMS.* Journal of Micro/Nanolithography, MEMS, and MOEMS, 2005. **4**(4): p. 043008-043008-6.

59. Evans, J.W. and L.C. De Jonghe, *Production of Inorganic Materials.* 1992.

60. Limmer, S.J., et al., *Electrophoretic growth of lead zirconate titanate nanorods.* Advanced Materials, 2001. **13**(16): p. 1269.

61. Bruchhaus, R., et al., *PZT thin films grown by multi-target sputtering: analysis of thin film stress.* Integrated Ferroelectrics, 1998. **21**(1-4): p. 461-467.

62. Hata, T., et al., *Proposal of new mixture target for PZT thin films by reactive sputtering.* Vacuum, 1998. **51**(4): p. 665-671.

63. Novotny, I., et al. *Piezoelectric ZnO thin films prepared by cyclic sputtering and etching technology*. in *Microelectronics, 1995. Proceedings., 1995 20th International Conference on*. 1995. IEEE.

64. Sakoda, T., et al., *Recent progress in sputtering PZT thin films for ferroelectric memories.* Integrated Ferroelectrics, 1998. **21**(1-4): p. 385-396.

65. Eda, K., et al. *Novel composite piezoelectric materials using direct bonding techniques*. in *Ultrasonics Symposium, 1995. Proceedings., 1995 IEEE*. 1995. IEEE.

66. Eda, K., et al. *Direct bonding of piezoelectric materials onto Si*. in *Applications of Ferroelectrics, 1996. ISAF'96., Proceedings of the Tenth IEEE International Symposium on*. 1996. IEEE.

67. Maas, R., et al., *Thick-film printing of PZT onto silicon.* Materials Letters, 1997. **31**(1): p. 109-112.

68. Pan, C.-Y., Y.-L. Chen, and D.-S. Tsai, *Synthesis and properties of lead zirconate titanate thin films via metalorganic chemical vapor deposition.* Journal of materials research, 2002. **17**(06): p. 1536-1542.

69. Brooks, K., et al., *Processing sol–gel PZT thin films for microactuators.* Electroceramics, Verlag der Augustinus Buchhandlung, Aachen, Germany, 1994. **2**.

70. Cakare, L., B. Malic, and M. Kosec. *Characterization of thick PZT 53/47 films prepared by sol–gel processing*. in *Proceedings of 34th International Conference on Microelectronics, Devices and Materials*. 1998.

71. Miyazawa, K.i., K. Ito, and R. Maeda, *Structure and electrical properties of multilayer PZT films prepared by sol–gel processing.* Ceramics international, 2000. **26**(5): p. 501-506.

72. Sayer, M., G. Yi, and M. Sedlar, *Comparative sol gel processing of PZT thin films.* Integrated Ferroelectrics, 1995. **7**(1-4): p. 247-258.

73. Kobayashi, T., J. Tsaur, and R. Maeda, *Fabrication of optical micro scanner driven by PZT actuators.* Japanese journal of applied physics, 2005. **44**(9S): p. 7078.

74. Donnelly, V.M. and A. Kornblit, *Plasma etching: Yesterday, today, and tomorrow.* Journal of Vacuum Science & Technology A, 2013. **31**(5): p. 050825.

75. Franssila, S., *Introduction to microfabrication*. 2010: John Wiley & Sons.

76. Lärmer, F. and A. Schilp, *Patents DE 4241045*. 1996, US.

77. Choi, C.-H. and C.-J. Kim, *Fabrication of a dense array of tall nanostructures over a large sample area with sidewall profile and tip sharpness control.* Nanotechnology, 2006. **17**(21): p. 5326.

78. Lee, C., et al. *Plasma etch challenges with new EUV lithography material introduction for patterning for MOL and BEOL.* in *SPIE Advanced Lithography*. 2015. International Society for Optics and Photonics.

79. Lee, C.G., K.J. Kanarik, and R.A. Gottscho, *The grand challenges of plasma etching: a manufacturing perspective.* Journal of Physics D: Applied Physics, 2014. **47**(27): p. 273001.

80. Chang, C., et al., *Etching submicrometer trenches by using the Bosch process and its application to the fabrication of antireflection structures.* Journal of micromechanics and microengineering, 2005. **15**(3): p. 580.

81. Lee, Y.-I., et al. *Dry release for surface micromachining with HF vapor-phase etching.* Microelectromechanical Systems, Journal of 6.3 (1997): 226-233.

82. Roberts, D.A. and R.R. Syms. *1D and 2D laser line scan generation using a fiber optic resonant scanner*. in *Symposium on Applied Photonics*. 2000. International Society for Optics and Photonics.

83. Cardinale, G., et al., *Micromachined silicon cantilever beams for thin-film stress measurement.* Thin solid films, 1996. **287**(1): p. 214-219.

84. http://www.microchemicals.com/technical_information/exposure_photoresist.pdf

85. Wang, W.-C. and C.-L. Tsui, *Two-dimensional mechanically resonating fiber optic scanning display system.* Optical Engineering, 2010. **49**(9): p. 097401-097401-8.

List of Abbreviations:

Abbreviation	**Description**
℃	Celsius, degrees (unit of temperature)
μm	Micrometer (unit of length)
AC	Alternating Current
ARC	Anti-reflection Coating
ARDE	Aspect Ratio Dependent Etch
Au	Gold
BOE	Buffered Oxide Etch
BPM	Beam Propagation Method
C_4F_8	Octafluorocyclobutane
cm	Centimeters (unit of length)
Cr	Chromium
CTE	Coefficient of thermal expansion
DC	Direct Current
DI	Deionized
DRIE	Deep Reactive Ion Etching
FEA	Finite Element Analysis
FORS	Fiber Optic Resonant Scanner
FOV	Field of View
FRF	Frequency Response Function
GPa	Gigapascal (SI derived unit of pressure)
GRIN	Gradient Index
H_2O_2	Hydrogen peroxide
H_2SO_4	Sulfuric acid
HCl	Hydrogen chloride
He-Ne	Helium–Neon
HF	Hydrogen Fluoride
HMD	Head-mounted Displays
HNO_3	Nitric Acid

Hz	Hertz (unit of frequency)
ICP	Inductively coupled plasma
IPA	Isopropyl alcohol
LPCVD	Low Pressure Chemical Vapor Deposition
MEMS	Micro-Electromechanical System
mJ	Millijoule (derived unit of energy)
mm	Millimeter (unit of length)
MOCVD	Metal organic chemical vapor deposition
n	Refractive index
NA	Numerical Aperature
NH_4OH	Ammonium Hydroxide
nm	Nanometer (unit of length)
O_2	Oxygen
OCT	Optical Coherence Tomography
PAG	Photoacid Generator
Pb	Lead
$PbCl_2$	Lead(II) chloride
PbClF	Lead (II) Chloride Fluoride
PEB	Post Exposure Bake
PGMEA	Propylene Glycol Monomethyl Ether Acetate
Pt	Platinum
PZT	lead-zirconate-titanate
rad	Radian (unit of angular measure)
RIE	Reactive Ion Etching
RPM	Rounds per Minute
SEM	Scanning electron microscope
SF_6	Sulfur Hexafluoride
Si	Silicon
SiO2	Silicon Dioxide
SFE	Scanning Fiber Endoscope

SLD	Superluminescent diode
SMF	Single-Mode Fiber
SRD	Spin Rinse Dryer
SWA	Sidewall Angle
TE	Transverse electric
Ti	Titanium
TM	Transverse Magnetic
UV	Ultraviolet
V	Volts (unit of voltage)
Zr	Zirconium

APPENDIX A: PIEZOELECTRIC SCANNER MICROFABRICATION PROCESS FLOW

0.0 Purpose

The appendix provides detailed fabrication process instructions for PZT push-pull resonant scanner.

1.0 Lists of Photolithography Masks

Number	Layer Name	Process Type	Photoresist Type
1	Front Side Opening	Etch	NR71-1000PY
2	Bottom Electrode	Lift-off	NR71-1000PY
3	Backside Opening	Etch	AZ 1512/AZ P4620
4	Top Electrode	Lift-off	NR71-1000PY
5	PZT Patterning	Wet etch	AZ P4620
6	Fiber Groove	Etch	AZ P4620
7	Sacrificial Layer	Sacrificial Layer	AZ 1512
8	Waveguide Slab	Structure	SU-8
9	Waveguide Ridge	Structure	SU-8

2.0 Front side Opening

2.1 Patterning

2.1.1 Negative photoresist NR71-1000PY (Futurrex Inc.), 2000 rpm, 40s

2.1.2 Thickness: ~1.2 micron

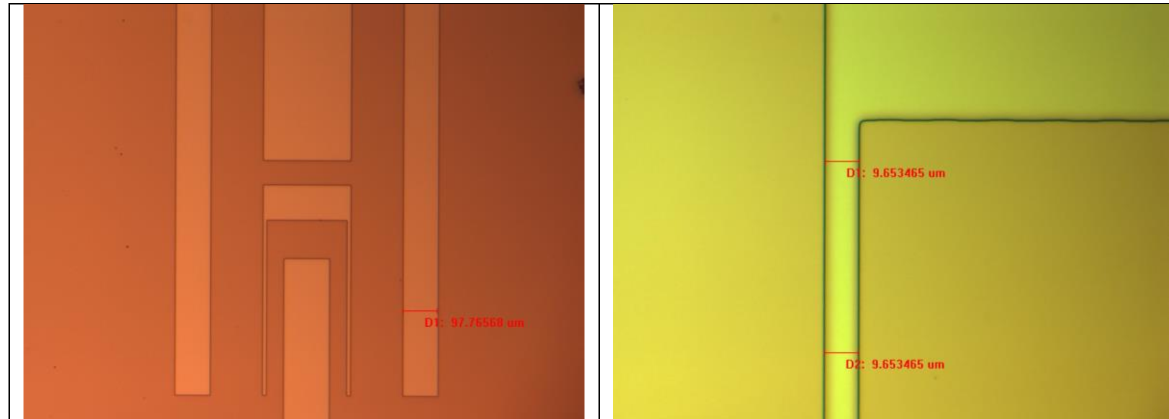

2.2 RIE

Nitride Recipe: 180 sec., Oxide recipe: 600 sec.

Recipe	Nitride	Oxide
Pressure Set (mTorr)	130	70
RF Power (W)	75	75
Base Pressure (mTorr)	50	50
O_2 (sccm)	0	2
CHF_3 (sccm)	0	25
SF_6 (sccm)	15	0

Etch Time (sec.)	180	600
Etch Rate (nm/min.)	118	61 (Thermal Oxide)

Thickness after RIE: ~0.89 micron

3.0 Bottom Electrode Patterning, Deposition, Lift-off and Heat Treatment

3.1 Patterning:

3.1.1 Negative photoresist NR71-1000PY (Futurrex Inc.), 2000 rpm, 40s

3.1.2 Thickness: ~1.2 micron

3.1.3 RIE Descum

Recipe	Descum
Pressure Set (mTorr)	75
RF Power (W)	50
Base Pressure (mTorr)	50
O_2 (sccm)	25
CHF_3 (sccm)	0
SF_6 (sccm)	0
Etch Time (sec.)	30

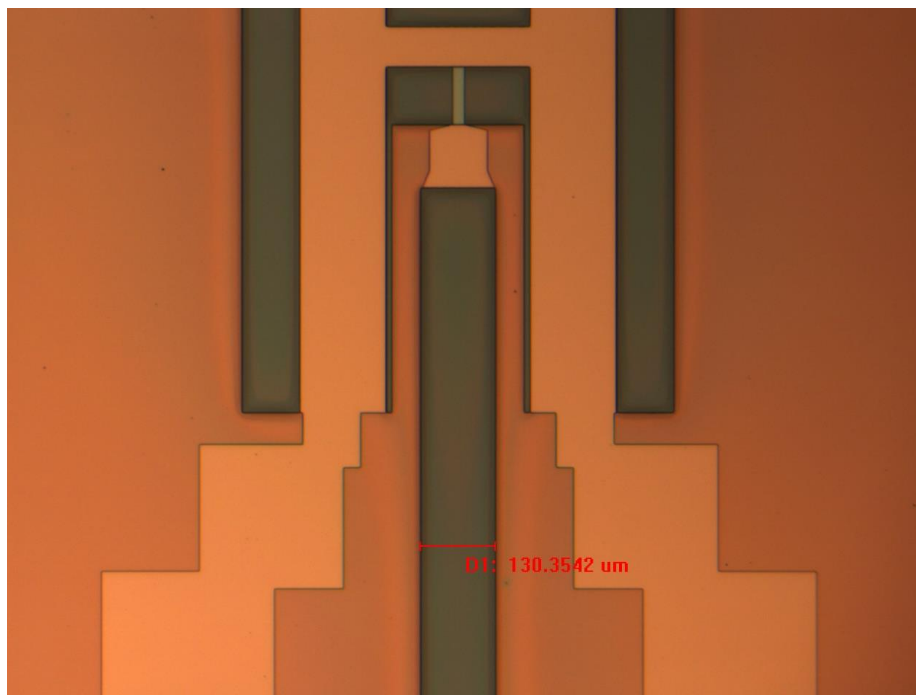

3.2 Deposition:

E-beam evaporator

Material	Titanium	Platinum
Final Thickness (angstrom)	200	1000
Rate (angstrom/sec.)	5	3

3.3 Lift-off:

RR4 resist remover (Futurrex Inc.), 24 hours

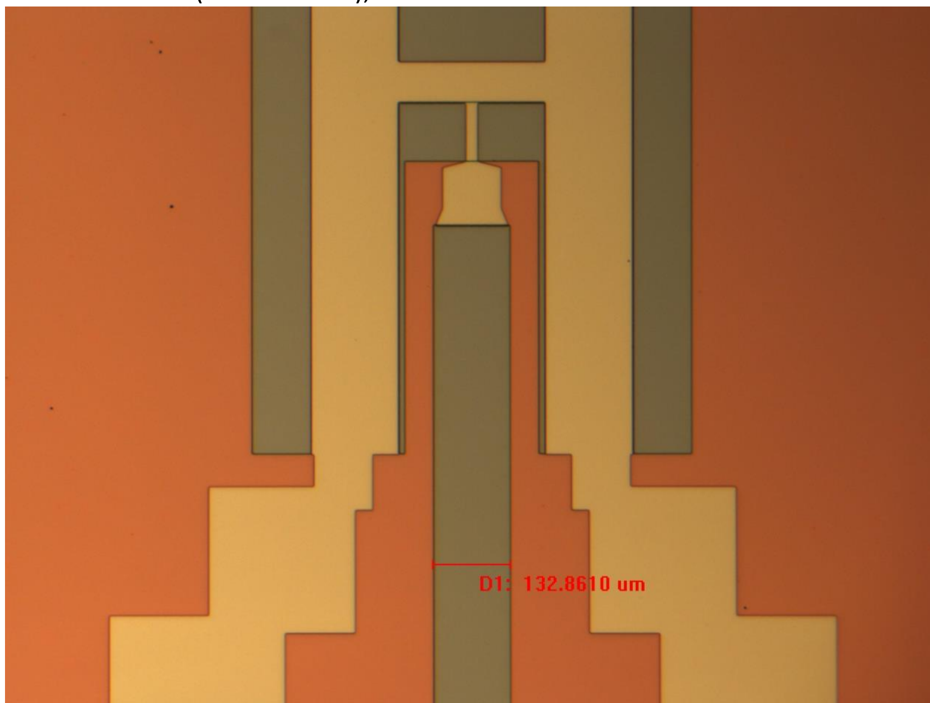

3.4 Heat Treatment:

3.4.1 Place the sample right at the middle of oxidation furnace tube 4. The sample wafer must be placed as flat up, face out.

3.4.2 Choose the recipe “Pt800”, verify the recipe meets the criteria as in the table below, then hits “run”.

Recipe: 800Pt		
	Time	Target
Time to Target	1 min.	20°C
Ramp Rate	10°C/min.	800°C
Dwell	45 min.	xxx
Ramp rate	10°C/min.	20°C

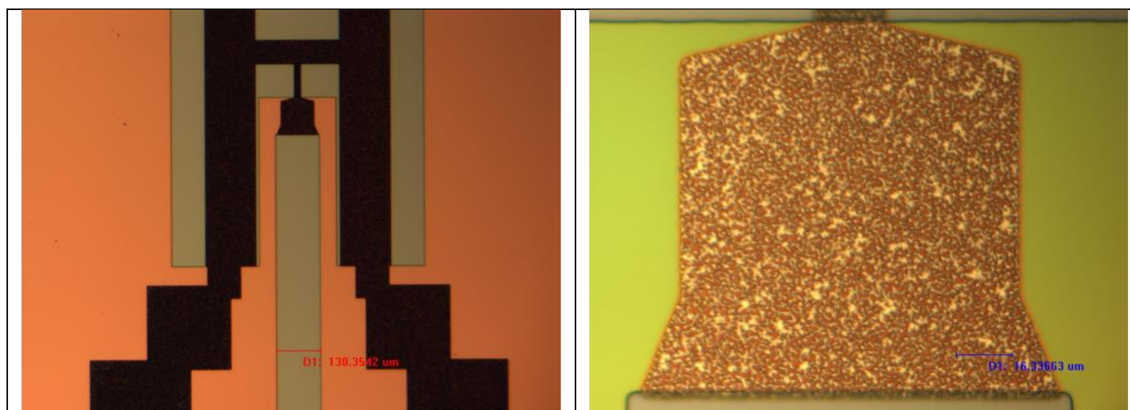

4.0 Backside Opening Patterning and RIE

4.1 Patterning:

Negative Photoresist NR71-1000PY (Futurrex Inc.), 2000 rpm, 40 sec.

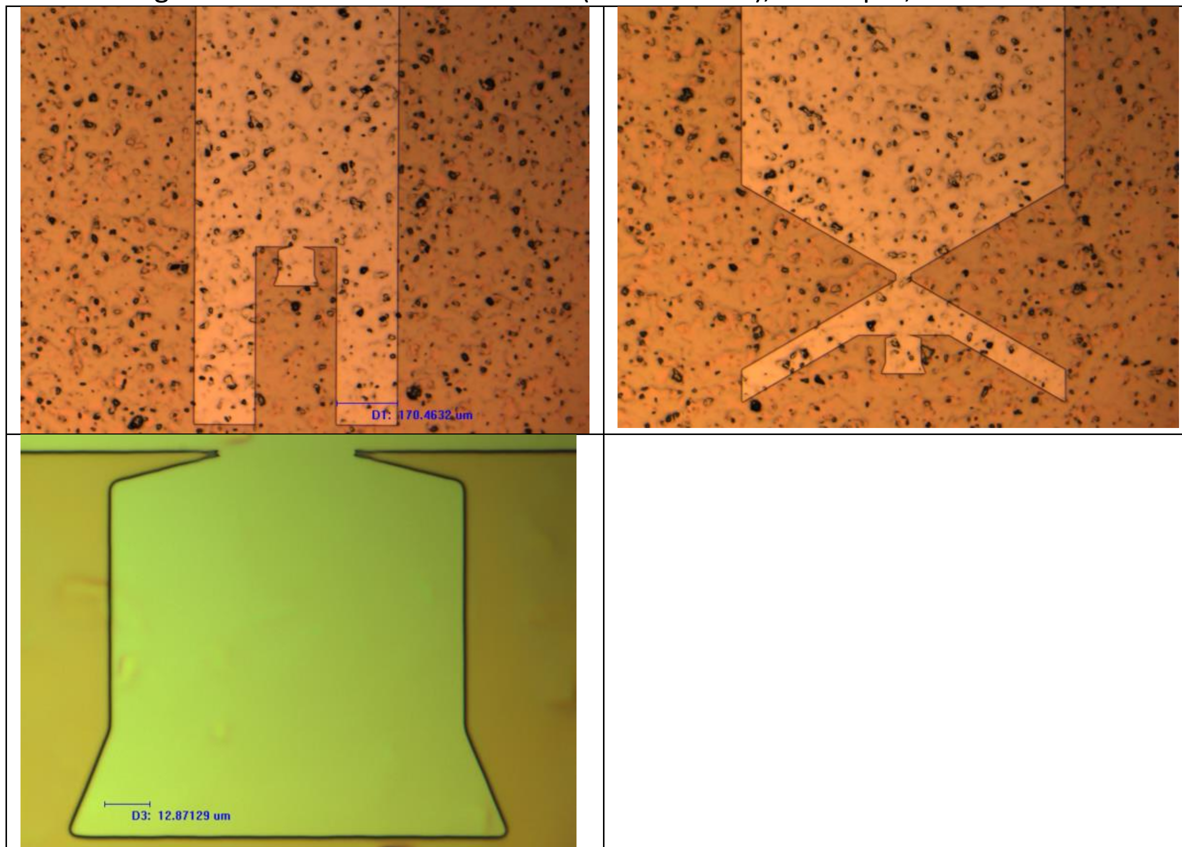

4.2 RIE

Nitride Recipe: 180 sec., Oxide recipe: 600 sec.

Recipe	Nitride	Oxide
Pressure Set (mTorr)	130	70
RF Power (W)	75	75
Base Pressure (mTorr)	50	50
O_2 (sccm)	0	2
CHF_3 (sccm)	0	25
SF_6 (sccm)	15	0
Etch Time (sec.)	180	600
Etch Rate (nm/min.)	118	61 (Thermal Oxide)

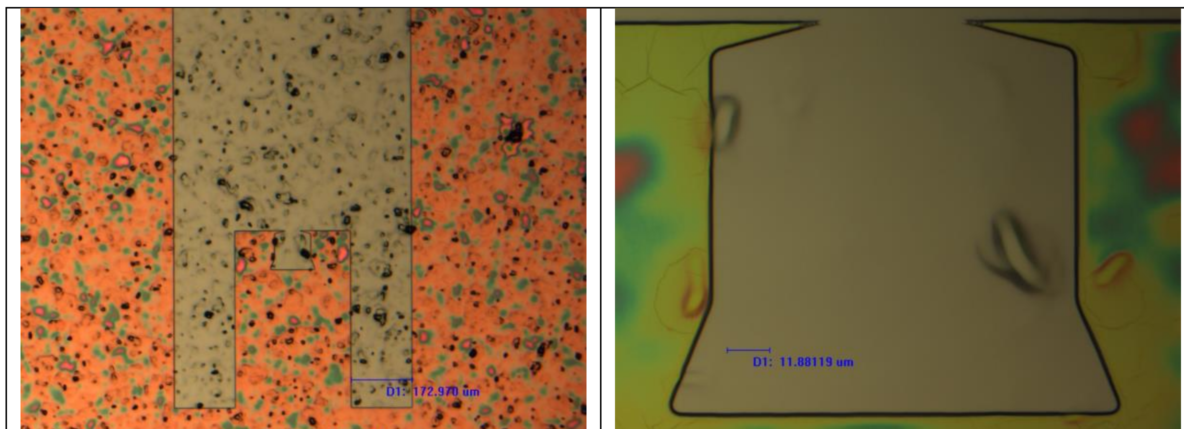

5.0 PZT Coating and Sintering

Steps: Spin coating PZT→ Rest period (15min.) → Furnace tube 4 sintering

Repeat 3X

5.1 Spinner recipe (Headway):

Spin speed (rpm)	Rate (rpm/sec.)	Dwell time (sec.)
500	500	5
4500	1500	20

Thickness:

5.2 Rest Period

Place the sample wafer on the table for 15 minutes.

5.3 PZT Sintering

5.3.1 Choose the recipe "PZT film", verify the recipe meets the criteria as in the table below, hits "run".

Recipe: PZT film		
	Time	Target
Time to Target	1 min.	20℃
Ramp Rate	10℃/min.	650℃
Dwell	100 min.	xxx
Ramp rate	10℃/min.	20℃

Hold the temperature when the temperature reaches 650℃.

5.3.2 Place the sample right at the middle of oxidation furnace tube 4 for 10 minutes. Make sure the temperature in Tube 4 is exact at 650℃.

5.3.3 The sample wafer must place as flat up, face out.

5.4 Repeat

Repeat step 3.1-3.4 two more times, totally 3 layers of PZT thin film.

1st PZT coating

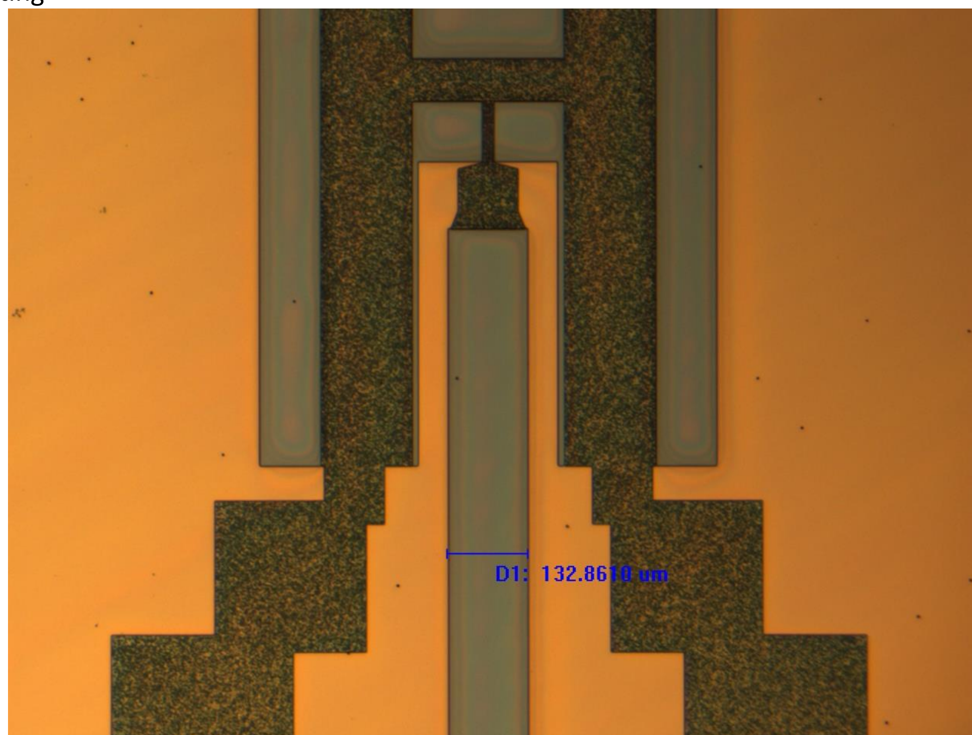

1st Sintering

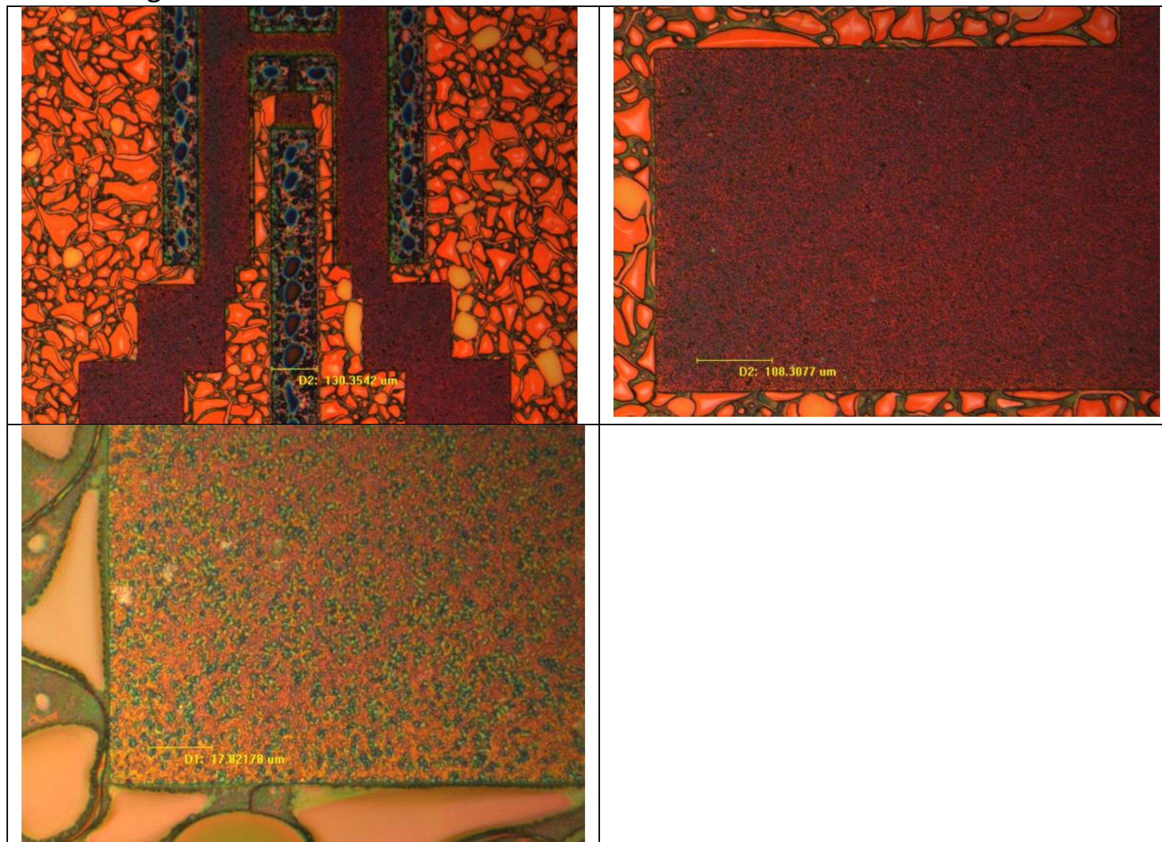

2nd PZT Coating:

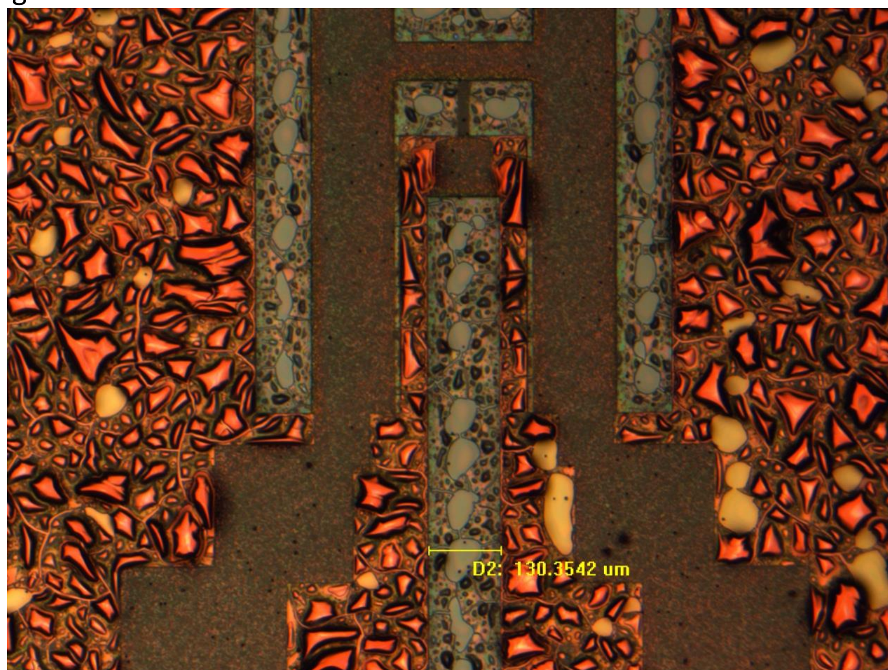

2nd Sintering

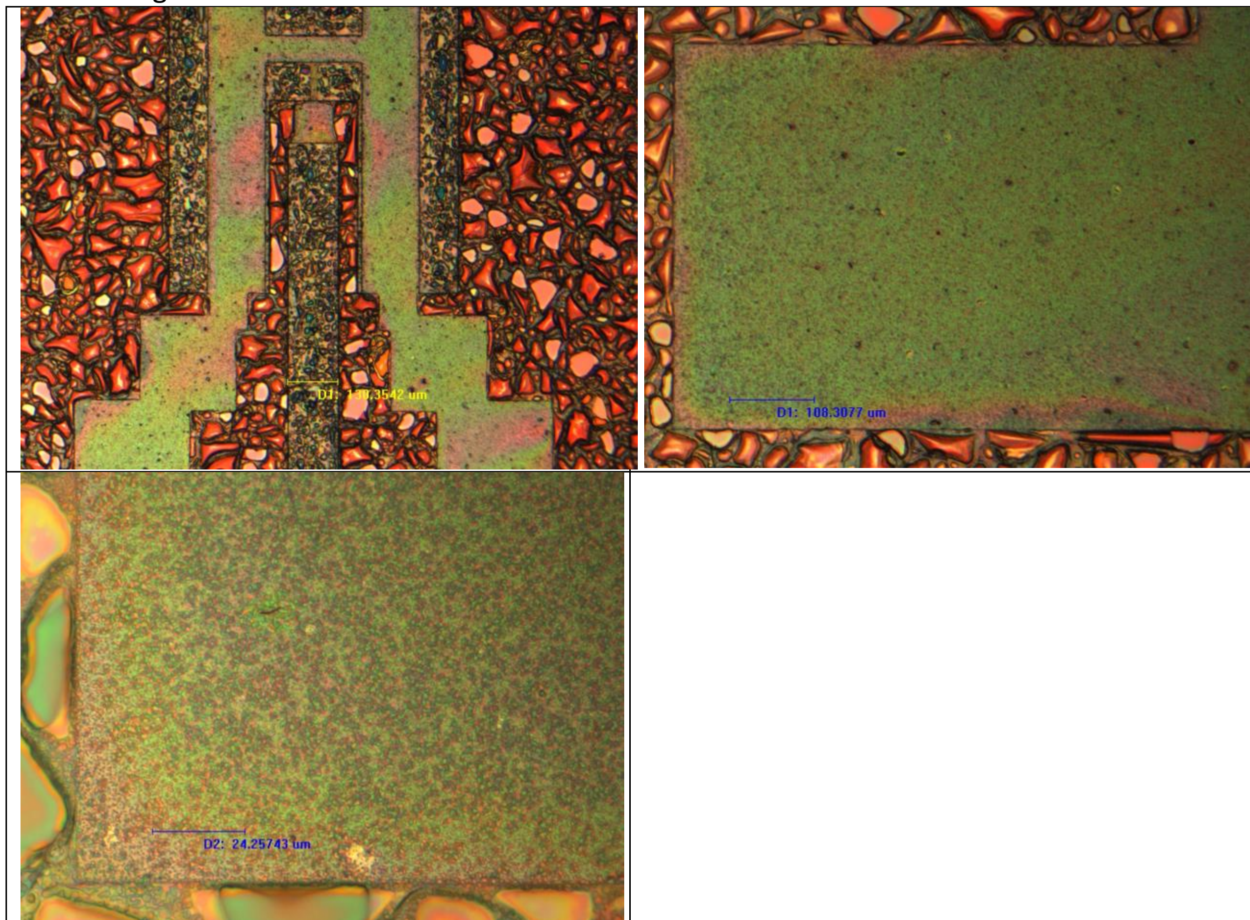

3rd PZT Coating:

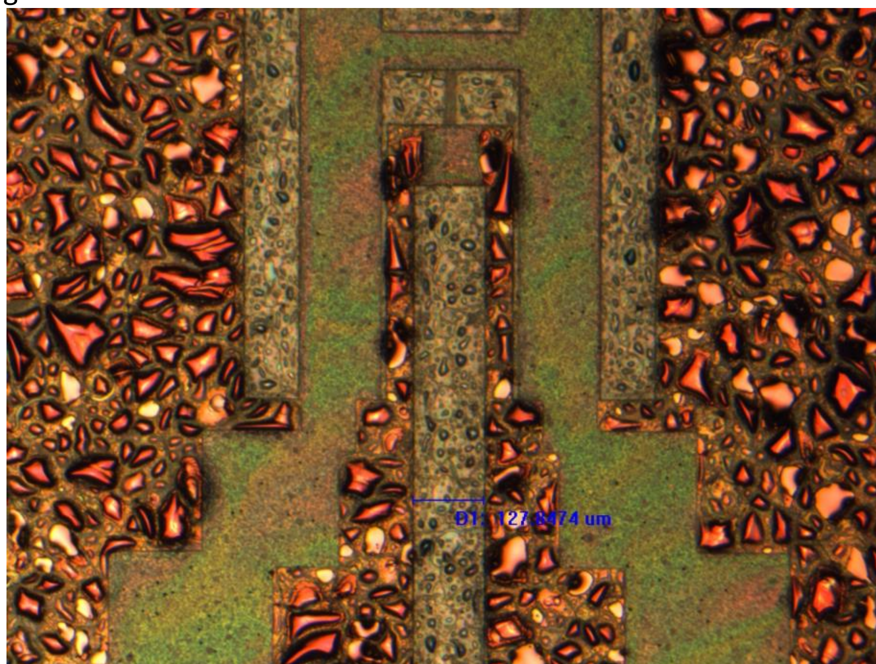

3rd Sintering

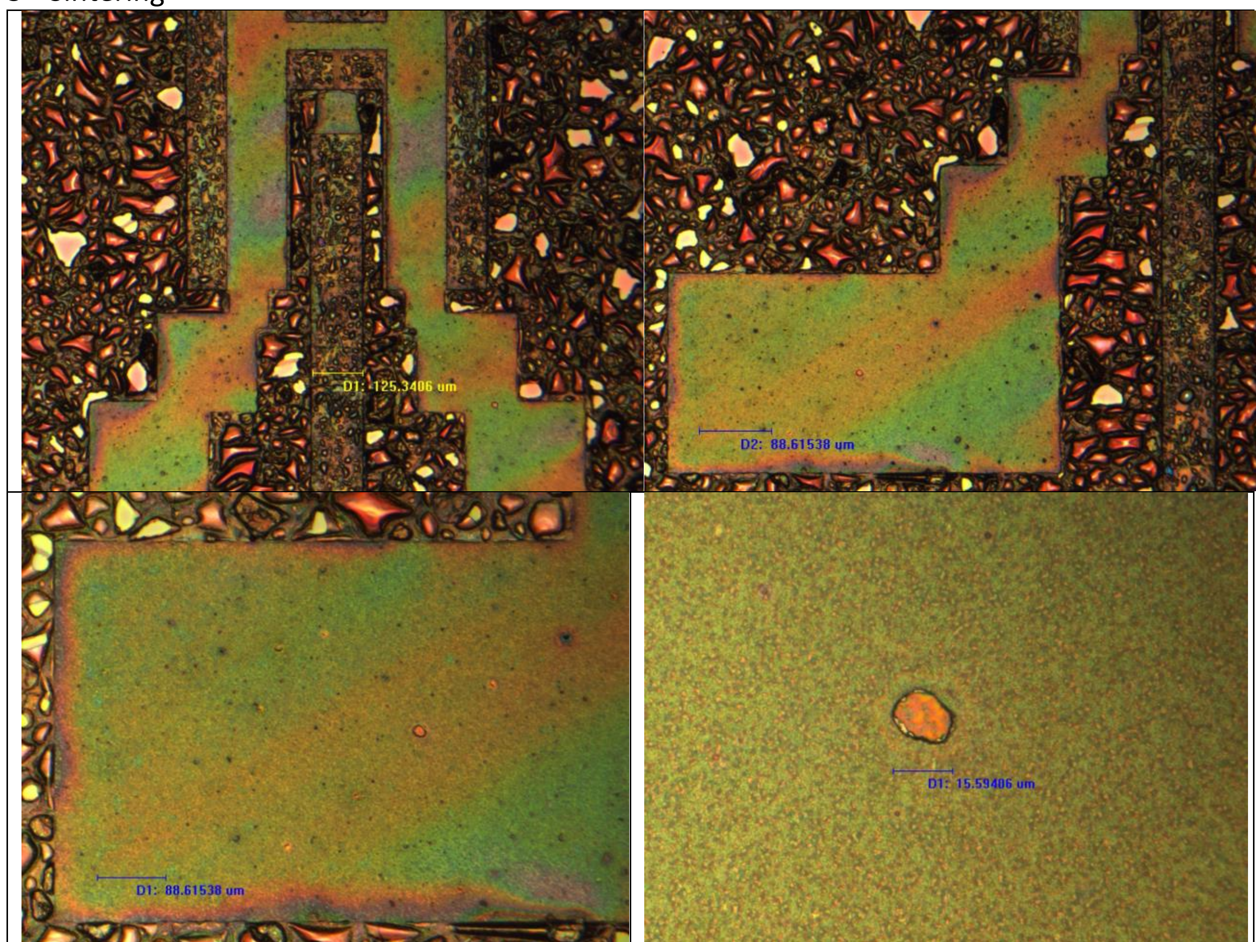

6.0 Top Electrode Patterning, Deposition, and Lift-off

6.1 Patterning

6.1.1 Negative photoresist NR71-1000PY (Futurrex Inc.), 2000 rpm, 40s

6.1.2 Thickness: ~1.2 micron

6.1.3 RIE Descum

Recipe	Descum
Pressure Set (mTorr)	75
RF Power (W)	50
Base Pressure (mTorr)	50
O_2 (sccm)	25
CHF_3 (sccm)	0
SF_6 (sccm)	0
Etch Time (sec.)	30

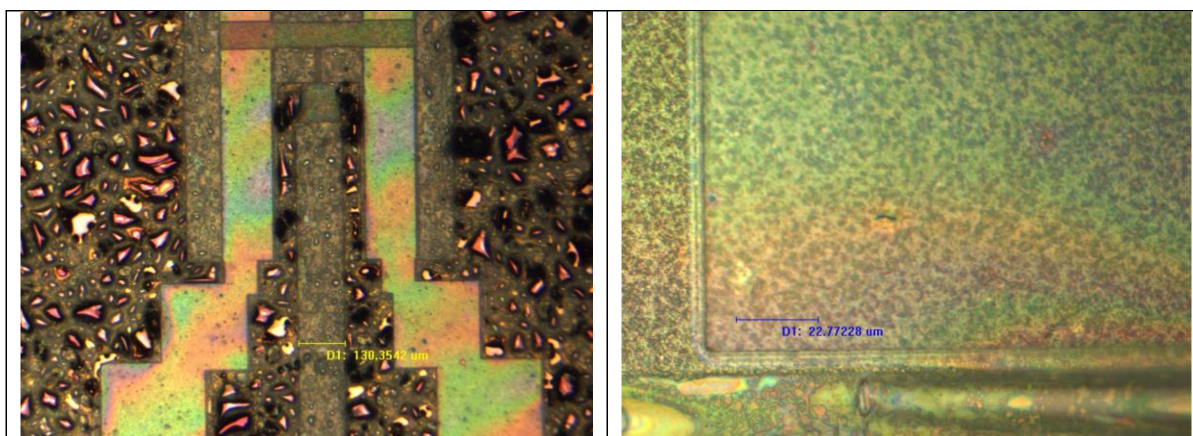

6.2 Deposition:

E-beam evaporator

Material	Titanium	Platinum
Final Thickness (angstrom)	200	1000
Rate (angstrom/sec.)	5	3

6.3 Lift-off:

RR4 resist remover (Futurrex Inc.), 24 hours

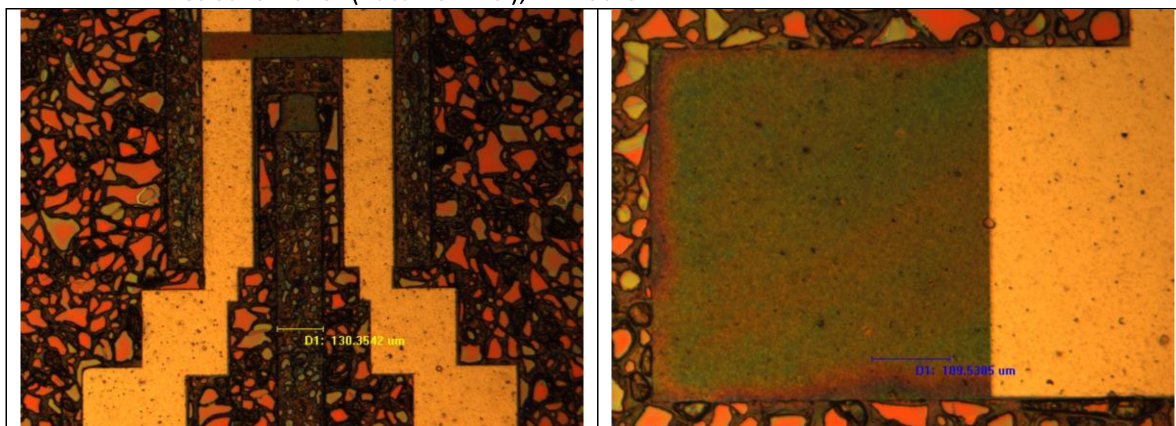

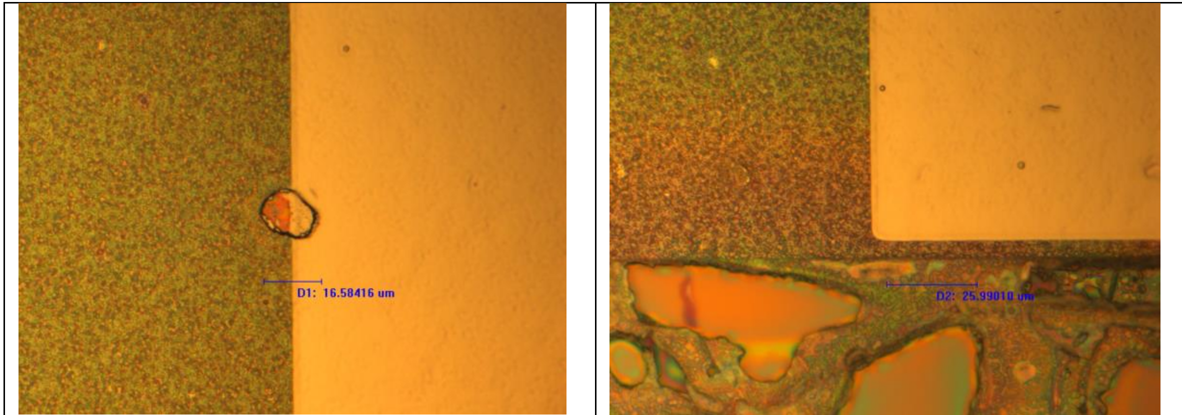

6.0 PZT patterning

6.1 AZ P4620 Coating

Before Hard Bake

After Hard Bake 110℃, 10 minutes.

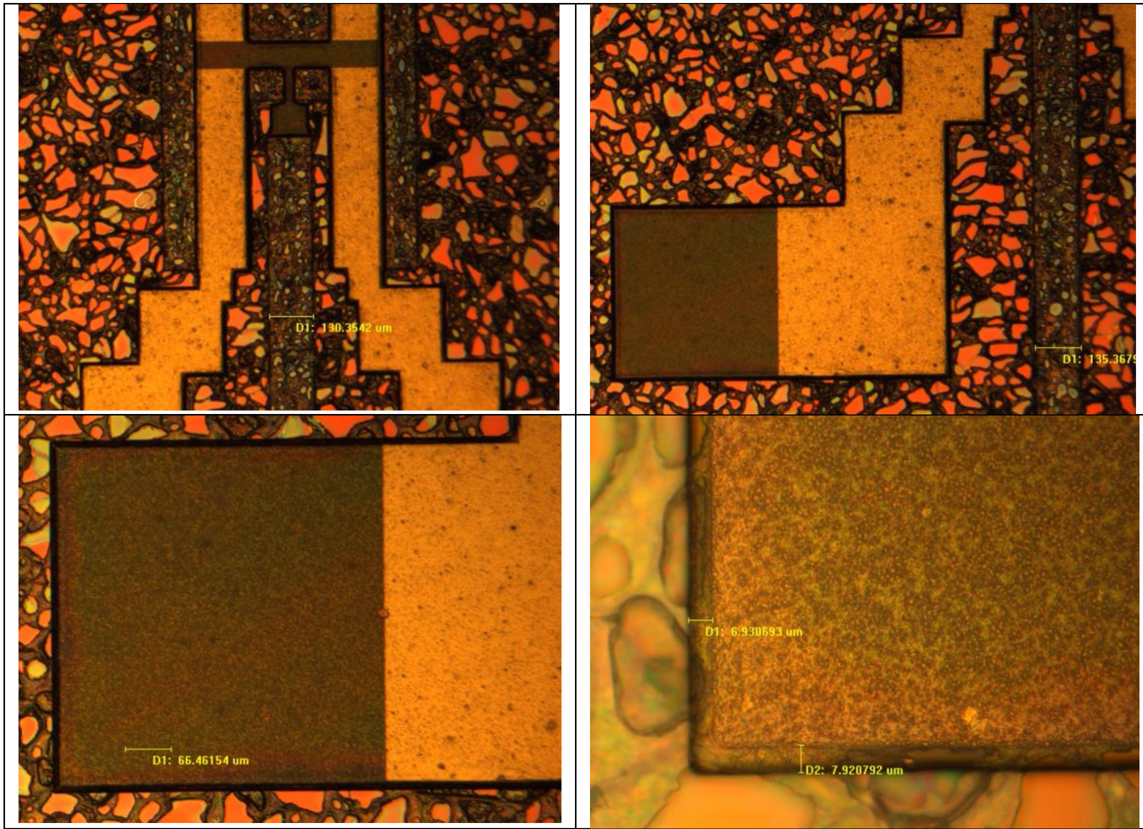

After 10 minutes PZT Wet Etching then Clean Photo Resist

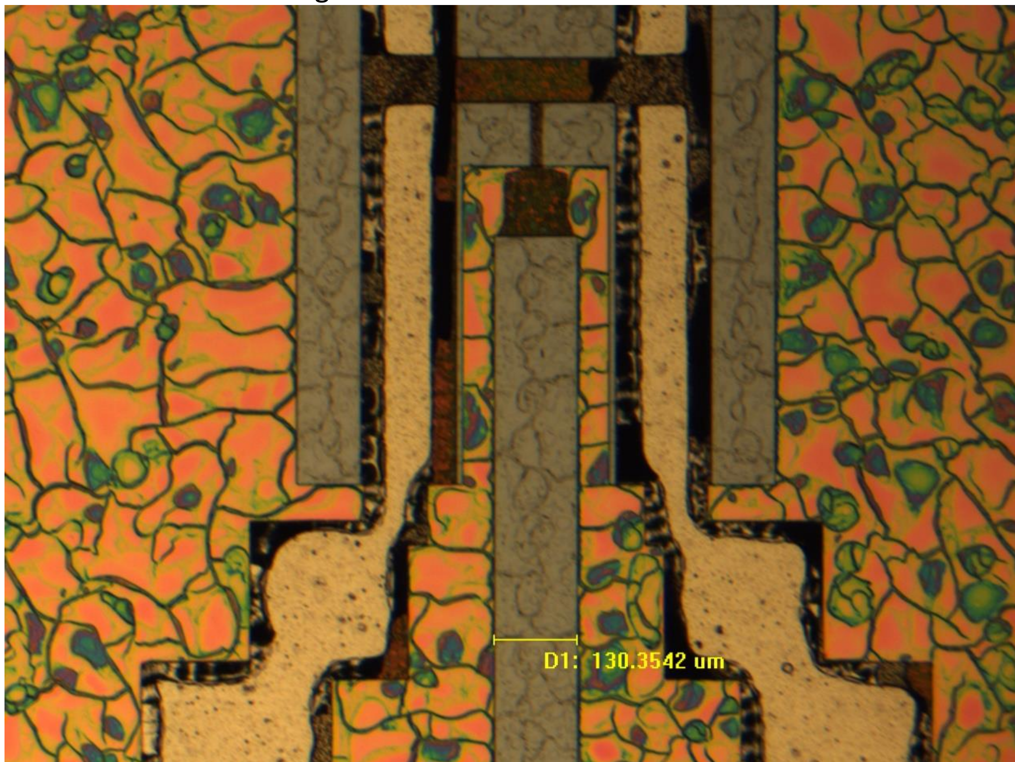

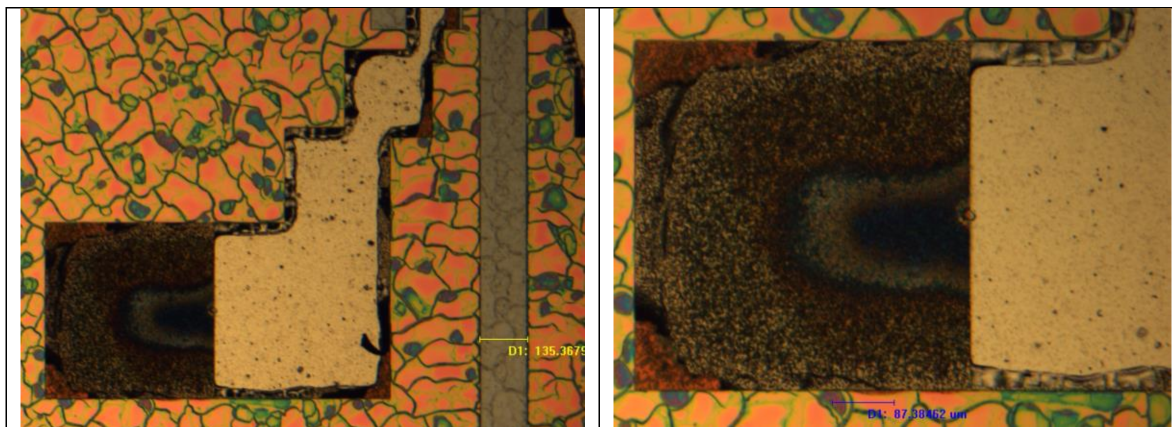

7.0 Fiber Groove Patterning and Deep RIE

7.1 AZ P4620 Patterning

7.1.1 Before Hard Bake:

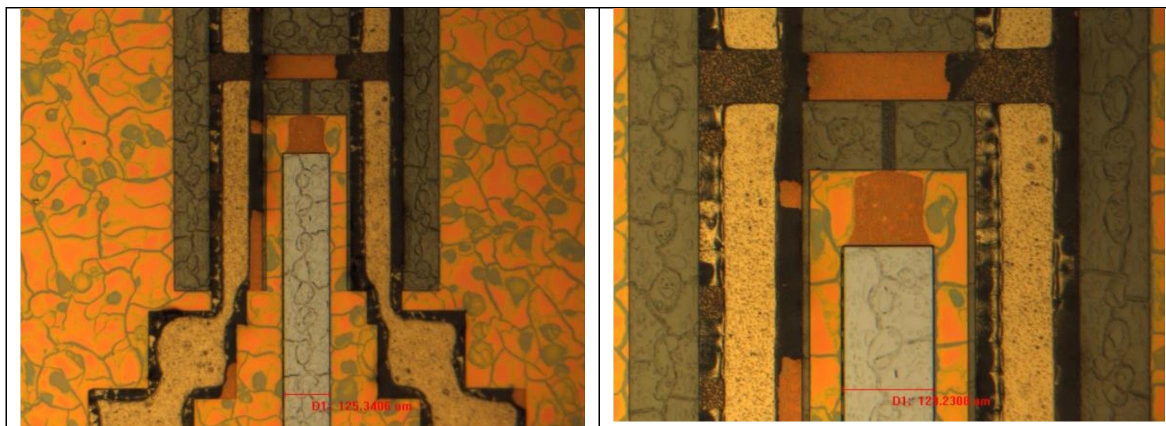

7.1.2 Hard Bake:

Place the sample wafer in a oven at the temperature of 110℃ for 30 minutes.

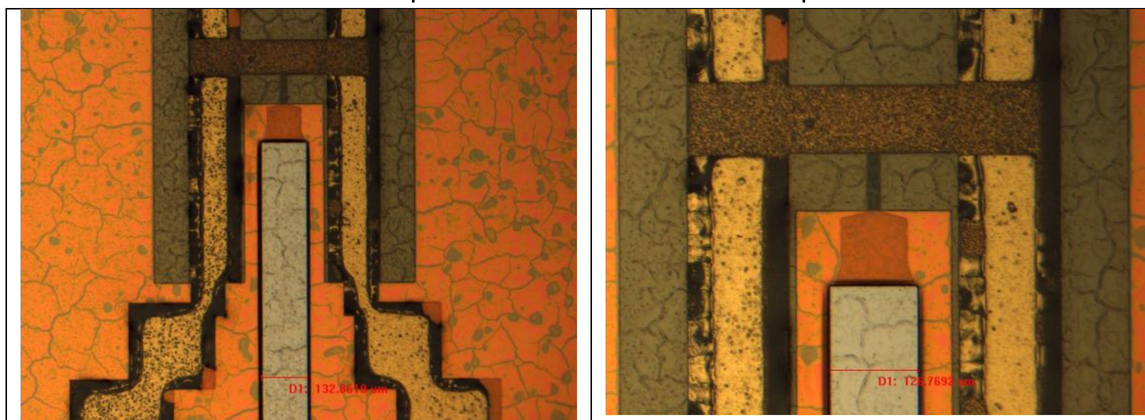

7.2 RIE Descum

7.3 Deep RIE

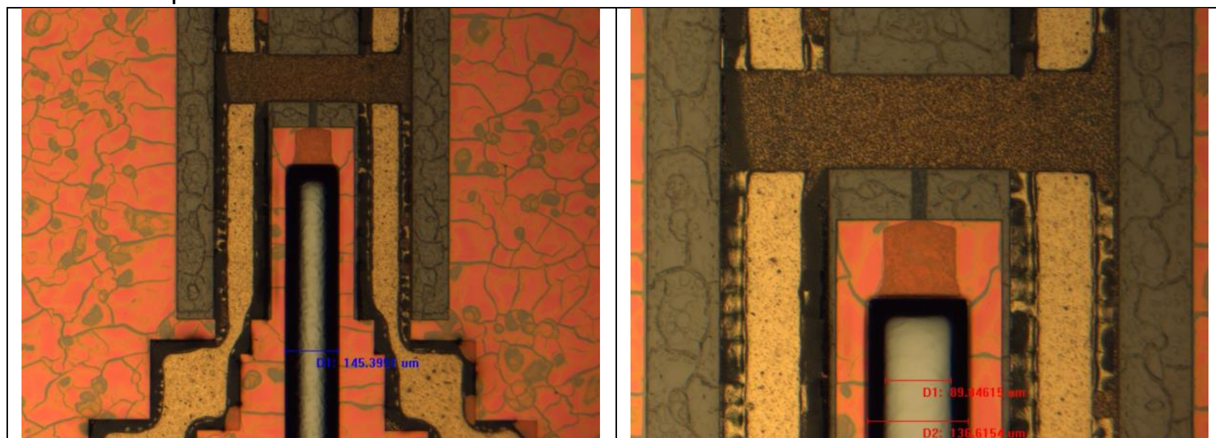

7.4 Clean PR

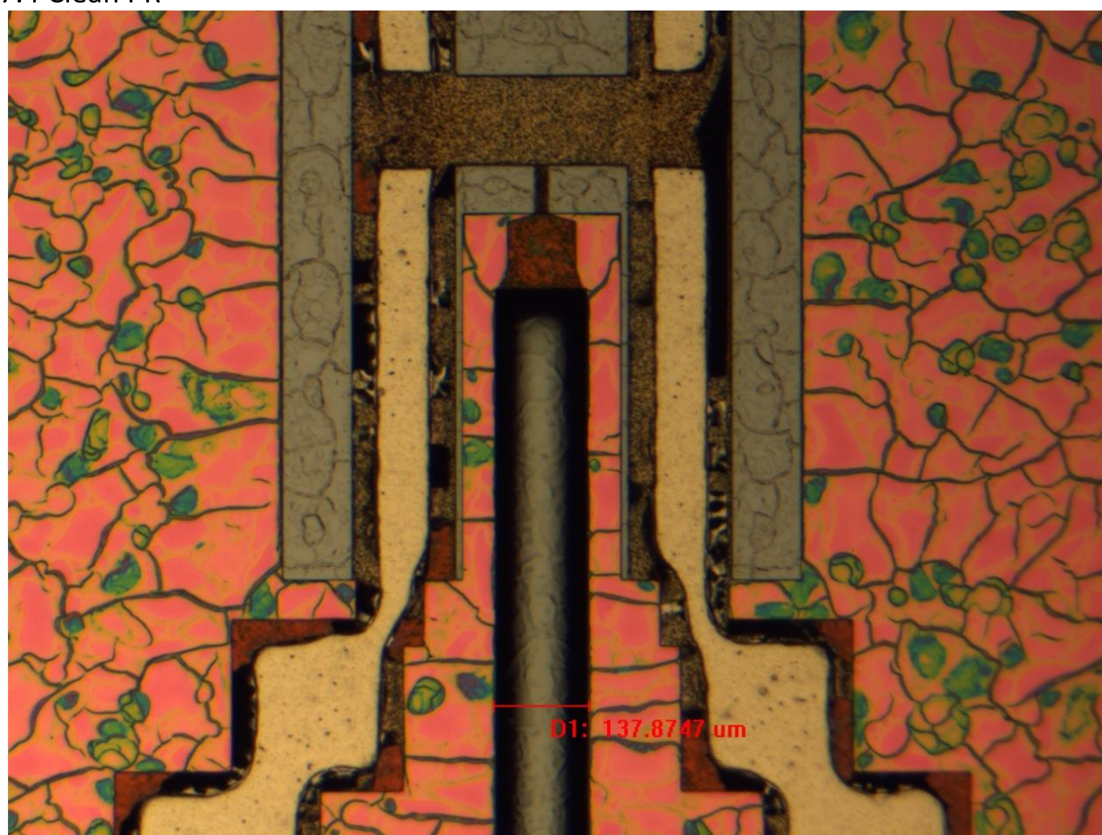

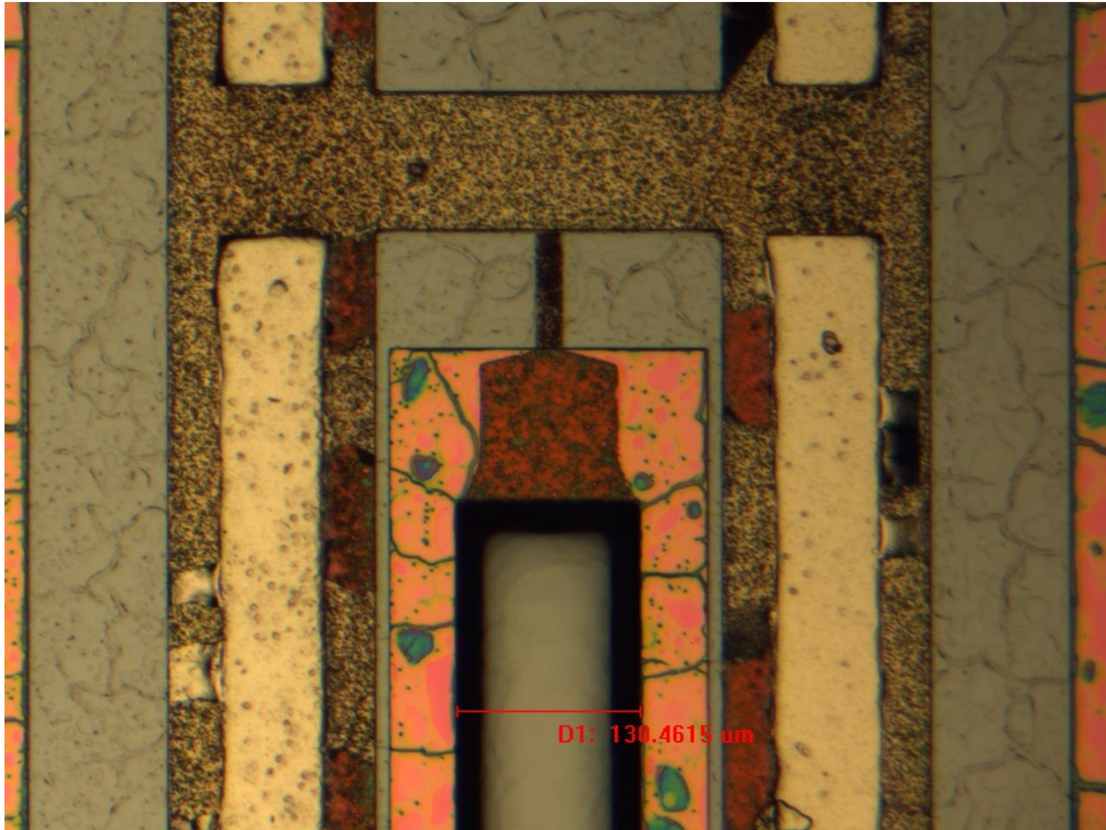

8.0 Sacrificial Layer Patterning

8.1 AZ 1512 Patterning

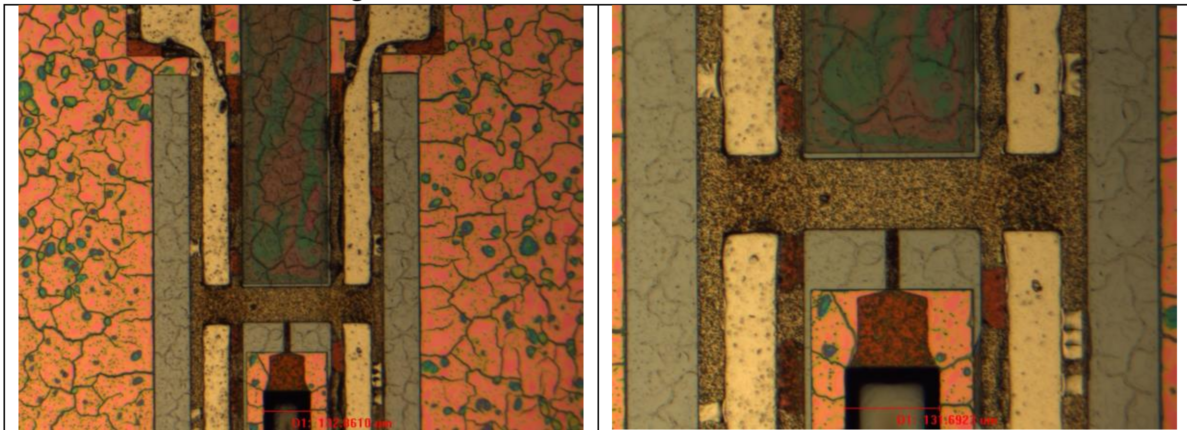

9.0 Double Layers SU8-5 Waveguide

9.1 Photolithography Recipe

9.1.1 1st Coating:

Headway	Spin Speed (rpm)	Ramp Rate (rpm/s)	Time (second)
Step1	500	500	5.0
Step2	3000	1000	40.0

9.1.2 1st Soft Bake:

One minute at 75℃ hotplate.

Three minutes at 105℃ hotplate.

9.1.3 1st Exposure: 6seconds (AB-M Aligner)

9.1.4 1st Post-Exposure Bake

75℃	1 minute
105℃	1 minute

9.1.5 2nd Coating:

Headway	Spin Speed (rpm)	Ramp Rate (rpm/s)	Time (second)
Step1	500	500	5.0
Step2	2750	1000	40.0

9.1.6 2nd Soft Bake:

75℃	1 minute
105℃	3 minute

9.1.7 2nd Exposure: 6 seconds (AB-M Aligner)

9.1.8 2nd Post-Exposure Bake

One minute at 75℃ hotplate.

One minute at 105℃ hotplate.

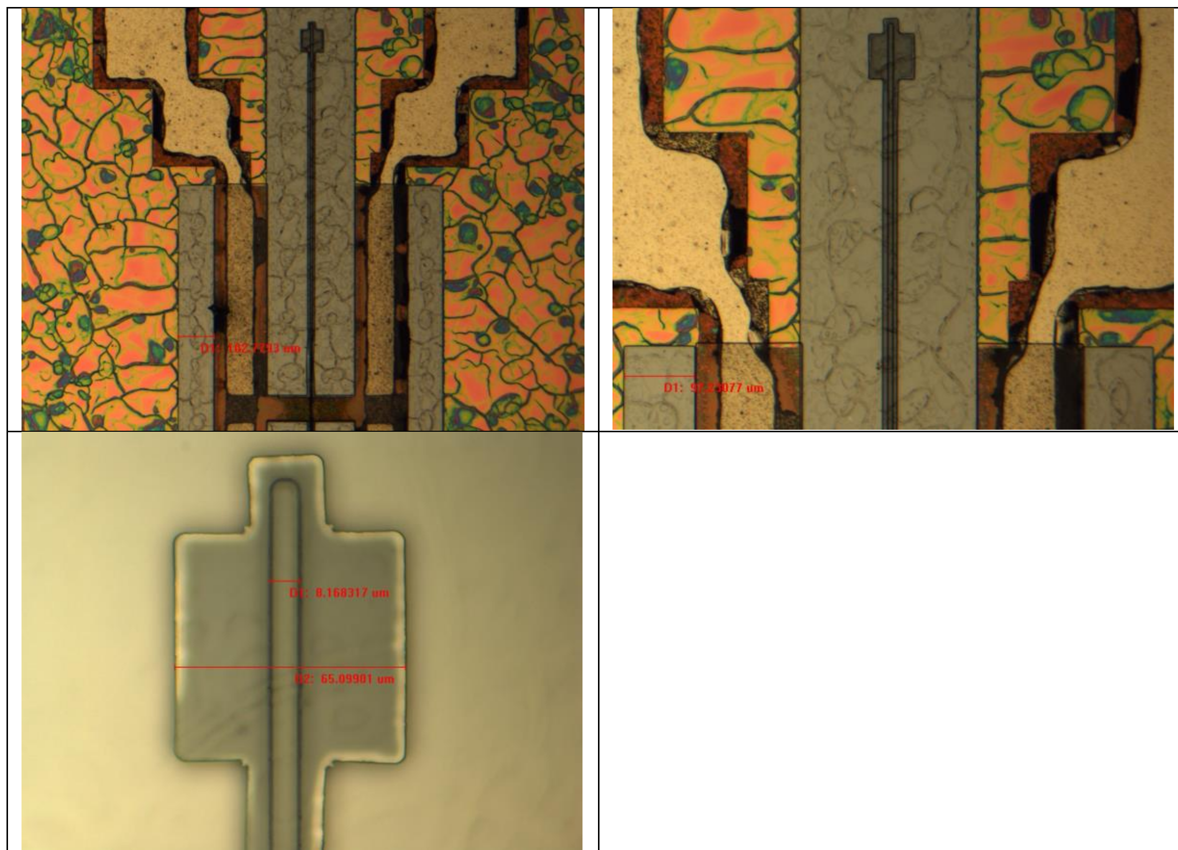

9.2 RIE

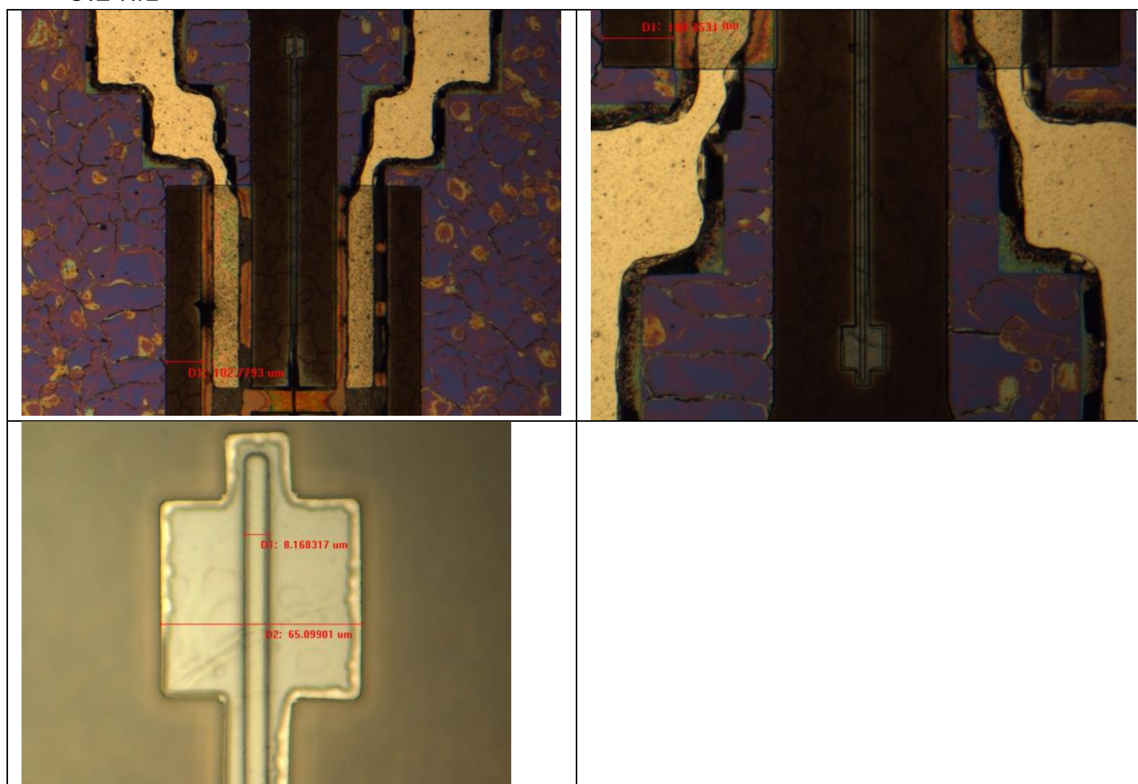

APPENDIX B: ELECTROSTATIC SCANNER MICROFABRICATION PROCESS FLOW

0.0 Purpose

This document provides detailed fabrication process instructions for NIH Electro statics (Ti/ Pt electrodes) scanner.

1.0 Process Flow Diagram

1. Front Side Structure Release
2. Front side Sacrificial Layer
3. SU-8 Waveguide Slab
4. SU-8 Waveguide Ridge
5. Bottom Electrode liftoff
6. Front side Fiber Groove DRIE
7. Backside structure release
8. Bonding with top electrodes

Fabrication flow chart

Fabrication Process – Actuator Portion

(1) Front side Nitride notch for structural release - negative PR, RIE

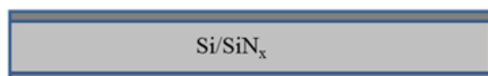

(2) No action

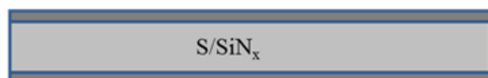

(3) Pattern of SU8 Actuator **(11em)**

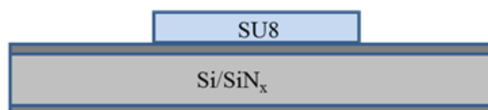

Fabrication Process – Waveguide Portion

(1) Front side Nitride notch for structural release - negative PR, RIE **(04em)**

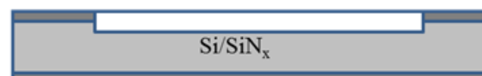

(2) Front side sacrificial layer to level waveguide **(06em)**

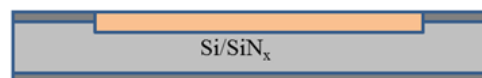

(3) Pattern of SU8 waveguide

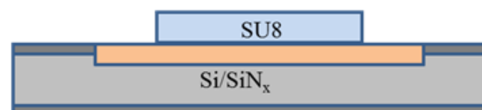

Fabrication Process – Actuator Portion

(4) No Action (13em)

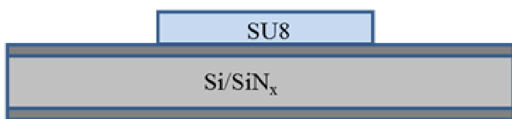

(5) Electrode on top of actuator using E-Beam Evaporation (12es)

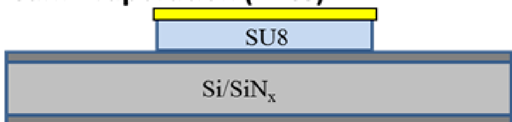

(6) Fiber grooves DRIE

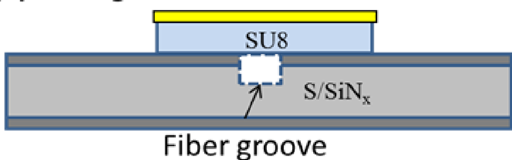

(7) Backside structure release – positive PR, DRIE w/ carrier wafer (02em)

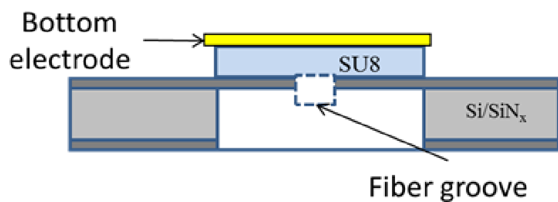

(8) Bonding with top electrodes with Kapton tape

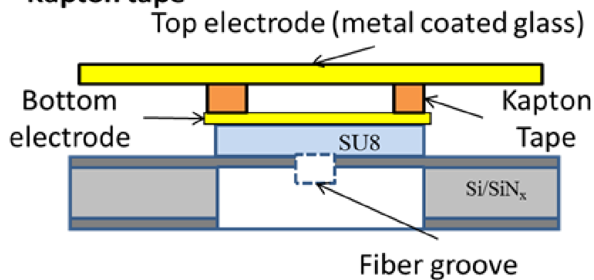

Fabrication Process – Waveguide Portion

Pattern of SU8 waveguide rib (double layer SU 8 process) **(13em)**

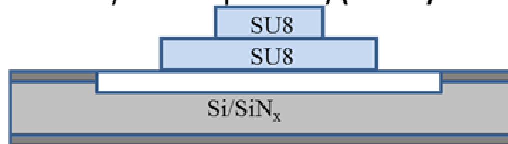

No Action

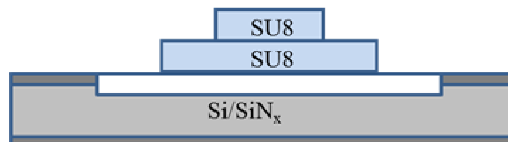

No Action

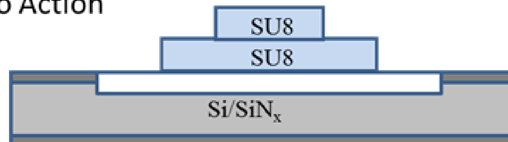

Backside structure release – positive PR, DRIE w/ carrier wafer

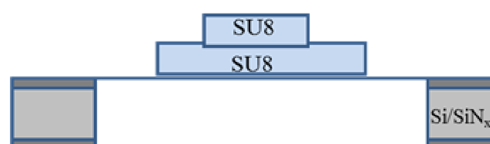

No Action

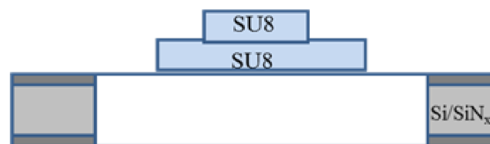

2.0 Wafer Preparation: Piranha Solution Pre-Clean

2.0 Chemicals & Materials:

- Sulfuric acid (H_2SO_4)
- Hydrogen peroxide (H_2O_2)

2.1 Procedure

2.1.1 Pour the following mixture (Piranha) into a clean glass tank.

	1:4 Ratio
H_2O_2	100 ml
H_2SO_4	400ml

2.1.2 Place silicon wafers into Piranha solution immediately after the mixture is made, and start the timer for 20 min.

2.1.3 After 20 minutes (or longer), place the wafers in the dump-rinser, using the standard 3 dump rinse cycle.

2.1.4 Dry the wafers using the standard spin-rinse dry cycle.

3.0 LPCVD Nitride

3.0 Equipment:

- LPCVD

3.1 Chemical & Material: N/A

3.2 Masks: N/A

3.3 Photo resists: N/A

3.4 Procedure:

3.4.1 Please refer to the LPCVD Users Manual for the instructions.

3.4.2 The standard cycle of LPCVD takes 6-8 hours, the target thickness of nitride layer is about 3000~5000 angstrom.

Picture 4. LPCVD in WTC

4.0 Front Side Structure Release

4.0 Mask:

04 em (clear field)

4.1 Photo resist:

NR9-3000PY (negative photoresist)

4.2 Procedure

4.2.1 Dehydration

165 ℃, 3 min.

4.2.2 Coating

4.2.2.1 Please refer to the Headway Spinner Users Manual for complete instructions on programming a spin recipe.

4.2.2.2 Verify a recipe meets the criteria as in the table below

	Speed (rpm)	Ramp (rpm/s)	Dwell (s)
Spread	500	100	5
Spin	3000	1000	40

4.2.3 Soft Bake

4.2.3.1 Pre-heat a hot plate to a temperature of 165 ℃

4.2.3.2 Carefully place the coated wafer directly on the hot plate. Start a timer and bake the wafer for 1 min.

4.2.4 Align

4.2.4.1 Please refer to the EVG Aligner User Manual for the instructions of front side alignment.

4.2.4.2 Set exposure time as 50.0 seconds

4.2.5 Post-Exposure Bake

4.2.5.1 Pre-heat a hot plate to a temperature of 110 ℃

4.2.5.2 Carefully place the coated wafer directly on the hot plate. Start a timer and bake the wafer for 1 min.

4.2.6 Developing exposed wafers

4.2.6.1 Pour the resist developer RD6 into a clean glass beaker

4.2.6.2 Place baked wafer into developer solution and start the timer for 25~30 seconds. Gently agitate the wafer.

4.2.6.3 Rinse the wafers with DI water. Finish rinsing in the dump-rinser, using the standard 3 dump rinse cycle.

4.2.6.4 Dry the wafers using the standard spin-rinse dry cycle.

4.2.7 Hard Bake

N/A

4.3 RIE Descum/Nitride Procedure

4.3.1 RIE Descum

4.3.1.1 Please refer to the RIE Users Manual for the instructions. Place the wafer into RIE machine, select “Oxide” Recipe.

4.3.1.2 Verify a recipe meets the criteria as in the table blow

Pressure Set (mTorr)	50
RF Power (W)	75
Base Pressure (mTorr)	50
O_2 (sccm)	25
CHF_3 (sccm)	0
SF_6 (sccm)	0

4.3.1.3 Edit process time to 30 seconds.

4.3.1.4 Hit “Automatic Process Control”, the recipe will run the process automatically.

4.3.2 RIE Nitride

4.3.2.1 Please refer to the RIE Users Manual for the instructions. Place the wafer into RIE machine, select “Nitride” Recipe.

4.3.2.2 Verify a recipe meets the criteria as in the table blow

Parameter	Value
Pressure Set (mTorr)	130
RF Power (W)	75
Base Pressure (mTorr)	50
O_2 (sccm)	0
CHF_3 (sccm)	0
SF_6 (sccm)	15

4.3.2.3 Edit process time to 110 seconds.

4.3.2.4 Hit “Automatic Process Control”, the recipe will run the process automatically.

4.4 Optical microscope pictures

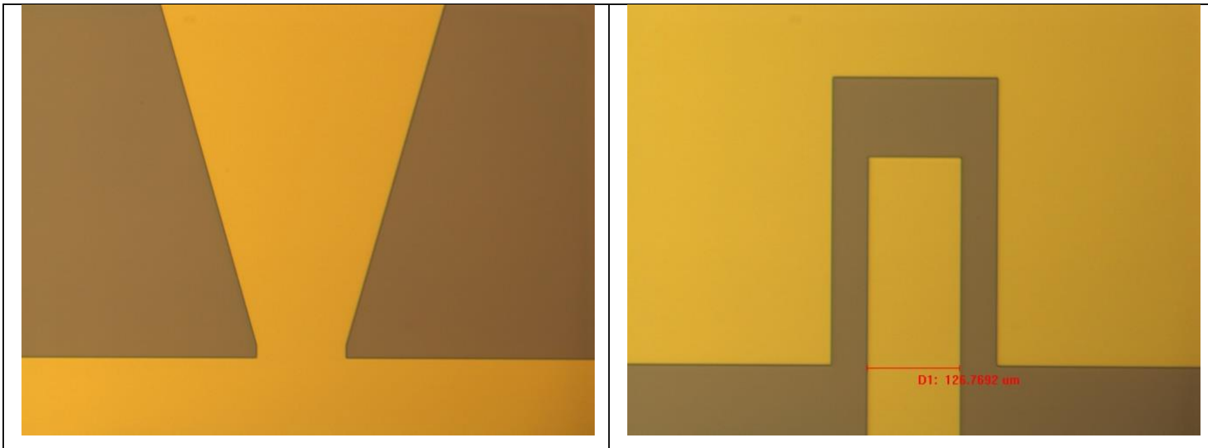

Figure 5. Microscope pictures show front side nitride notch patterning

5.0 Front Side Sacrificial Layer

5.0 Mask

- 06 em (clear field)

5.1 Photoresist

- AZ 1512 (positive photoresist)

5.2 Procedure:

5.2.1 Coating wafer with photoresist

5.2.1.1 Please refer to the CEE Spinner Users Manual for complete instructions on programming a spin recipe.

5.2.1.2 Verify a recipe meets the criteria as in the table below

	Speed (rpm)	Ramp (rpm/s)	Dwell (s)
Spread	500	500	5
Spin	**Corresponding speed**	1000	30

5.2.1.3 For coating the desired thickness of AZ 1512, please refer to the table below to select a corresponding spin speed.

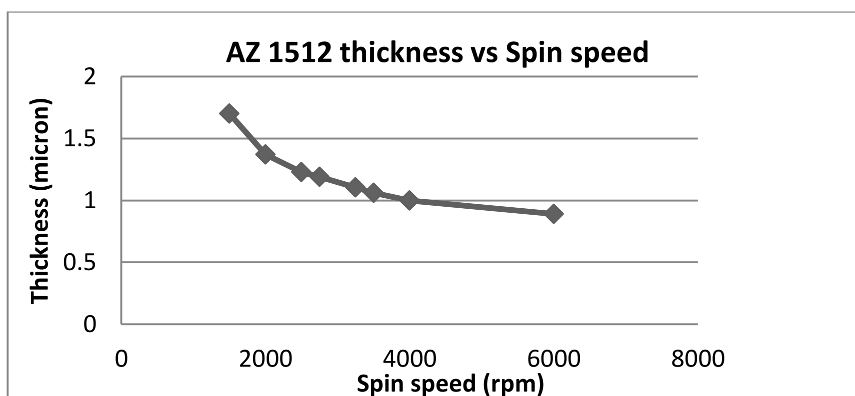

5.2.2 Soft Bake

5.2.2.1 Pre-heat a hot plate to a temperature of 110 ℃

5.2.2.2 Carefully place the coated wafer directly on the hot plate. Start a timer and bake the wafer for 3 min.

5.2.3 Back side alignment

5.2.3.1 Please refer to the EVG Aligner User Manual for the instructions of back side alignment.

5.2.3.2 Set exposure time as 5.0 second

5.2.4 Developing exposed wafers

5.2.4.1 Pour the following mixture into a clean glass beaker

	1:4 Ratio
AZ 351	750 ml
DI water	3000 ml

5.2.4.2 Place wafers into developer solution and start the timer for 30~40 seconds. Mild agitation.

5.2.4.3 Rinse the wafers with DI water. Finish rinsing in the dump-rinser, using the standard 3 dump rinse cycle.

5.2.4.4 Dry the wafers using the standard spin-rinse dry cycle.

5.2.5 Hard Bake/Descum: 110℃, 2 minutes.

5.3 Microscope pictures

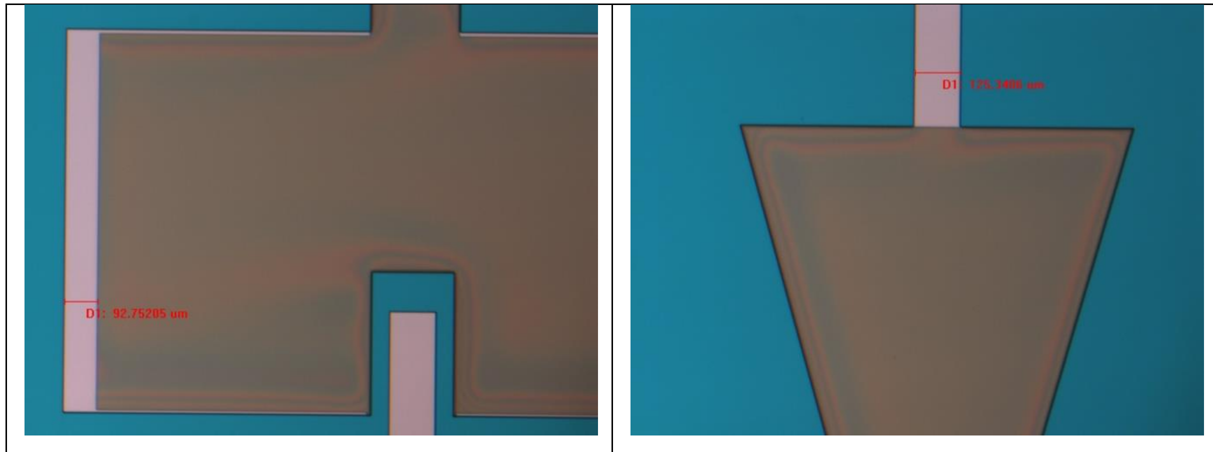

Figure 6. Microscope pictures show positive photoresist AZ 1512 as a sacrificial layer fill in the front nitride opening.

6.0 SU-8 Actuator

6.0 Mask

- 11 ES (D) (clear field)
- 13-3.9 ES (dark field)

6.1 Photoresist

- SU8-2 (negative photoresist)

6.2 Procedure:

6.2.1 Coating wafer with SU8-2

6.2.1.1 Please refer to the Headway Spinner Users Manual for complete instructions on programming a spin recipe.

6.2.1.2 Verify a recipe meets the criteria as in the table below

	Speed (rpm)	Ramp (rpm/s)	Dwell (s)
Spread	500	100	5
Spin	2000	300	30

6.2.2 Soft Bake

6.2.2.1 Pre-heat two hot plates to temperature of 70°C and 105 °C, separately.

6.2.2.2 Carefully place the coated wafer directly on the 70°C hot plate. Start a timer and bake the wafer for 1 min.

6.2.2.3 Carefully move the wafer from 70°C hot plate to 105°C hotplate. Start a timer and bake the wafer for 15 minutes.

6.2.3 Relaxation Time: 10 minutes.

6.2.4 Alignment

6.2.4.1 Please refer to the AB-M Aligner User Manual for the instructions of front side alignment.

6.2.4.2 Set exposure time as 8.0 seconds.

6.2.5 Post-Exposure Bake

6.2.5.1 Carefully place the coated wafer directly on the 70°C hot plate. Start a timer and bake the wafer for 1 min.

6.2.5.2 Carefully move the wafer from 70°C hot plate to 105°C hotplate. Start a timer and bake the wafer for 1 minute.

6.2.5.3 Let the wafer slowly cool down at least 20 minutes.

6.2.6 Coating the second layer SU8-2

6.2.6.1 Please refer to the Headway Spinner Users Manual for complete instructions on programming a spin recipe.

6.2.6.2 Verify a recipe meets the criteria as in the table below

	Speed (rpm)	Ramp (rpm/s)	Dwell (s)
Spread	500	500	5
Spin	2000	1000	40

6.2.7 2nd Soft Bake

6.2.7.1 Carefully place the coated wafer directly on the 75℃ hot plate. Start a timer and bake the wafer for 1 min.

6.2.7.2 Carefully move the wafer from 75℃ hot plate to 105℃ hotplate. Start a timer and bake the wafer for 3 minutes.

6.2.8 2nd Alignment

6.2.8.1 Please refer to the AB-M Aligner User Manual for the instructions of front side alignment.

6.2.8.2 Set exposure time as 6 second.

6.2.9 2nd Post exposure Bake

6.2.9.1 Carefully place the coated wafer directly on the 75℃ hot plate. Start a timer and bake the wafer for 1 min.

6.2.9.2 Carefully move the wafer from 75℃ hot plate to 105℃ hot plate. Start a timer and bake the wafer for 1 minute.

6.2.10 Developing exposed wafers

6.2.10.1 PourSU8 developer and IPA into clean glass beakers respectively.

6.2.10.2 Place wafers into developer solution and start the timer for 75 seconds. Gently agitate the wafers.

6.2.10.3 Rinse the wafers with IPA. Finish rinsing in the dump-rinser, using the standard 3 dump rinse cycle.

6.2.10.4 Dry the wafers using the standard spin-rinse dry cycle.

6.2.11 Hard Bake/Descum

No hard Bake/Descum needed.

6.3 Pictures

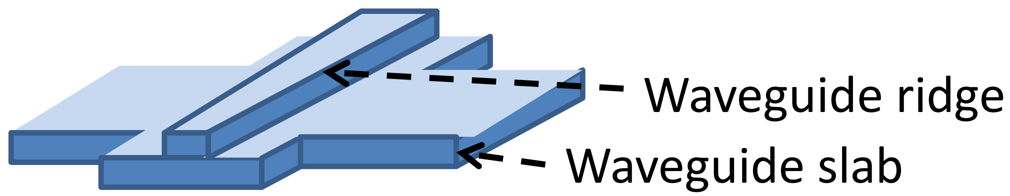

Picture 7.1 a schematic diagram of double-layer SU-8 cantilever.

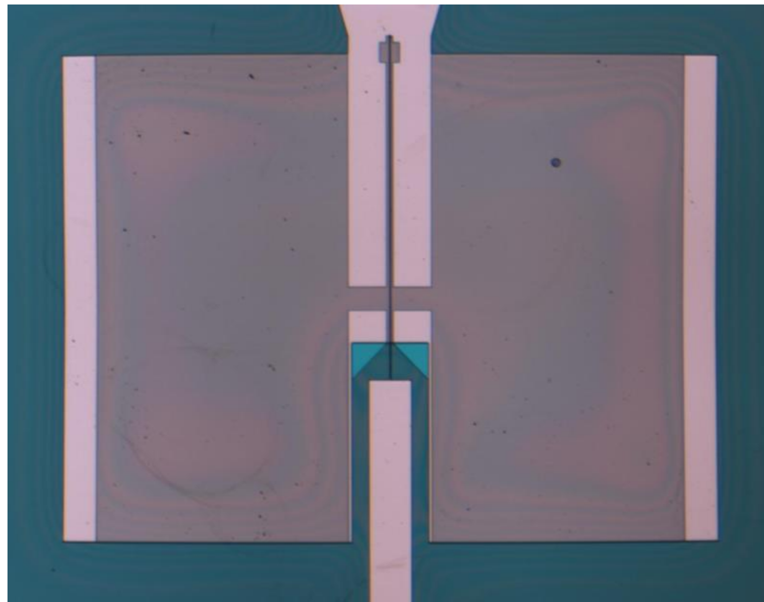

Figure 7.2 a panorama view of a double-layer SU-8 device includes waveguide and pads.

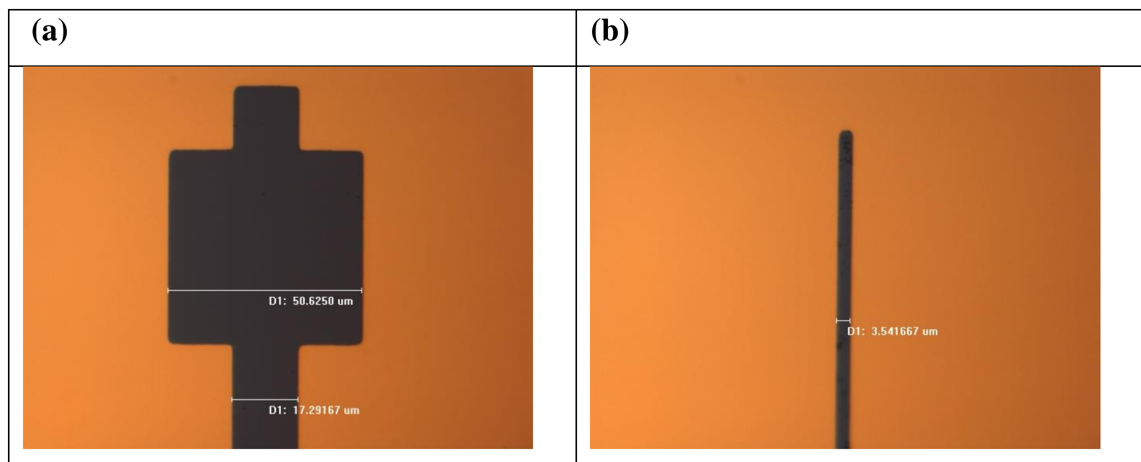

Figure 7.3 Inspection of the photo mask. (a) waveguide slab part and (b), waveguide ridge part.

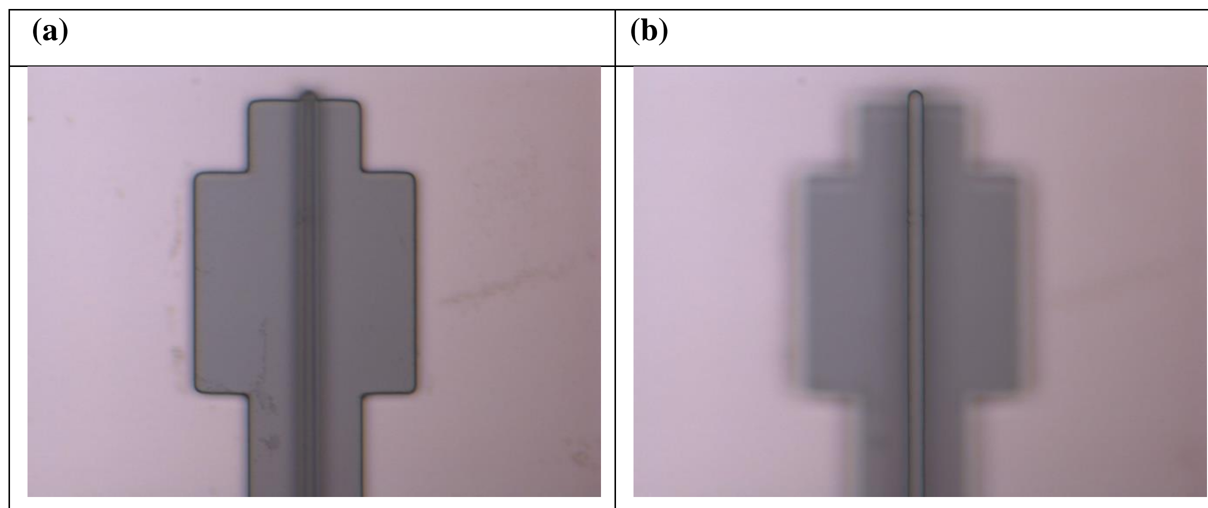

Figure 7.4 Microscope pictures show lithography result of the double-layer SU-8 waveguide tip. (a) focus on the slab, and (b) focus on the ridge.

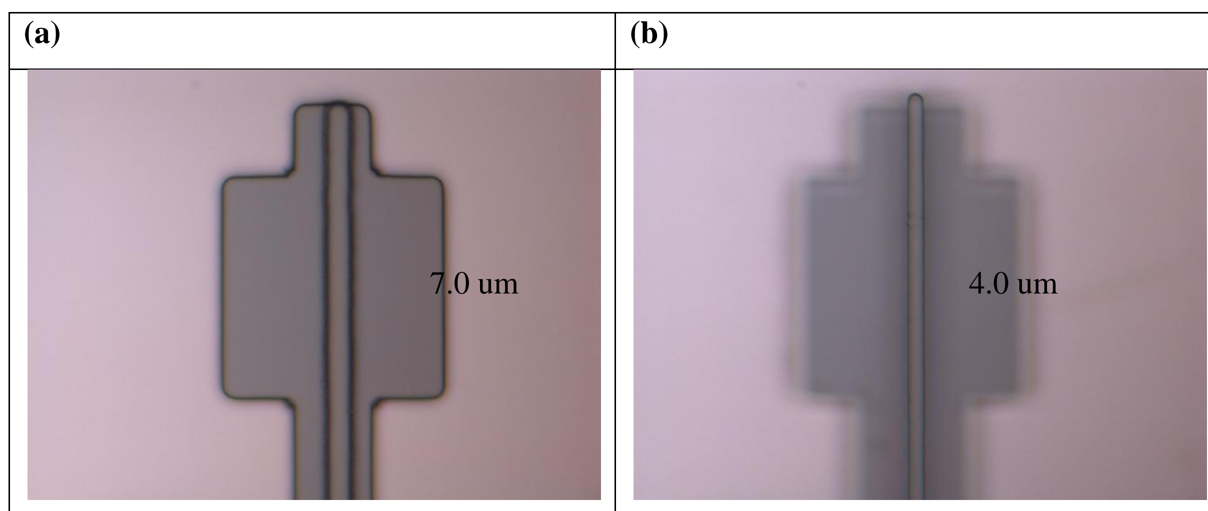

Figure 7.5 Microscope inspection shows how different alignment contact methods affect the lithography dimension. (a) hard contact and (b), vacuum contact.

7.0 Bottom Electrode Lift-Off

7.0 Mask:

- 12 ES (clear field)

7.1 Photo resists

- Negative photoresist NR9-3000PY (Futurrex Inc.)

7.2 Lithography:

7.2.1 OmniCoat™

7.2.1.1 **Coating**

7.2.1.1.1 Please refer to the CEE Spinner Users Manual for complete instructions on programming a spin recipe.

7.2.1.1.2 Verify a recipe meets the criteria as in the table below

	Speed (rpm)	Ramp (rpm/s)	Dwell (s)
Spread	500	100	5
Spin	3000	300	30

7.2.1.2 **Soft Bake**

7.2.1.2.1 Pre-heat a hot plate to a temperature of 200 ℃

7.2.1.2.2 Carefully place the coated wafer directly on the hot plate. Start a timer and bake the wafer for 1 min.

7.2.2 NR9-3000PY

7.2.2.1 **Coating**

7.2.2.1.1 Please refer to the CEE Spinner Users Manual for complete instructions on programming a spin recipe.

7.2.2.1.2 Verify a recipe meets the criteria as in the table below

	Speed (rpm)	Ramp (rpm/s)	Dwell (s)
Spread	500	100	5
Spin	1000	1000	40

7.2.3 Soft Bake

7.2.3.1 Pre-heat a hot plate to a temperature of 165 ℃

7.2.3.2 Carefully place the coated wafer directly on the hot plate. Start a timer and bake the wafer for 1 min.

7.2.4 Align

7.2.4.1 Please refer to the EVG Aligner User Manual for the instructions of front side alignment.

7.2.4.2 Set exposure time as 50.0 second.

7.2.5 Post-Exposure Bake

7.2.5.1 Pre-heat a hot plate to a temperature of 110 ℃

7.2.5.2 Carefully place the coated wafer directly on the hot plate. Start a timer and bake the wafer for 1 min.

7.2.6 Developing exposed wafers

7.2.6.1 Pour the following FuturRex negative photoresist developer RD6 into a clean glass beaker

7.2.6.2 Place wafers into developer solution and start the timer for **20 minutes**. Gently agitate the wafers.

7.2.6.3 Rinse the wafers with DI water. Finish rinsing in the dump-rinser, using the standard 3 dump rinse cycle.

7.2.6.4 Dry the wafers using the standard spin-rinse dry cycle.

7.2.7 Hard Bake:

N/A

7.3 E-beam Evaporation Procedure

7.3.1 Please refer to E-Beam Evaporator Users Manual for complete instructions.

7.3.2 Deposit titanium for 200 Angstrom first, then Nickel for 2000 Angstrom.

7.4 Lift-off Procedure

7.4.1 Pour acetone into a clean plastic container.

7.4.2 Place the sample wafer into acetone. Wait for 5 minutes.

7.5 pictures:

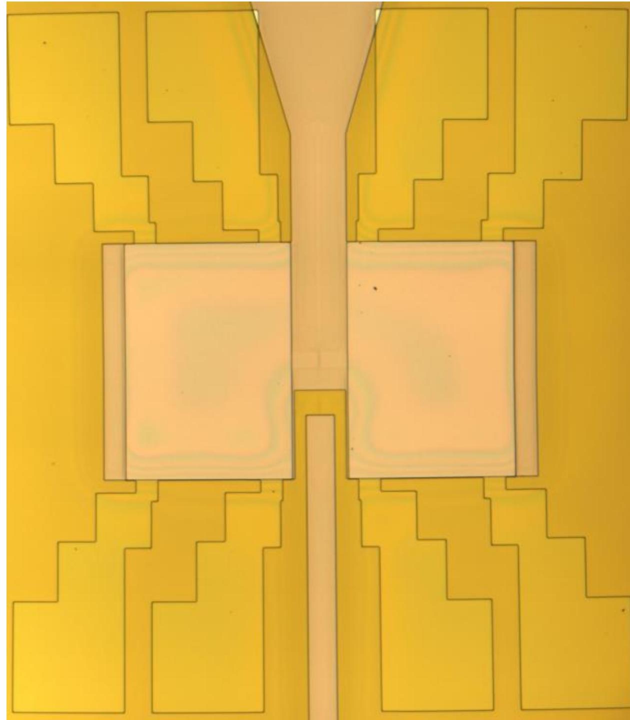

Figure 8.1. Microscope picture shows lithographic patterning of negative photoresist NR9-3000PY on top of SU-8

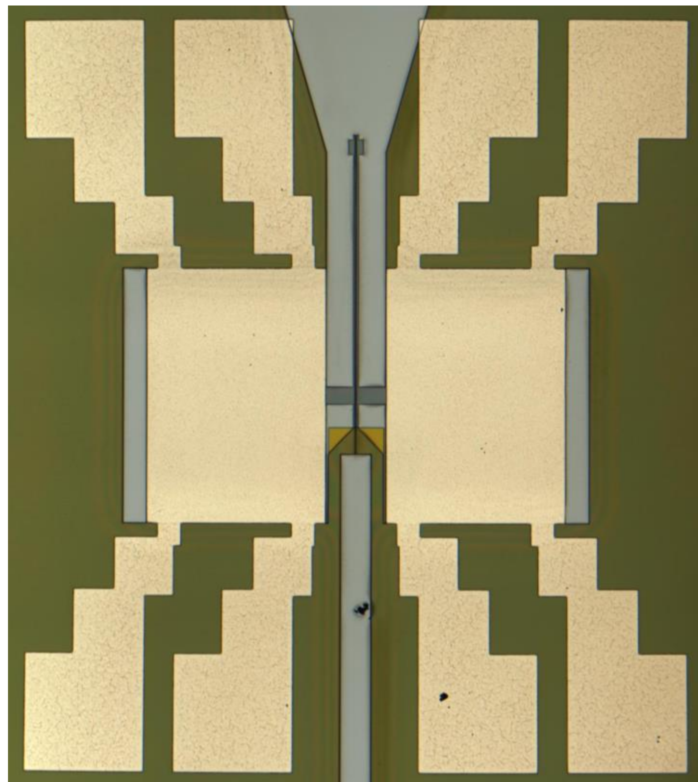

Figure 8.2. Microscope picture shows bottom electrode Ti/Pt lift-off result.

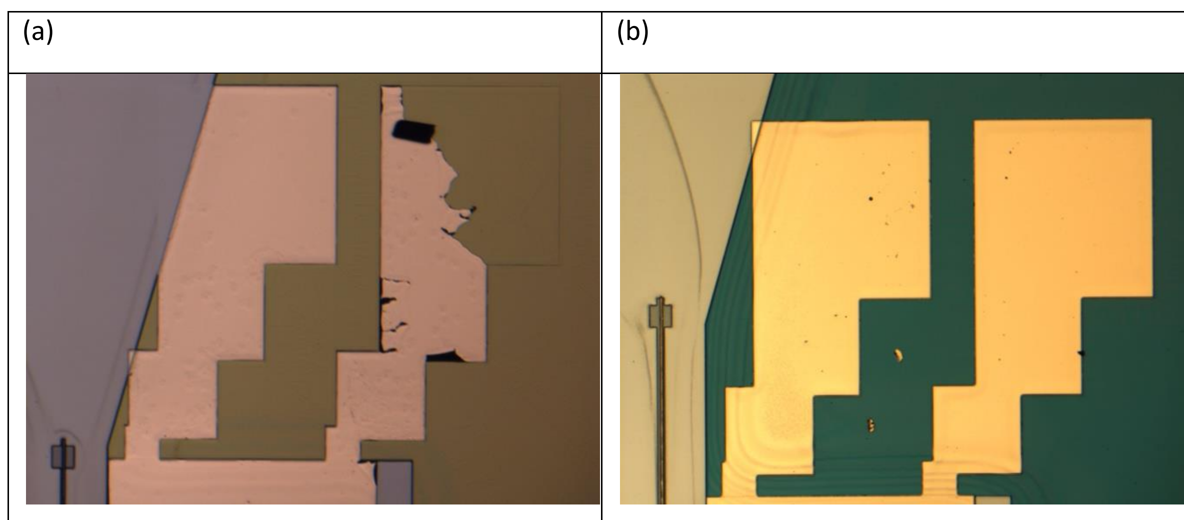

Figure 8.3 Microscope pictures show oxygen plasma RIE can improve the adhesion between SU-8 surface and metal. (a) bottom electrodes lift-off without pre-oxygen plasma RIE. (b) bottom electrodes lift-off with pre-oxygen plasma RIE.

8.0 Front Side Fiber Groove and Dividers DeepRIE

8.0 Mask

- A (clear field)

8.1 Photo resist:

- NR9-3000PY (Positive photo resist)

8.2 Procedure:

8.2.1 Dehydration

165 ℃, 3 min.

8.2.2 Coating

8.2.2.1 Please refer to the Headway Spinner Users Manual for complete instructions on programming a spin recipe.

8.2.2.2 Verify a recipe meets the criteria as in the table below

	Speed (rpm)	Ramp (rpm/s)	Dwell (s)
Spread	500	100	5
Spin	3000	1000	40

8.2.3 Soft Bake

8.2.3.1 Pre-heat a hot plate to a temperature of 165 ℃

8.2.3.2 Carefully place the coated wafer directly on the hot plate. Start a timer and

bake the wafer for 1 min.

8.2.4 Align

8.2.4.1 Please refer to the EVG Aligner User Manual for the instructions of front side alignment.

8.2.4.2 Set exposure time as 50.0 second

8.2.5 Post-Exposure Bake

8.2.5.1 Pre-heat a hot plate to a temperature of 110 ℃

8.2.5.2 Carefully place the coated wafer directly on the hot plate. Start a timer and bake the wafer for 1 min.

8.2.6 Developing exposed wafers

8.2.6.1 Pour the resist developer RD6 into a clean glass beaker

8.2.6.2 Place baked wafer into developer solution and start the timer for 25~30 seconds. Gently agitate the wafer.

8.2.6.3 Rinse the wafers with DI water. Finish rinsing in the dump-rinser, using the standard 3 dump rinse cycle.

8.2.6.4 Dry the wafers using the standard spin-rinse dry cycle.

8.2.7 Hard Bake

N/A

8.3 RIE Nitride/Oxide Procedure

8.3.1 Please refer to the RIE Users Manual for the instructions. Place the wafer into RIE machine, select "Nitride" Recipe.

8.3.2 Verify a recipe meets the criteria as in the table blow

Pressure Set (mTorr)	130
RF Power (W)	75
Base Pressure (mTorr)	50
O_2 (sccm)	0
CHF_3 (sccm)	0
SF_6 (sccm)	15

8.3.3 Edit process time to 3 minutes (180 seconds).

8.3.4 Hit "Automatic Process Control", the recipe will run the process automatically.

8.3.5 After the process finishes, select "Oxide" recipe from the main menu.

8.3.6 Verify a recipe meets the criteria as in the table blow.

Pressure Set (mTorr)	70
RF Power (W)	75
Base Pressure (mTorr)	50
O_2 (sccm)	2
CHF_3 (sccm)	25
SF_6 (sccm)	0

8.3.7 Edit process time to 12 minutes (720 seconds).

8.3.8 Hit "Automatic Process Control", the recipe will run the process automatically.

8.4 Deep RIE

8.4.1 Place the wafer into Deep RIE machine. Please refer to the Deep RIE User Manual for complete instructions on operating Deep RIE.

8.4.2 Update the recipe time to meets the criteria for the target etching thickness.

- Etch Time Calculation: Etch time is entered as number of loops completed. The machine runs through 5 loops a minute, so if you want to etch for 30 minutes, you will have 150 loops.
- WTC standard Bosch

	SF6 (sccm)	C4F8 (sccm)	Time (sec.)
Etch	100	1	7
Deposition	1	100	5
Exposed area	~ 10%		
Ideal Etch rate	3.6 +/-.3 µm/min (10% exposed area)		

8.5 Pictures

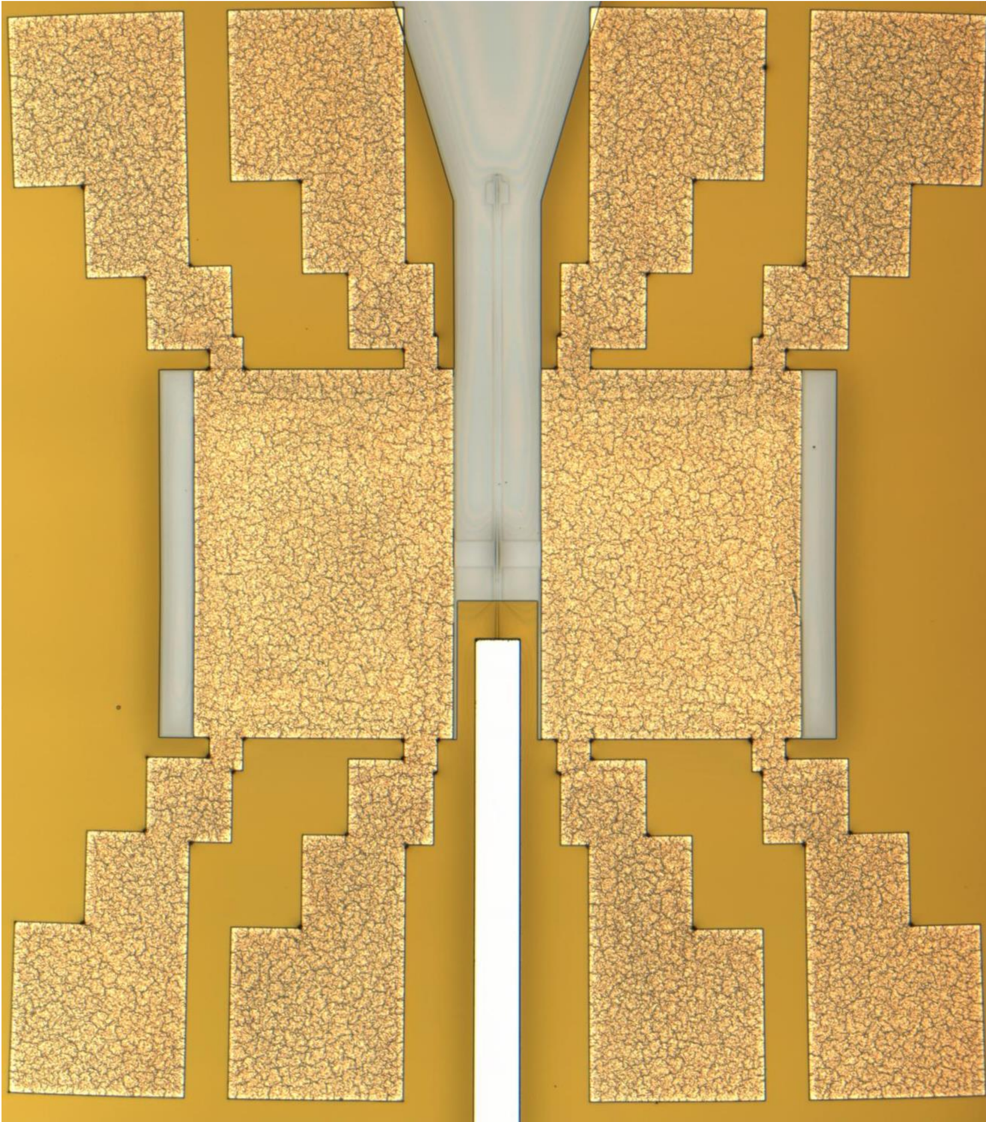

Figure 9. A panorama view of the lithography result of the fiber groove (pre-DRIE).

9.0 Backside structure release (AZ P4620 11µm)

9.0 Mask

- 02 EM (dark field)

9.1 Photoresist

- AZ P4620 (positive photoresist)

9.2 Procedure:

9.2.1 Coating wafer with photoresist

9.2.1.1 Please refer to the CEE Spinner Users Manual for complete instructions on programming a spin recipe.

9.2.1.2 Verify a recipe verify the criteria as in the table below

	Speed (rpm)	Ramp (rpm/s)	Dwell (s)
Spread	300	300	3
Spin	1500	1200	30
Spin	2000	1200	5

9.2.2 Soft Bake

9.2.2.1 Pre-heat a hot plate to a temperature of 110 ℃

9.2.2.2 Carefully place the coated wafer directly on the hot plate. Start a timer and bake the wafer for 2 min.

9.2.2.3 Load wafers into a metal cassette and place cassette into 110℃ oven with wafers in a horizontal orientation for 15 minutes.

9.2.3 Back side alignment

9.2.3.1 Please refer to the EVG Aligner User Manual for the instructions of back side alignment.

9.2.3.2 Set exposure time as 55.0 second

9.2.4 Developing exposed wafers

9.2.4.1 Pour the following mixture into a clean glass beaker

	1:4 Ratio
AZ 400K	750 ml
DI water	3000 ml

9.2.4.2 Place wafers into developer solution and start the timer for 2 min. Mild agitation.

9.2.4.3 Rinse the wafers with DI water. Finish rinsing in the dump-rinser, using the standard 3 dump rinse cycle.

9.2.4.4 Dry the wafers using the standard spin-rinse dry cycle.

9.2.5 Hard Bake/Descum

9.2.5.1.1 Verify the oven is set to 120°C.

9.2.5.1.2 Load wafers into a cassette and place cassette into oven with wafers in a horizontal orientation for 15 minutes.

9.2.5.1.3 Descum wafers in O_2 plasma for 30 seconds.

9.3 Deep RIE

9.3.1 Place the wafer into Deep RIE machine. Please refer to the Deep RIE User Manual for complete instructions on operating Deep RIE.

9.3.2 Update the recipe time to meets the criteria for the target etching thickness.

- Etch Time Calculation: Etch time is entered as number of loops completed. The machine runs through 5 loops a minute, so if you want to etch for 150 minutes, you will have 750 loops.

9.3.3 WTC standard Bosch recipe:

	SF6 (sccm)	C4F8 (sccm)	Time (sec.)
Etch	100	1	7
Deposition	1	100	5
Exposed area	~ 10%		
Ideal Etch rate	3.6 +/-.3 µm/min (10% exposed area)		

9.4 Pictures

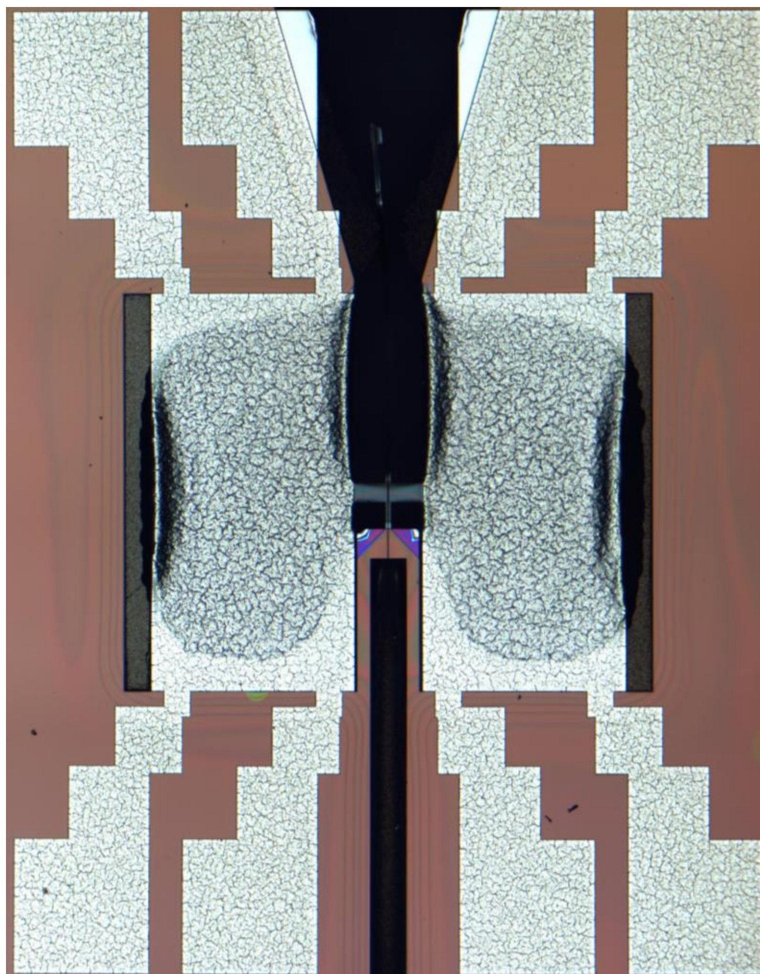

Figure 10.1 A panorama view of the device from the front side.

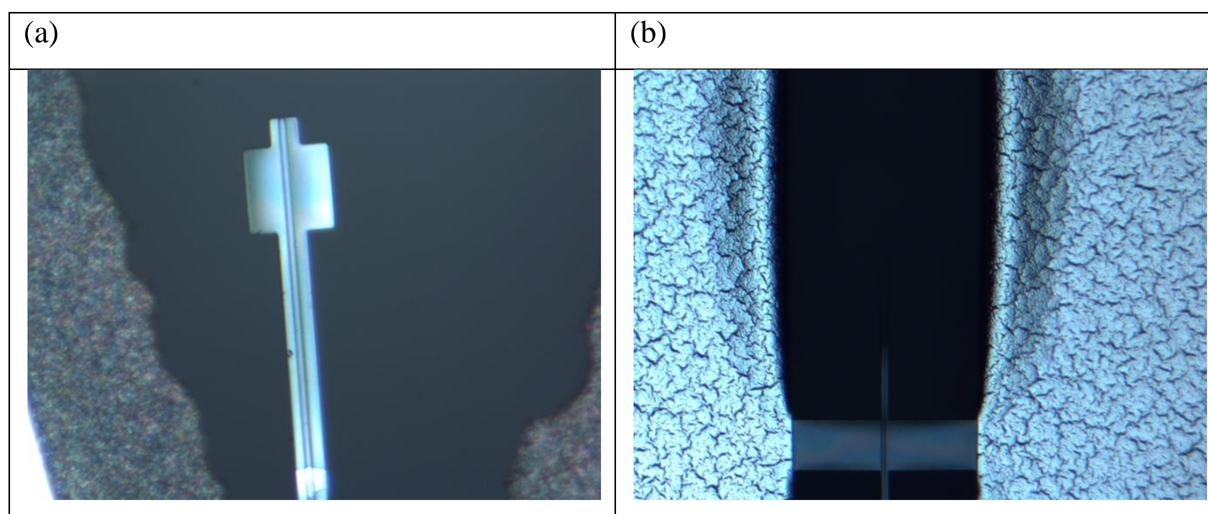

Figure 10.2 (a) large view of double-layer SU-8 waveguide after the device was released. (b) picture shows the waveguide was broken after DRIE over-etching.

APPENDIX C: PREPARING FOR THE MEMS DEVICE TEST SAMPLE

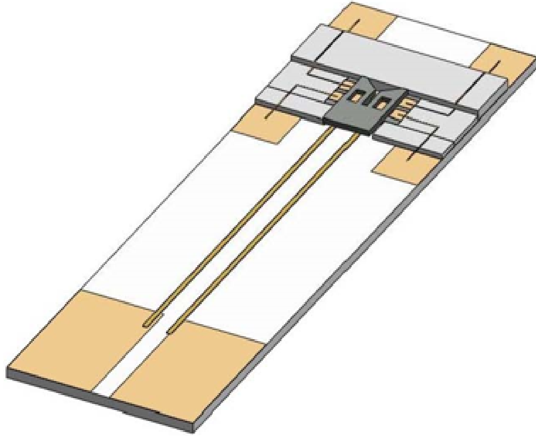

1) Glass base
2) 1 mm polymer block
3) 0.5 mm polymer block to crate a space
4) Place driving electrode layer MEMS device
5) 0.5 mm polymer block to constrain the MEMS device
6) External electrode pads
7) MEMS device with wave guide and drive membranes
8) Wire bounding on the drive device
9) Upside down the drive device
10) Place drive device
11) Wire bounding on the driving electrode layer MEMS device

(1)
Glass base

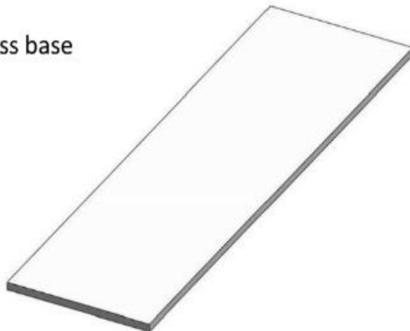

(2)
1 mm polymer block

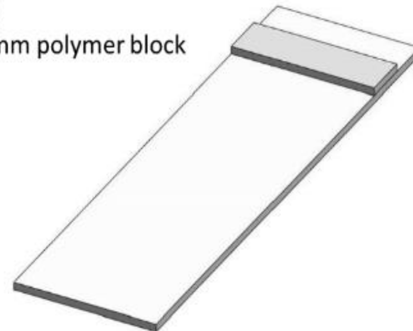

(3)
0.5 mm polymer
block to crate a space

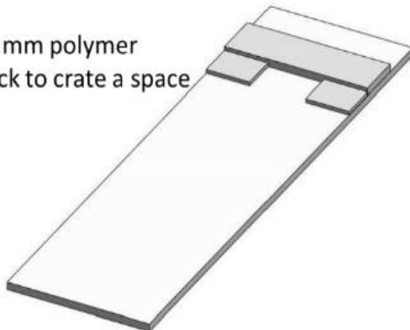

(4)
Place driving
electrode layer
MEMS device

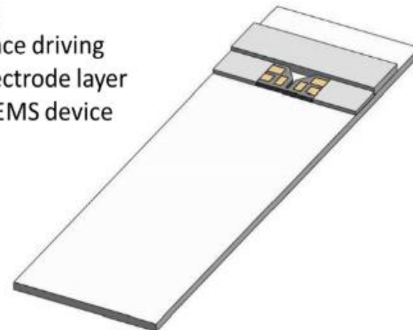

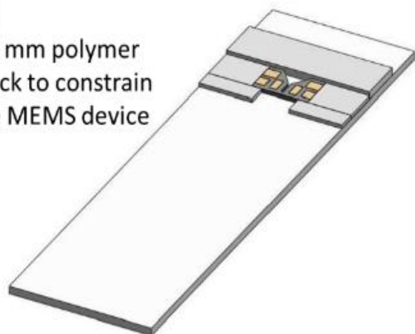
(5)
0.5 mm polymer
block to constrain
the MEMS device

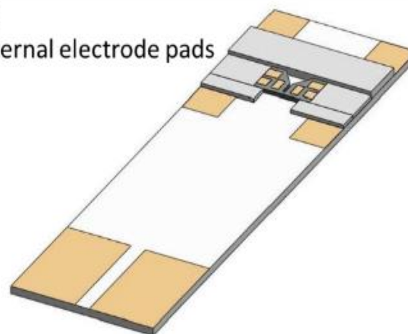
(6)
External electrode pads

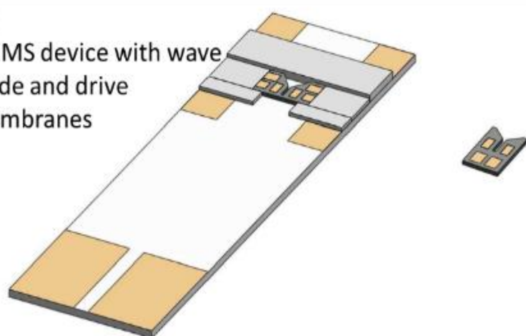
(7)
MEMS device with wave
guide and drive
membranes

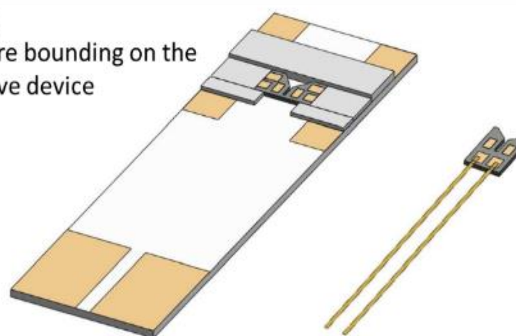
(8)
Wire bounding on the
drive device

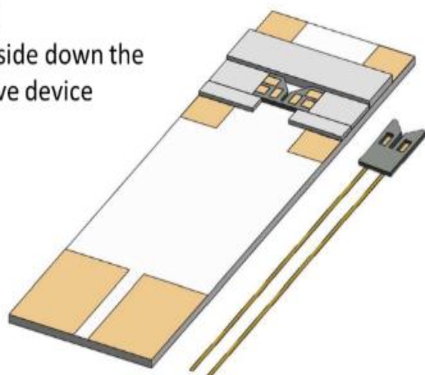
(9)
Upside down the
drive device

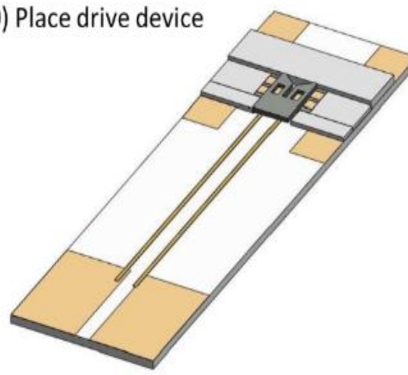
(10) Place drive device

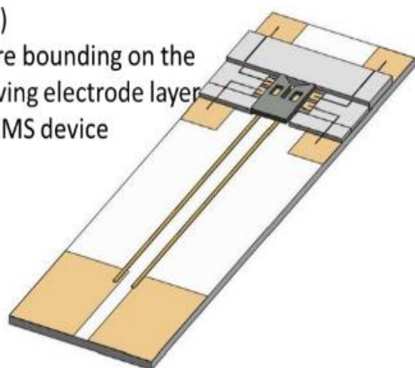
(11)
Wire bounding on the
driving electrode layer
MEMS device

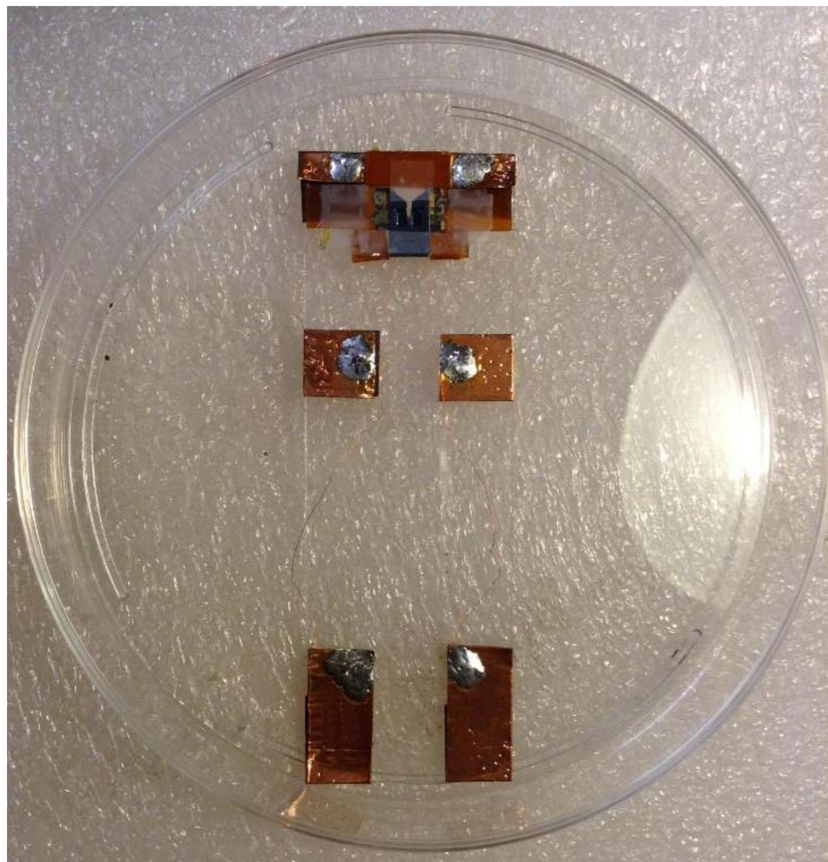

Figure 1. Top view of the MEMS device test sample.